

**The Effect of Zr-Doping and Crystallite Size
on the Mechanical Properties
of TiO₂ Rutile and Anatase**

Von der Fakultät für Biologie, Chemie und Geowissenschaften der
Universität Bayreuth

Zur Erlangung der Würde eines Doktors der Naturwissenschaften
– Dr. rer. nat. –

Genehmigte Dissertation
Vorgelegt von Dipl.-Ing.
Eva Susanne Holbig

Bayreuth, 2008

Prüfungsausschuß:

Prof. J. Brey, Universität Bayreuth	(Vorsitzender)
PD Dr. Dubrovinsky, Universität Bayreuth	(1. Gutachter)
Prof. G. Müller, Fraunhofer ISE Würzburg	(2. Gutachter)
Prof. H. Samuel, Universität Bayreuth	
Prof. F. Langenhorst, Universität Bayreuth	

Tag der Einreichung: 19.12.2007

Tag des wissenschaftlichen Kolloquiums: 29.04.2008

Content

Zusammenfassung	4
Summary	8
I. Introduction	12
1. TiO ₂ and ZrO ₂ Polymorphs	12
1.1. Polymorphs of Titania	12
1.2. Polymorphs of Zirconia	15
1.3. Energetics of Nanocrystalline ZrO ₂ and TiO ₂ Phases	16
2. TiO ₂ -ZrO ₂ Phase Diagram	19
3. Technical Applications	21
4. Tuning of Elastic Properties	23
5. Computational Work	27
6. Motivation and Outline	29
II. Methods and Instrumentation	30
1. High Pressure Experimental Techniques	30
1.1. Hydrothermal Experiments	31
1.2. Piston Cylinder Technique	32
1.3. Multi Anvil Technique	34
1.4. Diamond Anvil Cell	36
2. Analytical Methods	38
2.1. Powder X-Ray Diffraction	38
2.2. X-Ray Absorption Spectroscopy	40
2.3. Raman Spectroscopy	41
2.4. Electron Microprobe	41
2.5. Transmission Electron Microscopy	42
3. Ab-initio Calculations	43
4. Compressing Materials: Equation of State	44
III. Results and Discussion	46
1. Synthesis and Characterization of Starting Materials	46
1.1. Sol-Gel Synthesis of TiO ₂ -ZrO ₂ Powders	46
1.2. Synthesis of Microscale Anatase and Nanoscale Rutile Ti _{0.9} Zr _{0.1} O ₂	55
2. Experimental Results on the System TiO ₂ -ZrO ₂ to 10 GPa	57
3. Compression Behavior of Anatase and Rutile	60
3.1. Compression Behavior of Zr-doped Anatase	61
3.2. Compression Behavior of TiO ₂ Nanoscale Rutile	75
3.3. Compression behavior of Zr-doped microscale rutile	77
4. Pressure Induced Transformations of Anatase and Rutile	80
4.1. Multi Anvil Experiments on Phase Transition of Anatase and Rutile to TiO ₂ II	80
4.2. DAC Experiments on Phase Transitions of Zr-doped Anatase	84
4.3. DAC Experiments on Phase Transitions of Rutile	86
5. Computational Ground States of TiO ₂	90
IV. Conclusions	96
Acknowledgments	101
Bibliography	102
Erklärung	115

Zusammenfassung

TiO₂ und das System TiO₂-ZrO₂

TiO₂ ist ein wichtiges technologisches Material, das als weißes Farbpigment eingesetzt wird, sowie als Halbleiter mit großer Energielücke in farbstoffsensibilisierten Solarzellen, zur Photokatalyse und bei photochemischen Prozessen der Energieumwandlung Verwendung findet. Die bekanntesten Phasen sind Rutil (*P4₂/mnm*, Z=2), Anatas (*I4/amd*, Z=4) und Brookit (*Pcab*, Z=8), desweiteren gibt es eine Reihe von metastabilen Phasen mit geringer Dichte. Kalorimetrische Messungen an microskaligen Proben klärten die Reihenfolge von der thermodynamisch stabilsten zur instabilen Phase wie folgt auf: Rutil → Brookit → Anatas. Bei einer Verringerung der Korngröße in den nm-Bereich ändern sich die relativen Stabilitäten, so dass Rutil die stabile Phase im µm-Bereich ist, Brookit bei mittlerer Korngröße und Anatas im nm-Bereich.

Hochdruckpolymorphe von TiO₂ werden mit steigendem Druck immer dichter und die Koordinationszahl von Ti-O steigt von 6 beim Rutil-typen über 7 beim Baddeleyit-typen (ZrO₂, *P2₁/c*, Z=4) und 8 bei der kubischen Struktur, die entweder in der Fluorit- (*Fm-3m*, Z=4) oder Pyritstruktur (*Pa3*, Z=4) vorliegt, zu 9 beim Cotunnit-typen (*Pnma*, Z=4). Mehrere Hochdruckpolymorphe zeichnen sich durch ihre große Härte und interessante optische Eigenschaften aus und sind daher potentielle Kandidaten für einen technischen Einsatz.

Das Phasendiagramm des Systems TiO₂-ZrO₂ besitzt die folgenden Mischkristalle: Baddeleyit und tetragonales ZrO₂ enthalten bis zu 9 bzw. 20 mol% TiO₂. Es gibt verschiedene (Zr,Ti)₂O₄ Phasen mit einem Gehalt an TiO₂ von zwischen 42 und 67 mol%. Rutil baut mit stiegender Temperatur bis zu ~15 mol% ZrO₂ bei 1600°C ein. Experimente bei hohen Drücken und Temperaturen wurden unter Verwendung der Stempel-Zylinder-Presse und der Viel-Stempel-Presse durchgeführt. Abgeschreckte Proben von Rutil, Anatas und deren Hochdruckmodifikationen, die bei Drücken bis zu 10 GPa synthetisiert wurden, zeigen einen Gehalt von ≤10 mol% ZrO₂, Zr-gedopte TiO₂ Ausgangsmaterialien haben daher die chemische Zusammensetzung Ti_{0,9}Zr_{0,1}O₂.

Experimentelle Methoden dieser Studie

Das Kompressionsverhalten von Anatas und Rutil mit der Zusammensetzung von TiO_2 und $\text{Ti}_{0.9}\text{Zr}_{0.1}\text{O}_2$ wurde anhand von Proben mit Kristallitgrößen im μm - und nm -Bereich untersucht. Kompressionsexperimente wurden in der Diamant-Stempelzelle durchgeführt und die Proben wurden mit Hilfe von *in-situ* Röntgendiffraktometrie, Röntgenabsorption und Ramanspektroskopie charakterisiert. Eine Sol-gel Methode wurde zur Herstellung von Ausgangsmaterialien $\text{Ti}_x\text{Zr}_{1-x}\text{O}_2$ mit $x = 0.00, 0.10, 0.25, 0.33, 0.50, 0.67, 0.75, 0.90$ und 1.0 entwickelt. Bei den Syntheseprodukten mit $x=0.90$ und 1.0 handelte es sich um nanoskaligen Anatas, der bei 1000°C zu mikroskaligem Rutil gesintert werden konnte. In Hydrothermal-Experimenten wurde außerdem nano-Anatas $\text{Ti}_{0.9}\text{Zr}_{0.1}\text{O}_2$ verwendet um mikroskaligen Zr-gedopten Rutil zu synthetisieren.

Kompressionsverhalten von Anatas

Experimente zeigen, dass Anatas weniger kompressibel wird, wenn die Kristallitgröße in den nm -Bereich herabgesetzt oder das Material mit Zr gedopt wird. Gefittete Zustandsgleichungen (EoS) der zweiten Ordnung ($K_0'=4$) weisen einen Kompressionsmodul von micro-Anatas von $K_0=178(1)$ GPa [1] bzw. $K_0=179(2)$ GPa [2] auf. Das nanokristalline Äquivalent hat einen höheren Wert von zwischen $K_0=237(3)$ GPa [3] bis $K_0=243(3)$ GPa [4]. In dieser Studie wurde das Kompressionsmodul von micro-Anatas $\text{Ti}_{0.90}\text{Zr}_{0.10}\text{O}_2$ zu $K_0=195(38)$ GPa ermittelt, vergleichbar zu ungedoptem Material. Der höchste Wert wurde für nano-Anatas $\text{Ti}_{0.90}\text{Zr}_{0.10}\text{O}_2$ gefunden, hier ist $K_0=258(8)$ GPa. Der Einbau von Zr reduziert daher die Kompressibilität, obwohl ZrO_2 Polymorphe generell kompressibler sind als die dazugehörigen TiO_2 Phasen.

Für Zr-gedopten Anatas zeigten Röntgendiffraktionsanalysen eine signifikante Änderung des Kompressionsverhaltens bei einem Druck >4 GPa, hervorgerufen durch die Wirkung von deviatorischem Streß der während der Kompression im nano-Material entsteht. Berechnungen an Superzellen mit verschiedenen Abständen von benachbarten Zr-Atomen legten die Vermutung nahe, dass es zur Cluster-Bildung von Zr-Atomen im

(Ti,Zr)O₂ Anatas kommt. Die resultierende Gitterstörung kann das veränderte Kompressionsverhalten weiterhin beeinflussen.

Zr-gedoppter nano-Anatas wird während wiederholter Zyklen von Kompression und Druckentlastung steifer. Während das Kompressionsmodul der ersten Kompression bei 211 GPa lag, zeigte die Probe nach Druckentlastung bei wiederholter Komprimierung ein Kompressionsmodul von 249 GPa. Es liegt die Vermutung nahe, dass partielle druckinduzierte Amorphisierung eine entscheidende Rolle für die Versteifung des Materials spielt.

Microanatas TiO₂ transformiert bei der Komprimierung zur MI Phase. Der Transformationsdruck von Anatase zu MI steigt, wenn die Kristallitgröße in den nm-Bereich fällt, und zwar von 12 GPa bei microskaligem Material zu 18 GPa bei Anatas mit einer Kristallitgröße von 12 nm. Noch kleinere Kristallite wandeln sich in eine amorphe Phase bei Drücken von 20–24 GPa. Der Einbau von Zr wirkt sich nicht auf den Transformationsdruck aus.

Kompressionsverhalten von Rutil

Experimentelle Ergebnisse zeigen, dass weder der Einbau von Zr, noch die Reduzierung der Kristallitgröße in den nm-Bereich einen Einfluss auf das Kompressionsverhalten von Rutil haben. Die Kompressionsmodule von nano- und microskaligem TiO₂ sowie nanoskaligem Ti_{0.90}Zr_{0.10}O₂ wurden mit 230(20), 251(12) und 203(13) GPa bestimmt, Unterschiede dieser Werte sind geringer als die Toleranzen der Messungen. Diese Ergebnisse unterscheiden sich von denen von Anatas, für den die Reduzierung der Kristallitgröße und der Einbau von Zr zu einer Erhöhung des Kompressionsmoduls führten.

Experimente zeigen, dass der Transformationsdruck von Rutil TiO₂ zur MI Phase mit einer Erniedrigung der Kristallitgröße steigt. In Experimenten, in denen kein Druckmedium benutzt wurde, liegt der Transformationsdruck bei 12 GPa für microskaligen Rutil, bei 18 GPa für Rutil mit einer Kristallitgröße von 15 nm und bei 22 GPa für eine Probe mit 10 nm. Der Einbau von Zr hat keinen Einfluss auf den Transformationsdruck.

Berechnungen des Grundzustandes von TiO₂

Ab-initio Berechnungen der elektronischen Struktur mit Hilfe der Dichtefunktionaltheorie wurden durchgeführt, um die Energien der Grundzustände der TiO₂ Phasen Rutil, Anatas, Brookit, TiO₂II und der MI-Phase zu berechnen. Dazu wurden die projector augmented wave und die linear augmented plane wave Methoden angewandt, zusammen mit der lokalen Dichte Näherung (LDA) und zwei Typen der generalisierten Gradienten Näherung (GGA) zum Austausch-Korrelationspotential der Elektronen. Es wurden die Formulierungen von Perdew, Bunge und Enzerhoff (PBE), sowie durch Wu und Cohen (WC) verwendet.

Die Null-Druck Volumina wurden in LDA Berechnungen um 3% kleiner, und in PBE und WC Berechnungen um 8 und 0.4% größer als experimentelle Werte bestimmt. Die stabile Phase bei 0 GPa ist Baddeleyite in den LDA Berechnungen und Anatas in GGA Berechnungen. Dies steht im Gegensatz zu experimentellen Ergebnissen, die Rutil als die stabile Modifikation zeigen. Rutil besitzt jedoch die höchste Energie in LDA Berechnungen und mittlere Energie in GGA Berechnungen.

Summary

TiO₂ and the System TiO₂-ZrO₂

TiO₂ is an important technological material, used as white pigment, as wide band gap semiconductor in electrochemical dye solar cells, for photocatalysis and in photochemical energy-conversion processes. The most abundant phases are rutile (*P4₂/mnm*, *Z=2*), anatase (*I4/amd*, *Z=4*) and brookite (*Pcab*, *Z=8*). In addition, there are a number of metastable low density modifications. Calorimetric measurements showed that the sequence for microscale material from the stable to the less stable phase is: rutile → brookite → anatase. Several phase stability crossovers occur with the decrease of the crystallite size while rutile is the stable phase for big crystallite sizes, brookite is stable for intermediate sizes and anatase for smallest crystals.

High pressure polymorphs of TiO₂ are subsequently denser and have increasing coordination number of Ti-O with increasing pressure, ranging from 6 for the rutile type over 7 for the baddeleyite type (ZrO₂, *P2₁/c*, *Z=4*) and 8 for the cubic structure, which is fluorite type (*Fm-3m*, *Z=4*) or pyrite type (FeS₂, *Pa3*, *Z=4*), up to 9 for the cotunnite type (PbCl₂, *Pnma*, *Z=4*). Several high pressure polymorphs are suggested as candidate materials for technological applications because they are very hard and have interesting optical properties.

The phase diagram of the system TiO₂-ZrO₂ shows the following solid solutions. Baddeleyite and tetragonal ZrO₂ contain up to ~9 and 20 mol% TiO₂, respectively, several distinct phases (Zr,Ti)₂O₄ with the compositional range of 42 to 67 mol% exist and TiO₂ rutile can be doped with up to ~15 mol% ZrO₂ at 1600°C. Experiments at high pressure and temperatures performed here, using piston cylinder and multi anvil presses showed that quenched samples of rutile, anatase and high pressure polymorphs synthesized at up to 10 GPa adopt ≤10 mol% ZrO₂, Zr-doped TiO₂ starting materials therefore have the composition Ti_{0.9}Zr_{0.1}O₂.

Experimental Methods of this Study

The compression behavior of anatase and rutile was studied for TiO_2 and $\text{Ti}_{0.9}\text{Zr}_{0.1}\text{O}_2$ starting materials with crystallite size in the micro- and also nanometer range. Compression experiments were carried out in the diamond anvil cell and samples were characterized by *in-situ* X-ray diffraction, X-ray absorption and Raman spectroscopic measurements. A sol-gel route was developed for the synthesis of starting materials $\text{Ti}_x\text{Zr}_{1-x}\text{O}_2$ with $x=0.00, 0.10, 0.25, 0.33, 0.50, 0.67, 0.75, 0.90$ and 1.0 . Product of the synthesis with $x=0.90$ and 1.0 was nanoscale anatase, which was annealed at 1000°C to microscale rutile. In hydrothermal experiments, nanoscale anatase $\text{Ti}_{0.9}\text{Zr}_{0.1}\text{O}_2$ was used as starting material for the synthesis of microscale Zr-doped anatase.

Compression Behavior of Anatase

Experiments show that anatase becomes less compressible when the crystallite size is decreased to the nanometer scale and when the material is Zr-doped. Second order EoS fits ($K_0'=4$) resulted in a bulk modulus of microscale anatase of $K_0=178(1)$ GPa [1] and $K_0=179(2)$ GPa [2]. The nanoscale counterpart shows much higher values of $K_0=237(3)$ GPa [3] and $K_0=243(3)$ GPa [4]. In this study, it was found that microscale anatase $\text{Ti}_{0.90}\text{Zr}_{0.10}\text{O}_2$ has $K_0=195(38)$ GPa, which is comparable to undoped material. Largest values were found for nanoscale anatase $\text{Ti}_{0.90}\text{Zr}_{0.10}\text{O}_2$ with $K_0=258(8)$ GPa. Zr-doping thus reduces the compressibility of nanoanatase, even though ZrO_2 polymorphs are more compressible than the corresponding TiO_2 forms.

For the Zr-doped nanoanatase, XRD analysis showed a significant change in compression behavior at pressures >4 GPa, suggested as a consequence of deviatoric stresses during experimental compression of the nanoscale material. Computations on supercells with different distances of neighboring Zr-atoms suggested cluster formation of Zr in the $(\text{Ti,Zr})\text{O}_2$ anatase. The resulting structural distortions can further augment the change in compression behavior.

Zr-doped nanoanatase becomes stiffer upon multiple compression cycles. While the bulk modulus of the first compression was 211 GPa, after the sample was decompressed, the second compression showed a bulk modulus of 249 GPa. We suggest that partial pressure induced amorphization plays an important role for the observed stiffening.

Microscale anatase TiO_2 transforms to the MI phase upon compression. The transition pressure increases with a decreasing crystallite size from 12 GPa for microscale material to 18 GPa for anatase with crystallite size of 12 nm. Smaller particles transform to an amorphous phase at pressures of 20–24 GPa. Zr-doping does not seem to vary the transformation pressure.

Compression Behavior of Rutile

Experimental results show that neither the incorporation of Zr nor the decrease of crystallite size to the nanometer range modifies the bulk modulus of rutile. Values for micro- and nanoscale TiO_2 as well as nanoscale $\text{Ti}_{0.90}\text{Zr}_{0.10}\text{O}_2$ were 230(20), 251(12) and 203(13) GPa, the differences of the values lie within the error of the fits. These results are different from those of anatase, where a decrease of crystallite size and doping with Zr leads to an increase of the bulk modulus.

Experiments show that the pressure of transformation of rutile TiO_2 to the MI phase increases with decreasing crystallite size. In experiments with no use of a pressure medium, the transformation pressure is 12 GPa for microscale rutile, 18 GPa for rutile with crystallite size of 15 nm and >22 GPa for 10 nm. Zr-doping has no effect on the transformation pressure. However, the transformation pressure is lowered when siliconoil is used as pressure medium.

Computational Ground States of TiO_2

Ab-initio all-electron density functional electronic structure simulations on the ground state energetics of the TiO_2 phases rutile, anatase, brookite, TiO_2II and MI-phase were performed using the projector augmented wave and the linear augmented plane wave methods along with local density approximation (LDA) and two types of

generalized gradient approximations (GGA), using the formulations by Perdew, Bunge and Enzerhoff, referred to as PBE, and by Wu and Cohen, referred to as WC.

The zero pressure volumes are predicted smaller by <3% in LDA computations and larger by 8 and 0.4% in PBE and WC computations. The stable structure at 0 GPa is baddeleyite for LDA computations and anatase for GGA computations, contradicting experimental results that determine rutile as the most stable phase. Rutile appears to have the highest energy in LDA computations and intermediate energy in GGA computations.

I. Introduction

1. TiO_2 and ZrO_2 Polymorphs

Titania, TiO_2 and zirconia, ZrO_2 , exhibit a series of high pressure polymorphs with common crystallographic features, shown also for other simple oxides with the formula AO_2 . With increasing pressure the sequent polymorphs are denser and have an increasing coordination number (CN), which is the number of oxygen ligands around the cation. The coordination numbers range from 6 for the rutile type (TiO_2 , $P4_2/mnm$, $Z=2$) over 7 for the baddeleyite type (ZrO_2 , $P2_1/c$, $Z=4$, here referred to as MI) and 8 for the fluorite type ($Fm-3m$, $Z=4$) or pyrite type, respectively (FeS_2 , $Pa3$, $Z=4$) up to 9 for the cotunnite type (PbCl_2 , $Pnma$, $Z=4$). Furthermore, a 10-fold coordination of the post-cotunnite structure was found for PbCl_2 and SnCl_2 and was proposed also for AO_2 oxides with heavy cation at very high pressure [5,6]. Among the oxides that undergo the pressure transition sequence fully or partly from CN=6 to 9 are: TiO_2 [2,7-24], ZrO_2 [25-36], HfO_2 [5,28,33,37-44], PbO_2 [5] and SiO_2 [45-49]. Because SiO_2 is an important phase of the Earth's crust and mantle, its transition sequence is of great interest for geosciences. TiO_2 served as an analogous system in the search for potential post-stishovite silica phases. It was chosen because the phase transitions occur at lower pressures compared to the SiO_2 system [22,50].

1.1. Polymorphs of Titania

At ambient conditions, the stable form of TiO_2 is rutile, but also anatase ($I4/amd$, CN=6) and brookite ($Pcab$, CN=6) exist as metastable forms, as well as modifications with the structure of $\beta\text{-VO}_2$ ($C2/m$ [51]), hollandite ($I4Im$) [52] and ramsdellite ($Pbnm$) [53]. Rutile, anatase, brookite, TiO_2II ($Pbcn$, CN=6, $\alpha\text{-PbO}_2$ structure) and the $\beta\text{-VO}_2$ – structured phase occur naturally as accessory minerals in sediments, metamorphic, plutonic and volcanic rocks, derived from crust and mantle [54]. Anatase, brookite and the $\beta\text{-VO}_2$ – structured phase convert to rutile during prograde metamorphism. Upon decompression, TiO_2II is a common quench-product of high pressure polymorphs.

Because rutile is resistant to weathering, it is inherited by metasediments, making them the predominant host for Ti along with other trace elements [54].

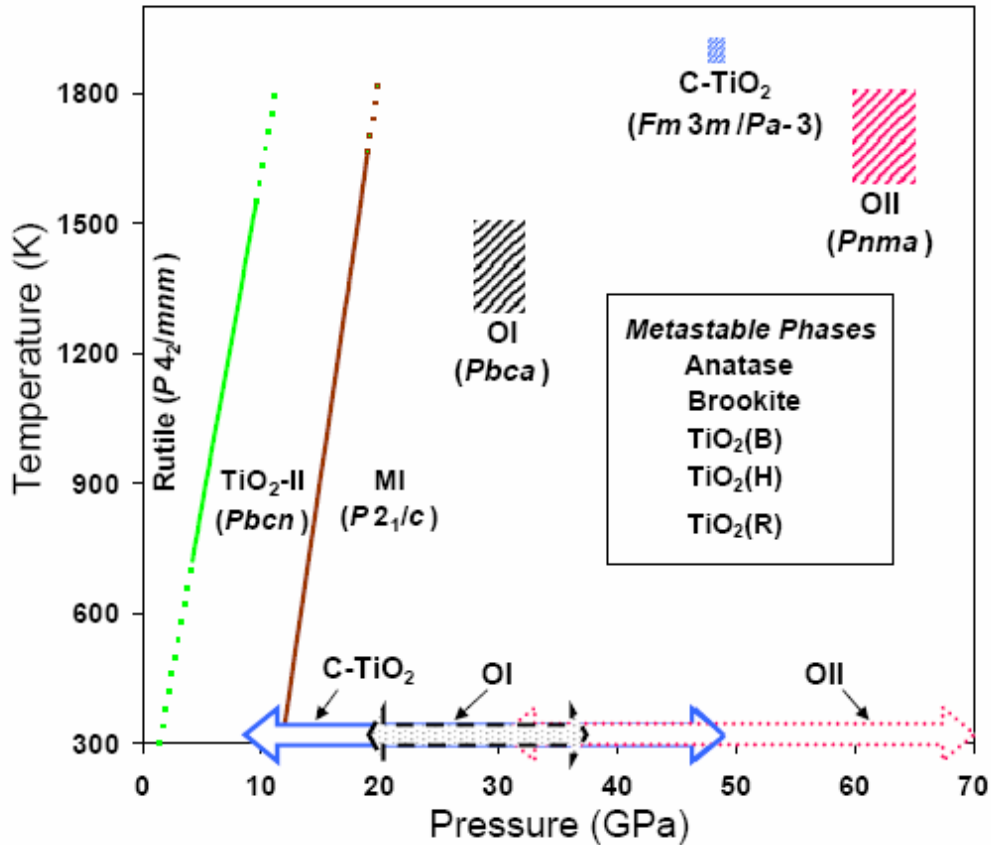


Figure 1. Phase diagram of TiO_2 from diamond anvil cell experiments. Shown are the pressure and temperature conditions of stable phases, the known metastable phases are named in the inset. The rutile– TiO_2II and TiO_2II –MI phase boundaries are after refs. [22,24,55,56]. The P-T conditions of synthesis for OI [9], C- TiO_2 [18], and OII [11] are shown by the shaded areas. The arrows indicate the pressure ranges over which P-V data were retrieved for OI (19-36 GPa), OII (30-80 GPa), and C- TiO_2 (9-48 GPa) during compression (right pointing arrow) and decompression (left pointing arrow). After *Swamy et al.* [57].

The sequence of TiO_2 high pressure polymorphs was determined experimentally as follows (Figure 1): TiO_2II (orthorhombic) was found upon compression of anatase at pressures of 2.6-7 GPa [2,16,17,58]. The phase is quenchable to ambient conditions. Anatase, rutile and TiO_2II transform to MI at ~ 12 GPa [1,2,11,14,17,55]. The transformation of MI to OI was found at 30 GPa by laser heating to 1300-1500 K and at 48 GPa OI transforms to a mixture of OII and the cubic phase [18]. A transformation from MI to OII was found at 60 GPa under laser heating to 1260-1800 K. OII could be compressed to at least 80 GPa and transforms to MI at 25 GPa upon decompression. A rapid quench at 77 K, using liquid nitrogen, preserved OII to room pressure and low

temperatures [11]. Upon decompression at ambient temperatures, the transformation of OII to MI was found at 20 GPa, the cubic phase could be followed to below 9 GPa and below 7 GPa MI transforms to a mixture of TiO₂II and rutile [18]. The pressures of phase transformations are different for compression and decompression and vary in different studies. The reason for that is most likely that in many cases phase transformations to the thermodynamically stable phase were hindered kinetically and only the metastable phases were observed. The apparent pressure-temperature phase diagram of TiO₂ is presented in Figure 1, containing transformation pressures as well as pressure ranges in which the phases were observed.

In the following chapters, the phases anatase, rutile, TiO₂II and MI will play an important role and their structures are described in more detail in the following (Figure 2). In anatase, each Ti is surrounded by an octahedron of six oxygen atoms. Four edges per octahedron are shared, building a “zig-zag” chain parallel to *a* as well as *b*. The chains are stacked antiparallel to the *c* axis. Rutile consists of TiO₆ octahedra and two opposing edges of each octahedron are shared, forming linear chains parallel to the *c*-direction. In the *a*-*b*-plane, the chains are linked via corner-sharing oxygen atoms. In TiO₂II, the octahedra make up a network similar to rutile but are distorted. The structure of MI can be seen as an even further distorted version of TiO₂II, exhibiting a seven-fold coordination of the Ti-atom.

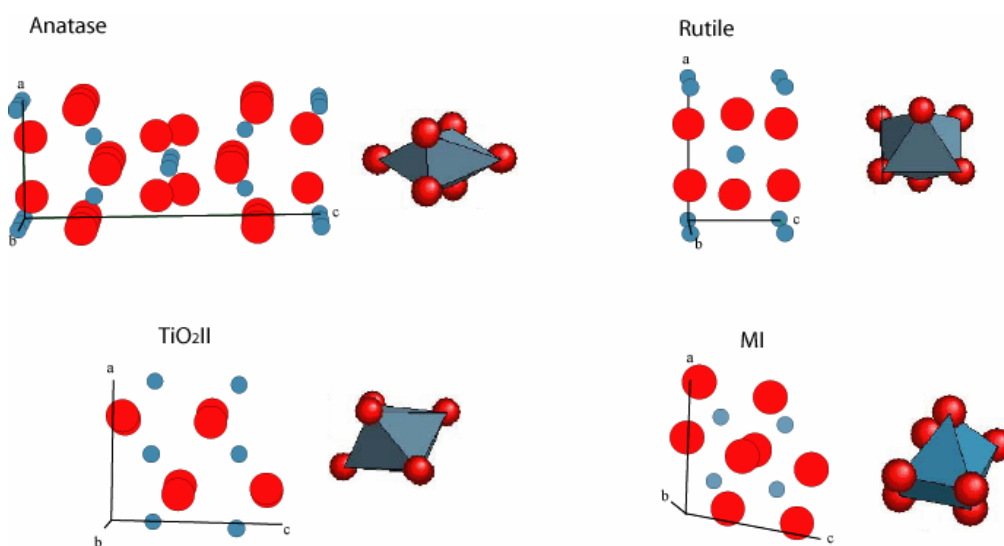


Figure 2: Elementary cells and polyhedra of TiO₂ anatase, rutile, TiO₂II and MI. Oxygen atoms are shown in red, titanium atoms and polyhedra are shown in blue.

1.2. Polymorphs of Zirconia

The ZrO_2 polymorph stable at ambient pressures is monoclinic baddeleyite. It is a widespread trace mineral, occurring in a variety of rock types like meteorites, tektites, mafic and ultramafic rocks, alkaline intrusions, kimberlites and metacarbonates [59]. At ambient pressure, it transforms to a tetragonal phase above $1200^\circ C$ with space group $P4_2/nmc$ and $CN=7$, which is a distorted version of the cubic fluorite-structured phase, occurring above $2372^\circ C$. ZrO_2 melts at $2680^\circ C$ [60,61] and under pressure baddeleyite is stable up to 10 GPa, polymorphs at higher pressures are OI (10-25 GPa) and OII (25-42 GPa). At higher pressures, another orthorhombic phase OIII was found but the structure could not be determined [44]. The values given by *Ohtaka et al.* [34] for the stabilities of the high pressure polymorphs differ strongly from the ones above: Baddeleyite <3-4GPa, OI <12.5 GPa and OII <24 GPa. Both groups of authors suggest cotunnite structure for OII and describe an orthorhombic phase, OIV, which is stable at higher temperatures than OII and higher pressures than the tetragonal phase with space group most likely $Pbc2_1$. The pressure-temperature phase diagram of ZrO_2 is presented in Figure 3.

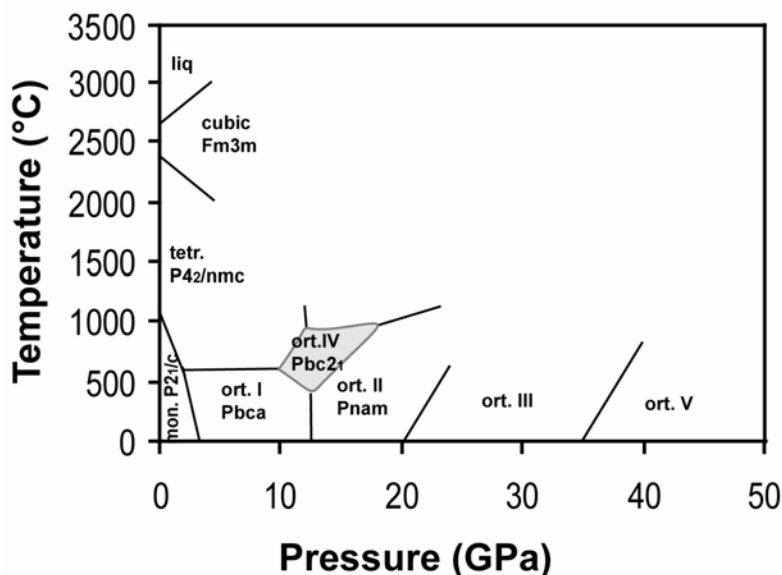


Figure 3: Generalized phase diagram of ZrO_2 from *in-situ* detection of phase transitions and characterization of quenched samples. The stable form at ambient conditions is monoclinic baddeleyite, polymorphs at high temperature are tetragonal and cubic phases. High pressure polymorphs are orthorhombic (named ort. I to V), space groups of phases ort. III and V are not identified and the existence of ort. IV is under debate. Redrawn after experimental data from refs. [34,44].

1.3. Energetics of Nanocrystalline ZrO_2 and TiO_2 Phases

In microscale particles, only a negligible amount of atoms is situated on the surface, whereas the bulk mass of atoms is surrounded by other bulk atoms. With a decrease of the crystallite size to the nanometer range, the relative amount of atoms on the surface increases. Atoms on the surface exhibit a surface structure, different from the bulk material due to unsaturated bondings of the atoms. Energetics are therefore very different compared to the bulk mass and in most cases, H_2O is adsorbed on the surface, making the energetics even more complicated. Figure 4 shows a nanometer scale particle with a core of bulk material and a surface area as the part of the particle within hailing distance of the surface, defined to be 0.5 nm. With decreasing particle size, the fraction of atoms near the surface increases, and at a certain point, all of the atoms belong to the surface shell. As will be seen later, the mechanical properties and phase stabilities are strongly affected by a decrease of the crystallite size to the nanometer range.

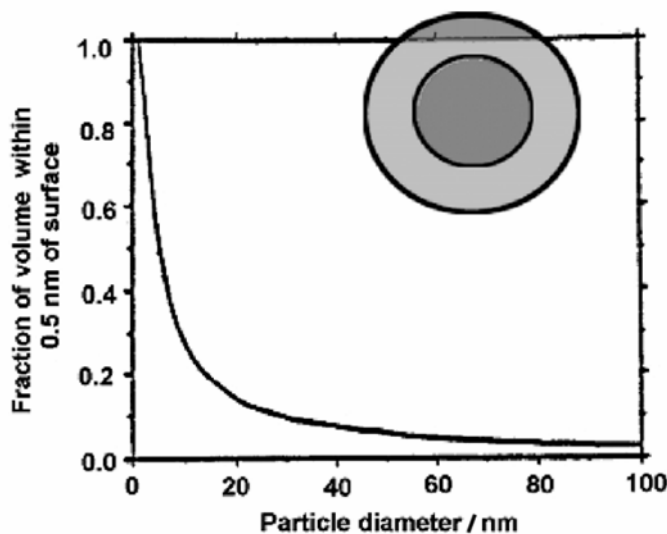


Figure 4: Plot of fraction of volume for nanoscale particle as a function of the particle diameter, showing the fraction of volume within 0.5 nm of the surface for a spherical particle. From ref. [62].

1.3.1 Energetics of Nanocrystalline Titania

Relative phase stabilities of micro- and nanoscale rutile, brookite and anatase were intensively studied by *Ranade et al.* [63], using high temperature oxide melt drop solution calorimetry. In that method, two samples are each dropped into a molten oxide, such as lead borate, sodium molybdate or alkali borate. The difference in observed

enthalpy of reactants and products gives the heat of formation. The stable form of TiO_2 microscale materials is rutile, having the lowest enthalpy. Relative to bulk rutile, bulk brookite is 0.71 ± 0.38 kJ/mol [64] and bulk anatase is 2.61 ± 0.41 kJ/mol higher in enthalpy [63]. Experiments on nanoscale materials revealed that rutile has the highest surface enthalpy of 2.2 ± 0.2 J/m², brookite has a medium value of 1.0 ± 0.2 J/m² and anatase has the lowest value of 0.4 ± 0.1 J/m². The closely balanced energetics lead to several phase stability crossovers occurring with the decrease of the crystallite size (compare Figure 5). The stable phase (with lowest enthalpy) is rutile for big crystallite sizes, brookite for intermediate sizes and anatase for smallest crystallite sizes.

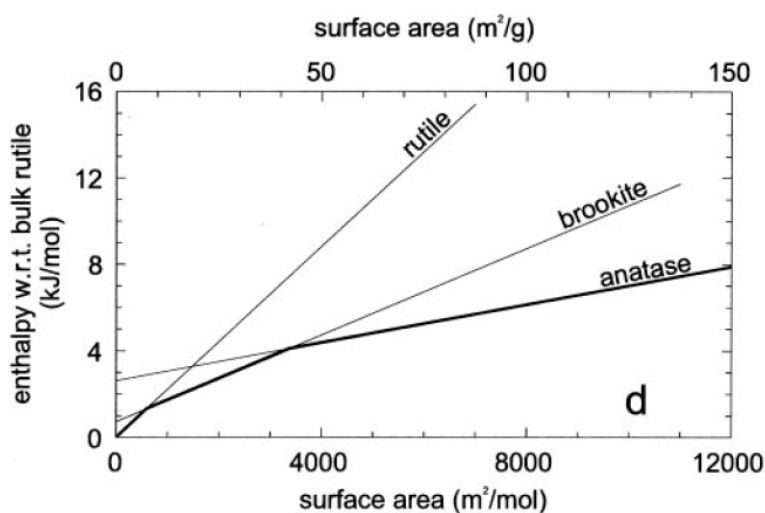


Figure 5: Enthalpy of micro- and nanoscale TiO_2 phases rutile, brookite and anatase with respect to microscale rutile versus surface area. Data were obtained by high temperature oxide melt drop solution calorimetry using $3\text{Na}_2\text{O} \cdot 4\text{MoO}_3$ as a solvent. The darker line segments indicate the energetically stable phases. From ref. [63].

Because the MI phase is not quenchable, calorimetric measurements can not be performed on the material. The following calorimetric data on TiO_2II are reported. For anatase-rutile a difference in enthalpy of 1.24 kcal/mole was measured [65] and for TiO_2II -rutile a value of 0.76 kcal/mole [66]. We can therefore estimate that the sequence for bulk material from the stable to the less stable phase is: rutile \rightarrow brookite \rightarrow TiO_2II \rightarrow anatase. Taking into account that TiO_2II is a common decomposition product in experiments and occurs naturally as nanocrystallites (e.g. [67]), we can furthermore estimate very roughly that it would plot with a slope comparable to anatase in Figure 5.

1.3.2. Energetics of Nanocrystalline Zirconia

Calorimetric measurements on ZrO_2 baddeleyite as well as the tetragonal and amorphous phases [68] show that for bulk material, the stable modification is baddeleyite. The enthalpy of the monoclinic to tetragonal transition was estimated to be 10 ± 1 kJ/mol and the amorphization enthalpy to be 34 ± 2 kJ/mole higher than for bulk baddeleyite. The monoclinic form has the highest surface enthalpy of 4.2 J/m², the tetragonal phase has intermediate value of 0.9 J/m² and the amorphous phase 0.5 J/m² [68]. Energy crossovers for nanocrystalline zirconia enthalpies are shown in Figure 6. The stable phase (with lowest enthalpy) is monoclinic zirconia for big crystallite sizes, the tetragonal phase for intermediate sizes and the amorphous phase for smallest crystallite sizes.

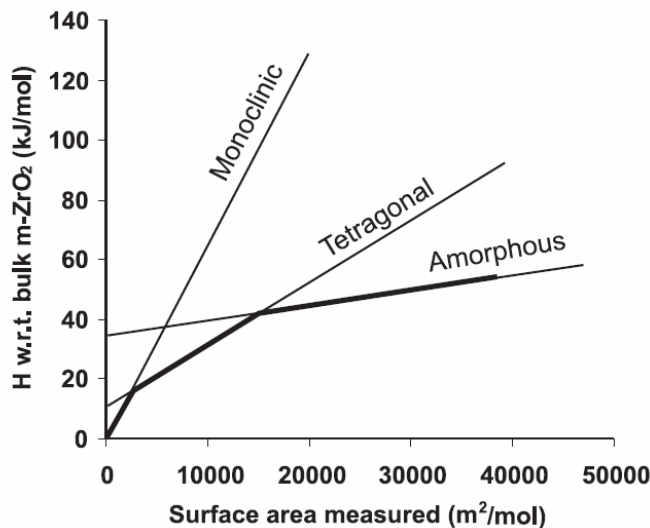


Figure 6: Enthalpy of micro- and nanoscale ZrO_2 phases with respect to the microscale monoclinic baddeleyite, showing several phase stability crossovers of nanocrystalline zirconia. Data were obtained by high temperature oxide melt drop solution calorimetry using lead borate as solvent. The darker line segments indicate the energetically stable phases. From ref. [68].

2. $\text{TiO}_2\text{-ZrO}_2$ Phase Diagram

The phase diagram of TiO_2 and ZrO_2 is well studied up to a pressure of 2.8 GPa [69-71] and a temperature of 1600°C [72-76], results are presented in Figure 7. The authors describe the occurrence of monoclinic ZrO_2 (baddeleyite), containing up to ~ 9 mol% TiO_2 . The tetragonal ZrO_2 phase, stable at temperatures greater than $\sim 1060^\circ\text{C}$ can adopt much higher amounts of TiO_2 , up to 20 mol%. The authors distinguish between an ordered phase of $(\text{Zr,Ti})_2\text{O}_4$ at a temperature below 1160°C and a disordered one at higher temperatures. The ordered phase contains 64.9 mol% TiO_2 at 800°C to 60.4 mol% TiO_2 at 1060°C . A jump occurs to ~ 49 mol% TiO_2 at 1080°C , coinciding with a remarkable change in the b -dimension, yielding at a second, distinct ordered phase. The disordered phase, stable at temperatures $>1160^\circ\text{C}$ contains 50 mol% TiO_2 at 1160°C and a bigger range of compositions at higher temperatures with 42 to 67 mol% TiO_2 at 1600°C . The mineral srilankite (ZrTi_2O_6 [77]) represents a specific composition of this solid solution. The TiO_2 phase is rutile and its Zr-incorporation increases linearly with temperature up to ~ 15 mol% ZrO_2 at 1600°C .

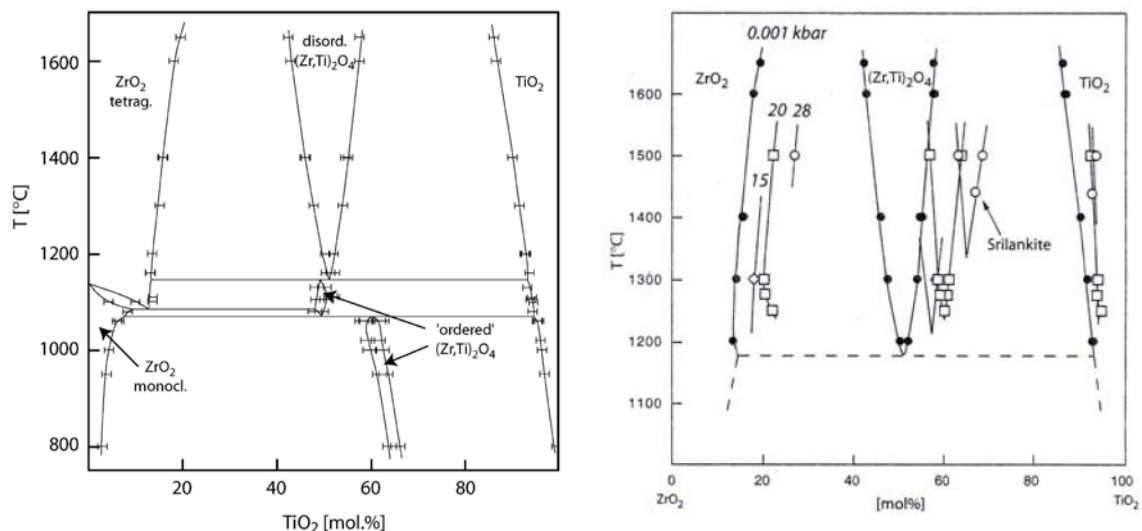


Figure 7: $\text{ZrO}_2\text{-TiO}_2$ phase diagram from characterization of quenched samples (refs. [75,76]). All phases (tetragonal and monoclinic ZrO_2 , ordered and disordered $(\text{Zr,Ti})_2\text{O}_4$, TiO_2) are solid solutions, and the phase fields are labelled with the predominant end-member. The label 'ordered' encompasses partly and fully ordered $(\text{Zr,Ti})_2\text{O}_4$.

Srilankite is a rare mineral, its origin and stability are discussed controversially and for a long time, a hydrothermal origin was proposed for natural samples, first found in a gemstone mine [77], a lamprophyre pipe [78] and ultramafic diatremes [79]. However, experimental results show an ordered phase at low temperatures and disordering (as for srilankite) only at temperatures $>1160^{\circ}\text{C}$, thus suggesting magmatic origin. Newer findings of srilankite in crustal mafic granulites [80] and a gabbroic vein [81] are consistent with the generation at high temperatures.

There are three different phases with the space group $Pbcn$: the ordered solid solution $(\text{Zr,Ti})_2\text{O}_4$, having the structure of columbite; the disordered solid solution $(\text{Zr,Ti})_2\text{O}_4$ with the structure of scrutinyite [82], containing srilankite with the formula ZrTi_2O_6 [77]; Furthermore there is the TiO_2 high pressure polymorph TiO_2II . There is ongoing research whether this phase makes a solid solution with one of the phases mentioned. In chapter III. section 2. "Experimental results on the system $\text{TiO}_2\text{-ZrO}_2$ to 10 GPa", new results are presented, suggesting that it is a separate phase.

3. Technical Applications

TiO₂ phases have a high refractive index with values of 2.52, 2.63 and 2.72 for anatase, brookite and rutile [83]. Because it lacks absorption of visible light, it is used as white pigment for paints, plastics and paper. As a wide band gap semiconductor ($E_g=3.0-3.2$ eV) it is used for electrochemical dye solar cells [84] and exhibits a good performance in photocatalysis [85,86]. It is chemically inert and highly corrosion resistant, ideal for exposition to aqueous solutions [87] and is used in the development of photoelectrodes for photochemical energy-conversion processes [88].

ZrO₂ is a common functional ceramic material as it is hard, chemically inert, has a high melting point, good ionic conductivity and interesting electrical properties. It is used as structural ceramic, high temperature solid electrode and optical material. It finds electrical applications, including catalyst supports, oxygen sensors, and thermal barrier coatings. The tetragonal and cubic phases of ZrO₂ are stabilized by doping an amount of ~0.15 mol% of other oxides like CaO, MgO, and Y₂O₃ [26,89]. Partially stabilized ZrO₂ and Y₂O₃-stabilized tetragonal ZrO₂ polycrystalline (Y-TZP) materials are particularly useful for advanced structural applications because of their high strength and fracture toughness. Furthermore, natural baddeleyite and synthetic ZrO₂ ceramics are candidate materials for the safe disposal of high level nuclear waste from power reactors as well as pure plutonium from disposition of nuclear weapons [59,90].

Zirconium titanate ceramics are used as temperature-stable dielectric materials for ceramic capacitors and exhibit outstanding dielectric properties in the microwave frequency range [91-94], making it a candidate material for ceramic resonators, used for example in wireless communication technology.

In addition to the current application, other TiO₂ structures exhibit interesting optical and mechanical properties and are proposed as candidate materials for functional ceramics. For example, the cubic high pressure polymorph of TiO₂ may be used as light absorber in solar-energy conversion [87]; *ab-initio* investigations of the electronic band structure showed important optical absorptive transitions in the region of the visible light, predicting a more efficient performance than the TiO₂ forms used so far.

Furthermore, the cotunnite phase (CN=9) is a candidate material for new noncarbon abrasive materials. *Dubrovinsky et al.* [11] presented a bulk modulus value of $K_0=431$ GPa and a hardness of 38 GPa, exceeding the values for WC (421 and 30 GPa, [95]) and cubic BN (369 and 32 GPa, [96]). It is likely that the OI phase (CN=7) and the cubic phase (CN=8) are also ultrahard substances (compare [57]).

4. Tuning of Elastic Properties

In industrial technologies using superhard materials for cutting, drilling, milling and polishing there is a need for designing new abrasive materials that are hard, tough, chemically inert and thermally stable. As the hardest materials, covalent ceramics like diamond, cubic boron-nitride and SiC are applied. But also hard oxides play an important role because of their low reactivity with atmosphere, especially at elevated temperatures, which is essential for such applications. The oxide materials that have received attention due to their high hardness, toughness and strength are rutile structured SiO_2 (stishovite), $\alpha\text{-Al}_2\text{O}_3$ (corundum), CVD-produced $\kappa\text{-Al}_2\text{O}_3$, and transformation-toughened ZrO_2 , HfO_2 and TiO_2 [97,98]. As it was already mentioned in the last section, hard TiO_2 structures seem to be very promising for new abrasive materials.

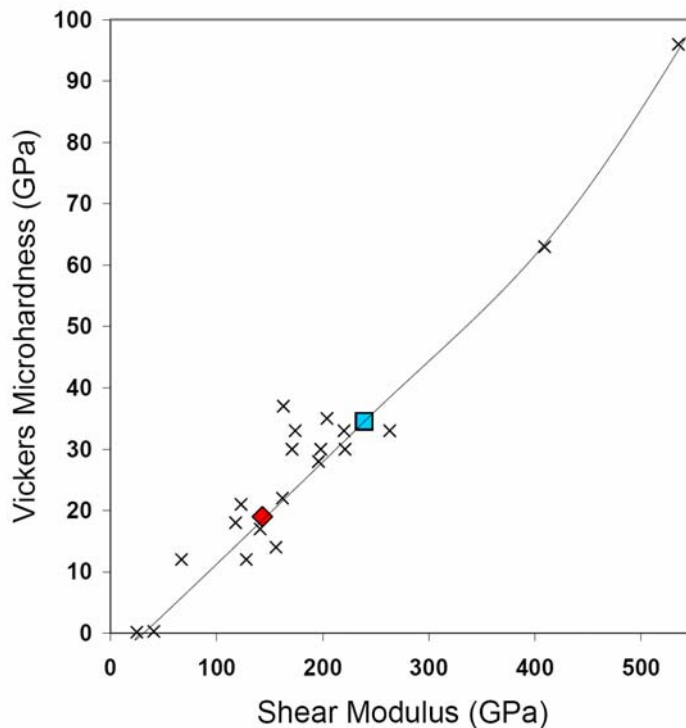


Figure 8: Correlation of shear modulus and hardness, plotted for various materials from ref. [97]. Square and diamond symbols are computational data for TiO_2 fluorite and pyrite from ref. [57].

The hardness of a material is correlated to its bulk modulus and shear modulus. Figure 8 shows, how well the shear modulus can be used as indicator for the hardness of a material. Data are presented for various materials [97] as well as for pyrite and fluorite forms of TiO_2 [57]. Unfortunately, the determination of the shear modulus is not possible for high pressure polymorphs. We therefore have to take the bulk modulus as a substitute for an indicator of the hardness. The definition of the bulk modulus and how to determine the equation of state experimentally and computationally is described in chapter II. section 4. “Compressing Materials: Equation of state”.

There are several possibilities to alter the elastic properties of a given material. Experimental data and theoretical predictions suggest that the values of the bulk modulus K_0 of the TiO_2 high pressure polymorphs increase with an increasing Ti-O coordination number. The 9-fold coordinated cotunnite structured phase is therefore the hardest of TiO_2 polymorphs, and of oxides known in general. One tool of creating new hard materials is therefore to synthesize the dense high pressure polymorphs and to stabilize them at ambient conditions. As one promising way to do that, doping of TiO_2 with ZrO_2 is proposed. The crystal chemistry of both, titanium and zirconium dioxides are similar and it is known that high pressure zirconia polymorphs (OI and OII) are quenchable. It is also well known that the ZrO_2 tetragonal and cubic high temperature polymorphs can be stabilized at ambient conditions by doping with other cations, such as Ca, Mg or Y. With a similar principle, the stabilization of high pressure polymorphs of the $(\text{Ti}_{1-x}\text{Zr}_x)\text{O}_2$ solid solution is proposed.

The incorporation of other cations is not only a way to stabilize high pressure polymorphs but is a tool by itself to tune elastic properties. The compressibility of high-pressure polymorphs of TiO_2 is systematically smaller than for ZrO_2 (Table 1). For the monoclinic MI phase, K_0 was measured as 290–303 GPa for TiO_2 and as 187–212 GPa for ZrO_2 . The values of K_0 for the orthorhombic phases are 318 GPa (TiO_2) and 243 GPa (ZrO_2) for OI, and 431 GPa (TiO_2) and 265 – 444 GPa (ZrO_2) for OII, respectively (details, nomenclature, and references are given in Table 1). This pattern can be understood by a comparison of the electronic structures of Zr and Ti. Having one more electron shell, Zr has larger ionic and covalent radii than Ti and therefore a higher compressibility. The compression behavior of Ti and Zr oxides is not only controlled by the compressibility of the metal atoms, but also by the distortion of their coordination

polyhedra and of the oxygen atoms. The valence electrons in the d states play an important role in the distortion of the polyhedra [19]. However, to give away the results of this study, it is worth mentioning that our experimental results on Zr-doped nanoanatase gave the highest bulk modulus for anatase ($\text{Ti}_{1-x}\text{Zr}_x\text{O}_2$) reported so far. The doping of TiO_2 with ZrO_2 thus led to hardening of the material.

Table 1: Volumes and bulk moduli of TiO_2 and ZrO_2 polymorphs.

Phase	V_0 (\AA^3)	V_0/Z (\AA^3)	K_0 (GPa)	K'_0	P (GPa)	T (K)	Technique	Ref.
TiO₂								
rutile	62.5	31.2	230(20)	6.6(7)	0-20	300	DAC + XRD	[14]
rutile	62.5	31.2	210(10)	6.6(7)	0-8	300	MA + XRD	[19]
rutile (10 nm)			211(7)					[20]
anatase	136.8	34.2	178(1)	4 f	0-8	300	DAC + XRD	[1]
anatase	136.3	34.1	190(10)	5.3(10)	0-14	300	DAC + XRD	[2]
anatase	143.8	36.0	189.5	3.4	0-50	-	<i>ab-initio</i>	[2]
anatase (single cryst.)	136.3	34.1	179(2)	4.5(10)	0-5	300	DAC + XRD	[2]
anatase (30 - 40 nm)	136.2	34.0	243(3)	4 f	0-35	300	DAC + XRD	[4]
anatase (6 nm)	-	-	237(3)	4 f	6-18	300	DAC + XRD	[3]
anatase (6 nm)	-	-	260	4 f	15	-	MD	[3]
anatase (6 nm)	-	-	240	4 f	20	-	MD	[3]
brookite	257.8	32.2	255(10)	4 f	0-8	300	DAC + XRD	[99]
MI	112.2	28.1	290(20)	4 f	10-60	300	DAC + XRD	[14]
MI	112.2	28.1	290(20)	4 f	0-20	300	MA + XRD	[19]
MI	105.1	26.3	304(6)	3.9(2)	30-80	300	DAC + XRD	[1]
MI (10 nm)			235(16)					[20]
α -PbO ₂	122.4	30.6	260(30)	-	0-10	300	DAC + XRD	[14]
α -PbO ₂	122.4	30.6	258(8)	4.05(25)	0-8	300	MA + XRD	[19]
α -PbO ₂			212(25)					[20]
OI	109.1	27.3	318(3)	4 f	19-36	300	DAC + XRD	[9]
OII	105.1	26.3	431(10)	1.35(10)	15-42	300	DAC + XRD	[1]
cubic	115.5	28.9	202(5)	1.3(1)	10-55	300	DAC + XRD	[18]
ZrO₂								
MI	140.6	35.2	212(24)	8(4)	0-70	300	DAC + XRD	[38]
MI	-	-	187	-	0	-	Brill. scat.	[100]
MI	-	-	152	4.00	-	-	<i>ab-initio</i>	[101]
MI	-	-	157	2.38	-	-	<i>ab-initio</i>	[102]
tetragonal (nanocryst.)	139.4	34.9	172(6)	8.5(5)	0-10	300	DAC + XRD	[25]
tetragonal	-	-	205(10)	4 f	0-12.5	1000	MA + XRD	[34]
tetragonal	-	-	200	6.25	-	-	<i>ab-initio</i>	[102]
OI	134.0	33.5	243(10)	7(2)	10-25	300	DAC + XRD	[38]
OI	-	-	273	3.51	-	-	<i>ab-initio</i>	[101]
OI	-	-	272	4.63	-	-	<i>ab-initio</i>	[102]
OII	123.2	30.8	444(15)	1 f	0-70	300	DAC + XRD	[38]
OII	120.1	30.0	265(10)	4 f	0-24	300	MA + XRD	[34]
OII	120.1	30.0	296(5)	1 f	0-24	300	MA + XRD	[34]
OII	120.9	30.2	306(10)	3.66 f	0-50	300	DAC + XRD	[27]
OII	120.9	30.2	322(8)	2.3(4)	0-50	300	DAC + XRD	[27]
OII	120.0	30.0	278(11)	3.70(22)	0-100	300	DAC + XRD	[32]
OII	120.0	30.0	267(3)	4 f	0-100	300	DAC + XRD	[32]
OII	-	-	314	3.66	-	-	<i>ab-initio</i>	[101]
OII	-	-	305	4.68	-	-	<i>ab-initio</i>	[102]

K_0 = isothermal bulk modulus; V = elementary cell Volume; Z = number of TiO_2 or ZrO_2 per elementary cell; DAC = diamond anvil cell; XRD = *in-situ* X-ray diffraction; MA = multianvil; MD = Molecular Dynamics; LD = Lattice Dynamics; Brill. Scat. = Brillouin scattering; f = fixed value;

The compression behavior of a material is furthermore controlled by the microstructure as well as stress and strain in the crystallites. Size dependent modifications of mechanical properties are described by the Hall-Petch effect [103,104], stating that hardness and yield strength increase with decreasing crystallite size:

$$\tau = \tau_0 + kd^{-1/2} \quad (1)$$

where τ is the yield stress, τ_0 is the friction stress needed to move individual dislocations, k is a constant (often referred to as the Hall-Petch slope) and is material characteristic, and d is the average grain size. The hardening of the nanoscale materials is related to the fact that such small crystallites are free of dislocations and therefore do not exhibit dislocation-creep upon compression. That way, an important tool for shearing is not possible in nanoscale compared to microscale material, leading to an increase of the shear-modulus. *Nieh et al.* [105] reformulated the effect for nanocrystalline materials using the Vicker's hardness H as a function of the crystallite size d :

$$H=H_0+K/\sqrt{d} \quad (2)$$

In contrast, *Schiotz et al.* [106] describe materials which get softer as the crystallite size decreases after a certain critical size, referred to as the reverse Hall-Petch effect.

A decrease in crystallite size leads to a higher bulk modulus for anatase, as shown by *Swamy et al.* [1,4]. The authors carried out experiments on the compression behaviour of macrocrystalline anatase [1] up to 8 GPa as well as of nanocrystalline anatase [4] up to 35 GPa and determined the isothermal bulk modulus for macrocrystalline anatase to be 178(1) GPa. The value for the nanocrystalline counterpart is 243(3) GPa, which is about 35% larger. The results suggest that stress hardens the material. In Table 1, the volumes, densities and equation of state data are presented for TiO_2 and ZrO_2 polymorphs with various crystallite sizes.

Stress and strain also vary the pressure of transformation from one polymorph to the other and therefore might be another tool for stabilization of high pressure polymorphs upon decompression or low pressure polymorphs upon compression. A decrease in crystallite size apparently suppresses the formation of TiO_2II and leads to a higher pressure limit of the transformation anatase \rightarrow MI. New experimental results on TiO_2 are reported in chapter III. section 4.

5. Computational Work

Experiments on the TiO₂ system have been complemented by a large number of computational studies on structural [9,21,107-118] and electronic properties [119-125]. A wide range of computational approaches have been used in these studies, with varying degrees of transferability and efficiency of the methods. On the more efficient side, a number of interatomic potential models were developed for atomistic simulations of titanium oxides [9,107-113,126], primarily applied to lattice dynamics (LD) and molecular dynamics (MD) computations. Among the various potentials derived, a number is well transferable [108,113] and LD and MD computations are successful in describing the relative stabilities of phases in pressure and temperature.

However, to describe electronic properties of a material, such as the band structure or electronic densities of states, *ab-initio* methods must be considered, even though they are computationally more demanding. In order to solve the Kohn-Sham (KS) equations for the solid [127], many-body interaction of the electrons through exchange and correlation need to be approximated. Hartree-Fock (HF) theory calculates the exchange energy exactly, but does not account for correlation [114,115]. In contrast, in the local density (LDA) [128] and generalized gradient approximation (GGA) [129], both exchange and correlation are approximated. Computations using LDA and GGA are typically referred to as density functional theory (DFT) computations. For Ti as a light transition metal ion, the correlation of electrons plays an important role, as has been pointed out in the literature. *Rościszewski et al.* [114] found that the correlation energy does not change linearly upon (de)compression, making it impossible for HF computations to predict the compressibility of rutile accurately. Only the lattice constants of the equilibrium geometry are reproducible. *Reinhardt et al.* [115] performed a comparative study on rutile using HF as well as DFT with LDA. They found that the latter one gives a good estimate for the binding energy whereas HF only provides 70% of it. The results show that HF is an inappropriate method for computations on TiO₂.

In DFT methods, either all electrons in the systems can be considered explicitly or the potential can be approximated by a pseudopotential. A large number of *ab-initio*

computations were performed in order to reveal the structures, bulk moduli and relative stabilities of TiO₂ polymorphs. *Sasaki* [21] applied GGA and a pseudopotential that was constructed for the electron configuration of the groundstate of Ti⁴⁺, having a partial core correction incorporated in the evaluation of the exchange-correlation energy. Phase transformations occurred in the same order as seen experimentally, from rutile to TiO₂II - brookite; however, anatase was not considered. *Dewhurst and Lowther* [116] used Troullier-Martin-pseudopotentials with LDA and included anatase in the structures. They found rutile more stable than anatase. In fact, anatase was the phase with the highest energy among the phases considered. In contrast, *Muscat et al.* [117] used the all-electron linear combination of atomic orbitals (LCAO) and pseudopotential (PS) methods as well as HF theory to compute the optimal crystal structures at various pressures. As a result, anatase was predicted more stable than rutile. *Labat et al.* [118] performed a detailed analysis of the structural and electronic properties of rutile and anatase, applying HF as well as density functional calculations using the hybrid HF/KS schemes, LDA and GGA. The authors report excellent agreement with experimental band structures as well as structural descriptions, but again anatase was found more stable than rutile.

6. Motivation and Outline

The goal of the current work is to examine the effect of crystallite size and Zr-doping on the compressibility and the transition behavior of rutile and anatase. It was found before that a decrease of the crystallite size to the nanometer range leads to stiffening of the material and here we investigate if this hypothesis applies to pure and Zr-doped anatase and rutile. From experimental data it is inferred that high pressure polymorphs of TiO_2 have a higher bulk modulus than the analogous ZrO_2 polymorphs. In this study, the bulk moduli of doped and undoped phases are determined and the study demonstrates that Zr-doping leads to a stiffening of nanoscale anatase. It was found before that a decreasing crystallite size to the nanometer scale leads to a higher transformation pressure of anatase and rutile to TiO_2II , which is confirmed here. A detailed comparison of the transition behavior of micro- and nanoscale doped and undoped forms of rutile and anatase is given below.

For the synthesis of starting materials for the experiments, a route of the sol-gel method was developed and hydrothermal experiments were performed. In order to determine the maximum amount of Zr-doping possible, experiments at pressure up to 10 GPa and temperatures up to 1600°C were performed. The experiments showed that ≤ 10 mole% of ZrO_2 can be incorporated into the structure of rutile and the high pressure polymorphs. Therefore, the Zr-doped samples used in compression experiments had the composition $\text{Ti}_{0.9}\text{Zr}_{0.1}\text{O}_2$.

II. Methods and Instrumentation

In this study, two kinds of experiments at high pressures and high temperatures (HPHT) were performed: First the materials synthesis of $\text{TiO}_2\text{-ZrO}_2$ materials and second diamond anvil cell (DAC) experiments with *in-situ* observation and data collection upon compression and decompression. For synthesis experiments at HPHT, the piston cylinder, multi anvil and hydrothermal apparatus were chosen and recovered samples were analyzed by means of powder X-ray diffraction (XRD), microprobing and transmission electron microscopy (TEM). Compression experiments were carried out in the DAC and *in-situ* XRD, X-ray absorption (XAS) and Raman spectroscopic measurements were performed. In section 1 and 2, high pressure experimental techniques as well as analytical methods are described. The theoretical approach to calculate energetics and structures of TiO_2 polymorphs is reported in section 3. In experiments and computations, the compression behavior was analyzed in detail and therefore, some theory about the compressibility is given in section 4, reviewing basic terms of elasticity and the concept of finite strain.

1. High Pressure Experimental Techniques

There are numerous methods for performing experiments at high pressures and high temperatures, used for synthesis as well as *in-situ* studies of materials at extreme conditions [130]. As a general rule, one can state that the higher the pressure achieved, the smaller the sample volume has to be. With the piston cylinder apparatus, pressures up to ~ 5 GPa and temperatures up to 2200°C can be achieved, with a sample volume of typically ~ 200 mm^3 . The piston-cylinder press is durable and robust, and controls the high pressures and temperatures over long periods of time, days to even weeks. Compared to that, the multi-anvil apparatus can produce much higher pressures. Depending on the choice of cubes and load, up to 25 GPa can be achieved at up to $\sim 2000^\circ\text{C}$, and the conditions can be controlled for time periods of several hours. The sample volumes are between 14 mm^3 for lower pressures and ~ 6 mm^3 for higher

pressures. In contrast, in the DAC, a maximum static pressure of ~ 300 GPa can be reached. At intermediate pressures, the DAC can be heated by electrical resistive heating (internal or external) to about 1000°C or internal laser heating to about 3000°C . However, sample volumes are as small as 0.0002 mm^3 .

The choice of *in-situ* measurements possible is highest for DAC experiments. Diamonds are transparent for electromagnetic radiation in a broad energy range, allowing for optical, near-infrared and X-ray analytical methods. Depending on the design and the choice of materials, multi anvil presses can allow for *in-situ* X-ray diffraction, but are limited for other *in-situ* techniques. The piston cylinder apparatus lacks the possibility for *in-situ* X-ray diffraction.

1.1. Hydrothermal Experiments

Hydrothermal experiments were performed in cold-seal pressure vessels, at pressure and temperature conditions, where H_2O is in the supercritical state, allowing for generally high dissolution rates. The system is shown in Figure 9 and described elsewhere [131-133].

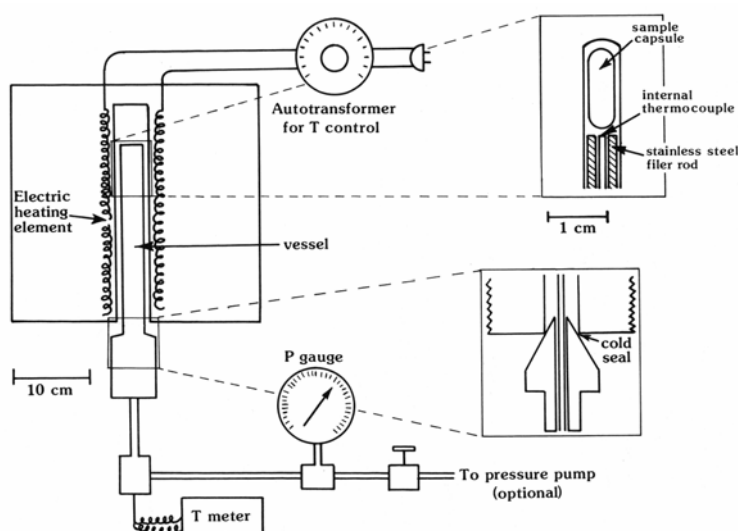


Figure 9: Schematics of a cold-seal pressure vessel and system. The pressure vessel is externally heated, while the seal is cooled. Pressure is generated by an external pressure pump and held constant by closing the valve when run conditions are reached. Temperature is controlled by a thermocouple situated close to the sample capsule. From ref.[134].

Experiments were performed in Au capsules with the diameter of 2.0 mm and a length of 10 mm. The capsules were cut from seamless tubing, washed in concentrated hydrofluoric acid, repeatedly rinsed in distilled water, cleaned with alcohol in an ultrasonic bath and annealed to yellow-orange color over a Meeker burner. Capsules were crimped and welded flat, filled with distilled and deionized water and ~30 mg sample powder, yielding 5 wt% H₂O. Capsules were crimped and welded immediately with a trefold. During welding, capsules were partly submerged in a bath of cold water and ice to prevent loss of H₂O. In all cases, weight loss during welding was 0.04–0.08 mg; For the same method, *Dolejš and Baker* [135] report that piercing the welded capsule and determining the weight loss by drying revealed no loss of H₂O within the weighing error (0.02 mg). Capsules were stored at 120°C for 1 h to ensure homogeneous distribution of H₂O vapor and re-weighed to check for leakage. Experiments were carried out in cold-seal pressure vessels, using air as pressure medium. Temperatures were monitored by external chromel-alumel thermocouples, calibrated against the melting point of NaCl (800.6°C). Individual temperatures are accurate to ±2°C. Pressure was measured with the Bourdon-tube gauges, calibrated against a factory calibrated Heise gauge. Pressure data are precise to ±2 MPa. The experiments were terminated by placing the vessel in an air jet and quenched below the solidus temperature in 1–2 min. All capsules were checked for leakage, opened and stored at room conditions.

1.2. Piston Cylinder Technique

The piston cylinder technique works by the principle of pressure amplification, where in the so called master ram a small load on a large piston is converted to a relatively large load on a small piston. Additionally to the master ram, the type of piston-cylinder apparatus used here is end-loaded, having a second hydraulic ram to vertically load and hence strengthen the pressure vessel in which the sample is located (Figure 10).

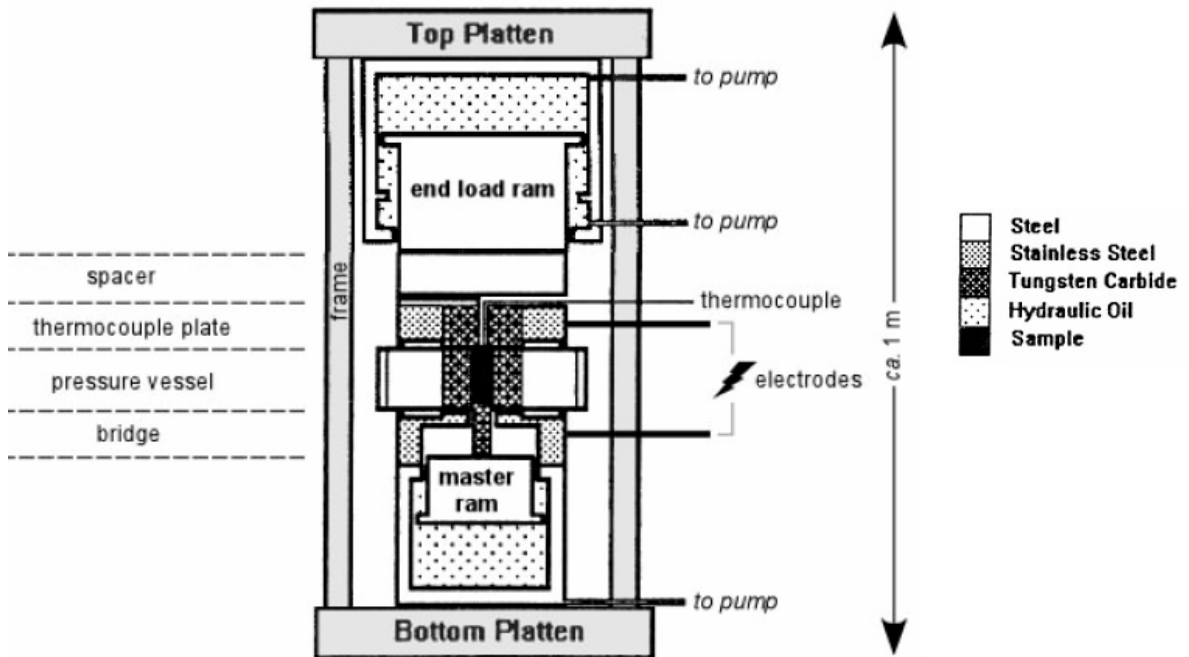


Figure 10: Cross-section of an end-loaded piston cylinder apparatus. The sample is situated in the pressure vessel and compressed by applying force on the master ram. The end load ram serves to strengthen the pressure vessel. The sample is heated by electrical resistance. Redrawn after ref. [136].

The sample assembly contains NaCl as solid pressure medium, a graphitic resistance heater, and the sample, which is surrounded by a Pt-capsule and placed into the hot spot of the assembly (Figure 11). A large voltage is applied to the steel plates above and below the pressure vessel and passed across the resistance heater to heat the sample, while the temperature is monitored with a s-type thermocouple placed close to the sample. During an experiment, pressure vessel, bridge and upper plates are cooled by a circulating water system.

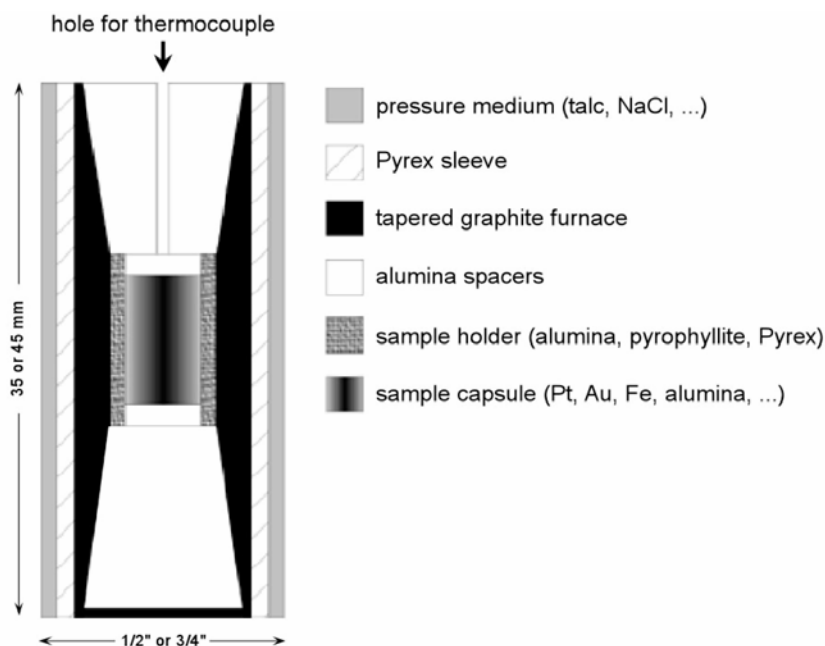


Figure 11: Cross section of the sample assembly for piston-cylinder experiments.

In all experiments, samples were compressed to 90% of the target run pressure and then heated. The pressure of the heated sample was adjusted to the target pressure and automatically controlled during the run time. Samples were quenched by switching off the heating power, followed by manual decompression.

1.3. Multi Anvil Technique

In the multi anvil apparatus, the force of a hydraulic press is exerted onto a set of six steel anvils, forming a cubic cavity, in which eight tungsten carbide (WC) cubes are placed. The corners of the WC cubes are truncated to form an octahedral pressure chamber, filled by an MgO octahedron that contains the sample capsule (Figure 12). Details of the technique are described elsewhere (e.g. ref. [137-140]).

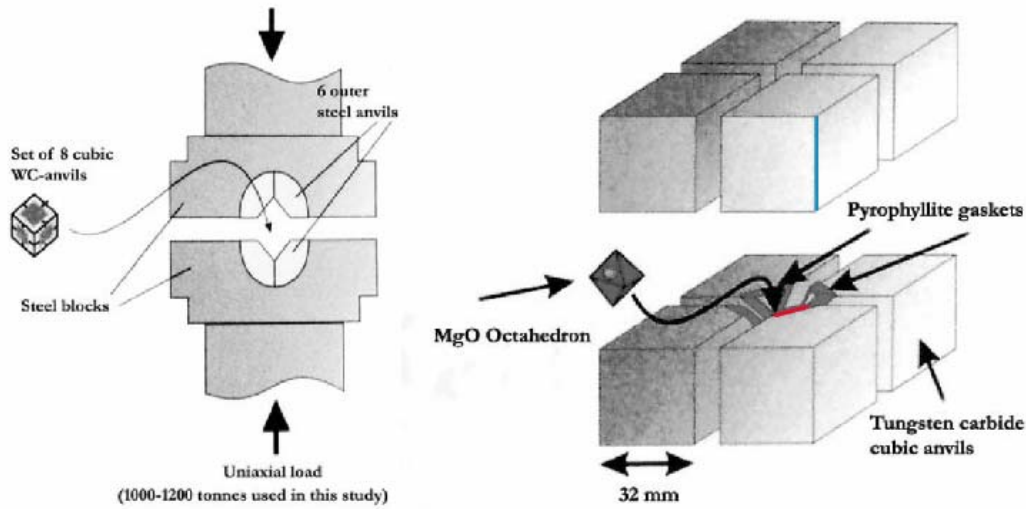


Figure 12: Schematic of the multi-anvil setup. On the left, two steel blocks are shown, forming a cubic cavity and enclosing a set of eight WC-anvils. On the right, the eight WC cubes are shown in detail, having truncated corners to form an octahedral void in which the sample is situated. The truncation edge length (TEL) of the cubes is marked in red, the octahedron edge length (OEL) is marked in blue.

Several assemblies exist with varying octahedron edge length (OEL) and truncation edge length (TEL) of the cubes. The maximum pressure that can be reached in an experiment increases with decreasing OEL and TEL, and thus with decreasing sample size. For the experiments here, WC cubes with OEL = 10 mm and TEL = 5 mm were used, allowing to squeeze the sample to 10 GPa (Figure 13).

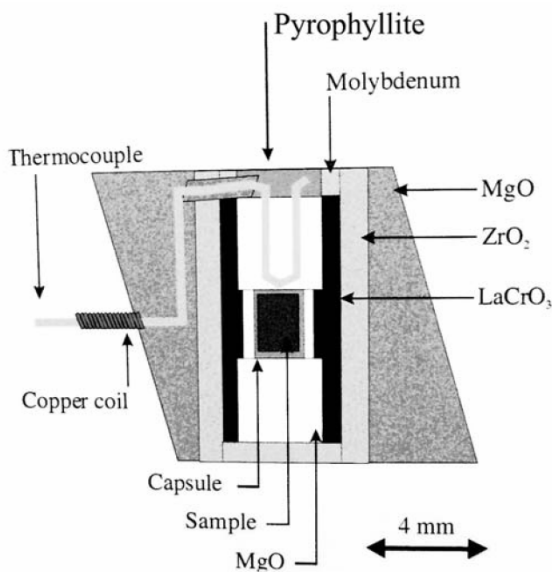


Figure 13: Pressure assembly of a multi anvil experiment.

The octahedron is made of MgO doped with 5% Cr₂O₃ to reduce heat loss by radiation. The sample is surrounded by a Re-capsule, which again is surrounded by an MgO cylinder and placed into the hot spot of a cylindrical graphite resistance heater, which is insulated from the octahedron by a zirconia sleeve. The capsule, made from 0.25 mm thick Re-foil, has a diameter of 1.6 mm and a length of 3.5 mm. The sample temperature is monitored using a W₇₅Re₂₅-W₉₇Re₃ thermocouple, which is placed in contact with the capsule. Pressures are calibrated using known phase transitions of common minerals (compare ref. [141]), with an uncertainty of ~1 GPa. The thermal gradient along the capsule at 1600°C and 10 GPa is ±50°C [142].

Multi-anvil experiments were carried out using the 1-Cylinder Sumitomo Press with axial force of 1200 t. In all experiments the samples were compressed to the run pressure and then heated at the rate of ~100 °C/min. The samples were quenched by switching off the heating power and cooled at a rate of 1000 °C/s, followed by slow pressure quenching, lasting up to 15 hours.

1.4. Diamond Anvil Cell

In the diamond anvil cell (DAC), the pressure chamber is made by a drilled hole of a metal foil, which is placed between the polished culets of two diamonds. The diamonds are seated on supporting plates, such that even moderate force on the plates lead to very high pressures on the sample chamber. There are a number of different types of DAC designs (for details see refs. [143-147]). The DAC design used for experiments of this study is described in detail by *Dubrovinskaia and Dubrovinsky* [148] and the principle is shown in Figure 14. For this study, a pair of 1/4 karate type IA diamonds with a culet size of 250 µm or 300 µm was used. The gasket was made from Re-foil with a thickness of ~250 µm, which was indented between the diamonds to 40–60 µm. Using electrical erosion, a hole with diameter of 80–100 µm was drilled in the middle of the indented area to form the pressure chamber.

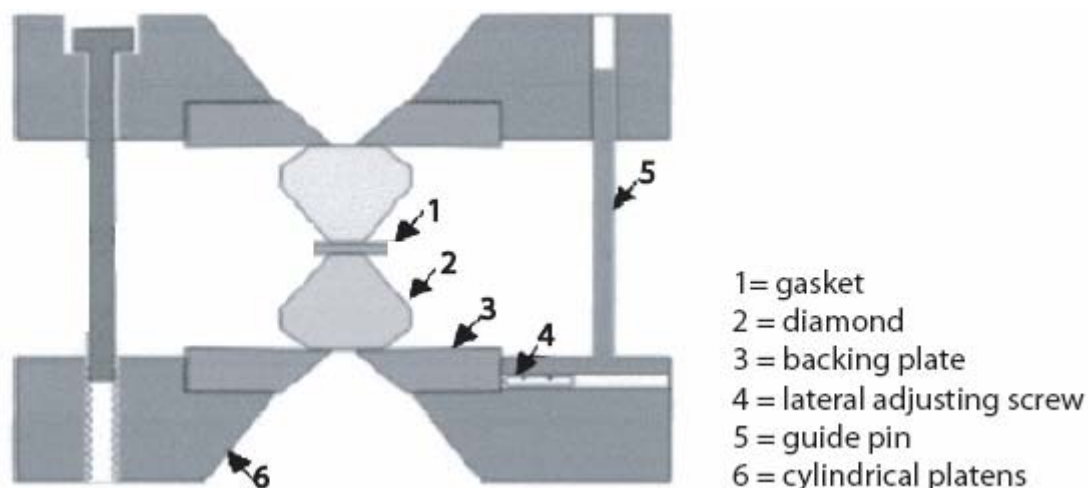


Figure 14: Schematic of a diamond anvil cell used at BGI. Redrawn after ref. [148].

For Raman studies, a small ruby sphere served as pressure calibrant, and the shift of the fluorescence line was used to determine the pressure, following the method described by *Mao et al.* [149]. For X-ray diffraction studies, a small piece of Cu-wire served as internal pressure calibrant, when the pressure transmitting medium was absent. When deviatoric stresses in the sample needed to be minimized by the use of a transmitting medium, LiF was chosen. LiF is a chemically stable soft material with low shear strength, and serves as both, pressure transmitting medium and pressure calibrant in X-ray diffraction experiments, exhibiting low absorption and a low scattering factor for *in-situ* measurements through the DAC.

The DAC can be heated using either electrical resistive (e.g. [148]) or laser heating [150-153]. In this study, samples were heated using the Nd-YAG laser ($\lambda=1.064$ μm and power above 20 W), as provided at the synchrotron facility at the advanced photon source (APS) in Argonne, Illinois, [154].

2. Analytical Methods

2.1. Powder X-Ray Diffraction

To determine the lattice parameters and atomic coordinates of the crystalline samples, two types of angle-dispersive XRD analysis were performed, *in-situ* studies on DAC experiments as well as characterization of synthesized samples. The latter was done at BGI on a the Siemens D5000 diffractometer (Cu $K\alpha_2$ radiation, $\lambda=1.542 \text{ \AA}$), or a Phillips X'Pert diffractometer (Co $K\alpha_2$ radiation, $\lambda=1.78897 \text{ \AA}$). The sample was ground and mixed with Si powder in proportion of $\sim 1:0.2$, serving as calibrant. The principles of the technique can be found in ref. [155]. Full profile refinements of the diffraction patterns were performed using the General Structure Analysis System (GSAS) program [156,157]. *In-situ* measurements of DAC experiments were performed at the high brilliance X-ray system at BGI, using Mo $K\alpha$ radiation ($\lambda=0.7105 \text{ \AA}$) and a CCD Bruker APEX detector, or at a synchrotron facility, using flexible radiation with wavelength of $\sim 0.3 \text{ \AA}$ and a MAR345 image plate. Experiments were performed at the Swiss Norwegian Beamline at the European Synchrotron Radiation Facility (ESRF), Grenoble, France, together with Prof. Vladimir Dmitriev, and at GeoSoilEnviroCARS 13 BMD at the Advanced Photon Source (APS), Argonne, Illinois, together with Dr. Vitali Prakapenka. The diffraction images were integrated using the FIT2D program [158], where CeO_2 was used to determine the distance of the sample from the detector along with other fitting parameters necessary. GSAS was used for full profile refinement of the integrated patterns, an example is shown in Figure 15.

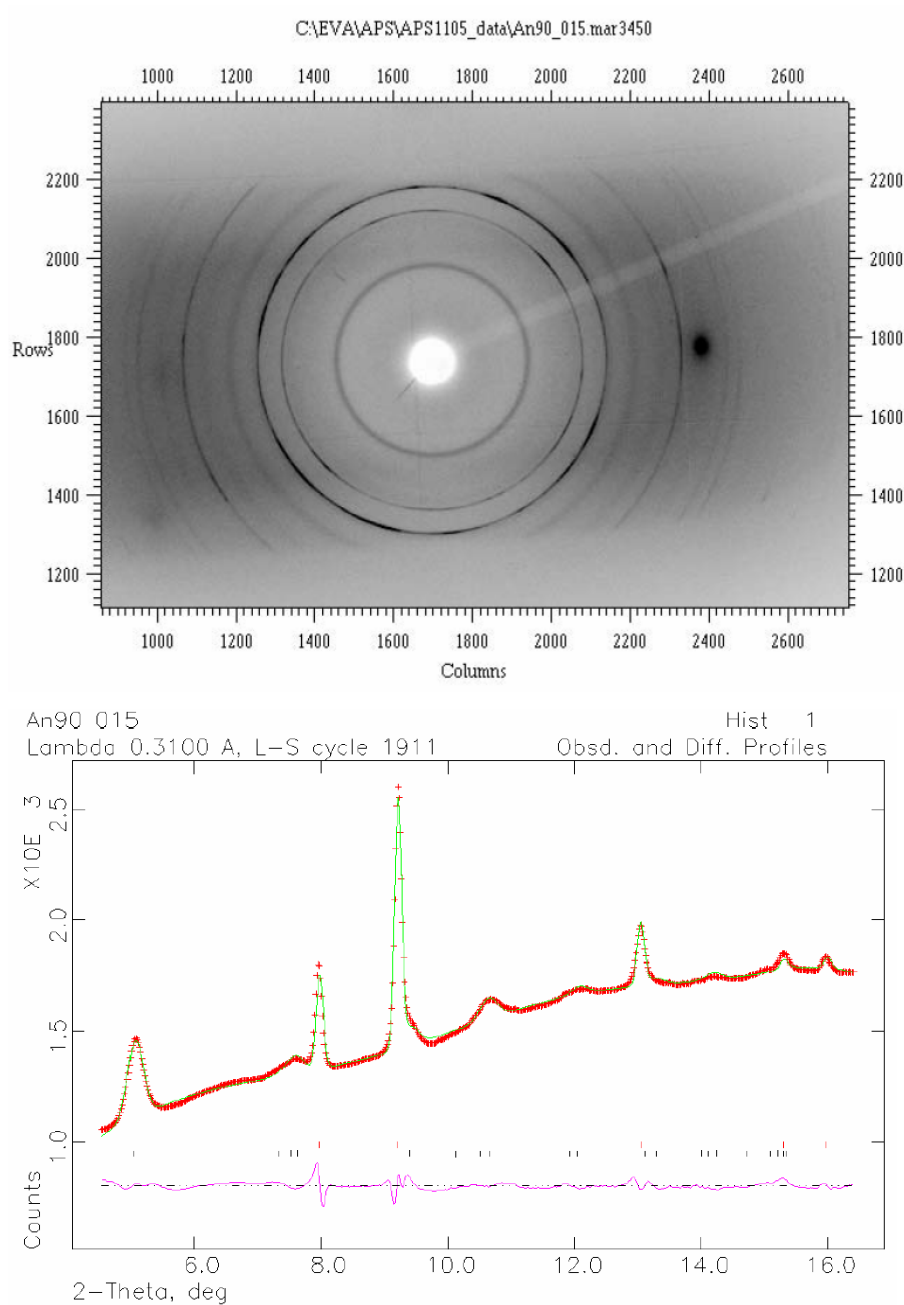


Figure 15: Processing of XRD data from imaging plates. On the top, an image from MAR345 detector of $LiF + Zr_{0.1}Ti_{0.9}O_2$ at 13 GPa ($\lambda=0.31$) is shown before integration. On the bottom, the result of full profile refinement is shown for the same spectrum, upper tickmarks indicate LiF and lower tickmarks indicate anatase $Zr_{0.1}Ti_{0.9}O_2$.

To determine the crystallite size and the strain of a sample from XRD data, the TOPAS-ACADEMIC software [159] was used for convolution-based profile fitting [160] and refinement of the microstructure. The diffraction spectrum of a CeO_2 standard was used to determine the source emission profile and instrumental contribution to peak broadening. The effects of crystallite size and strain on the peak broadening were

analyzed using the double-Voigt approach [161]. Integral-breadth based volume-weighted mean column height L_{Vol_IB} of coherently diffracting domains as well as mean strain values e_0 [160] were obtained simultaneously. The estimate of crystallite size from L_{Vol_IB} depends on the particular crystallite shape and on the size distribution of the crystallites. For monodisperse spherical crystallites with diameter D , the following equation is applicable: $D = 4/3 L_{Vol_IB}$ [162,163].

2.2. X-Ray Absorption Spectroscopy

X-Ray Absorption Spectroscopy (XAS) is generally used to determine the local atomic and electronic structure of atoms, in our study that of Ti atoms. Absorbing X-rays of energies close to the electron binding energy, the absorption spectra of an atom shows specific features, the absorption edge, which is divided into three regions: The pre-edge region just before the edge, the X-Ray Absorption Near-Edge Structure (XANES) and the Extended X-Ray Absorption Fine Structure (EXAFS). The XANES region is extended to 50-100 eV beyond an absorption edge and is determined by the local density of vacant states of an absorbing atom, as well as multiple-scattering effects, while the EXAFS region is extended to up to 2000 eV beyond the edge and is dominated by single scattering processes [164]. High quality XANES spectra were recorded *in-situ* upon compression of the material in a DAC for several pressures across the phase transition. It was shown before that pre-edge features observed at the K edge of the Ti atom are very sensitive to the distortion of the local environment around the Ti atom [165-167], and that displacement of the Ti atoms from their centrosymmetric positions leads to the appearance of an additional peak due to transitions into unfilled atomic d level. The transition from the s to d states is forbidden in the electric dipole approximation and is usually very weak because its existence is only due to a small electric quadrupole matrix element in the absorption cross section. However, the Ti atom displacement from the cubic site breaks inversion symmetry and induces a mixing of p and d states, thus introduces a large dipole transition. The intensity of this peak is therefore a direct probe of the local displacement of this atom [165,166]. K edge measurements serve well to distinguish between different phases.

Ti K-edge measurements were performed in the transmission geometry at beamline ID12 of the ESRF [168]. The experimental conditions and the sensitivity of the measurement are reported in ref. [169]. In order to enhance the intensity of the transmitted beam, a DAC was used with thin diamonds, which were mounted on fully perforated diamond anvils [170,171]. In order to minimize deviatoric stresses on the sample, siliconoil was used as pressure transmitting medium.

2.3. Raman Spectroscopy

Raman scattering occurs due to the excitation of vibrations of atoms or molecules in the sample when the frequency of the electric field applied equals the eigen frequency of the corresponding vibration. A charge separation is induced during the interaction with radiation while the electron shell is displaced as a response to the external field. The number of observed Raman bands as well as the eigen frequencies, relative intensities, widths and polarization of vibrational bands are controlled by the sizes, valences and masses of the atomic species, the bond forces between the vibrating atoms and the symmetry of their arrangement in the crystal structure (e.g. ref.[172]). Raman spectroscopy serves as an important tool for *in-situ* phase identification and characterization upon compression and heating during DAC experiments [173-175].

Raman scattering measurements were performed on a LABRAM Raman spectrometer with a He-Ne laser (632 nm). The spectrometer was calibrated using the Γ_{25} phonon of Si. The vibrational peaks were analysed using the PeakFitTM program by Jandel Scientific and the Savitsky-Golay data-smoothing algorithm was used for peak analysis. The peak profiles were described by combinations of Lorentzian and Gaussian functions.

2.4. Electron Microprobe

Electron microprobing is a common tool for materials analysis; details about the method can be found elsewhere, e.g. refs. [176,177]. All samples were mounted in epoxy resin and polished. Samples and epoxy mounts are non-conductive and were

therefore carbon coated to ensure conduction of the beam electrons away from the sample. All samples were analyzed on the JEOL JXA-8200 electron microprobe at BGI. In order to identify the phases and to achieve knowledge about which elements are present in each phase, Energy Dispersive Spectrometry (EDS) was used to obtain qualitative spectra. The EDS software is equipped with a marker database for K-, L-, and M-lines for peak identification. The chemical compositions were analyzed using Wavelength Dispersive Spectrometry (WDS) with a 10 nA beam current and an accelerating voltage of 15 kV. The instrument was calibrated on a natural rutile standard for TiO₂ and natural zircon standard for ZrO₂. The CITZAF correction package of Armstrong [178] was used to reduce the data and to obtain quantitative analysis. The atomic number correction of Duncumb and Reed, Heinrich's tabulation of absorption coefficients, and the fluorescence correction of Reed were used to obtain a quantitative analysis [178].

2.5. Transmission Electron Microscopy

Details about Transmission Electron Microscopy (TEM) technique can be found in refs. [179,180]. The microstructure of the sample as well as crystal structures were investigated by High Resolution Transmission Electron Microscopy (HRTEM), a phase contrasting imaging technique where the contrast is due to differences in the electrostatic potential in the crystal. Analysis was done on the analytical Philips CM20 FEG scanning TEM at BGI as well as on the FEI TecnaiTM G² F20 X-Twin TEM at Geoforschungszentrum Potsdam (GFZ), using accelerating voltage of 120–200 kV. Samples of nanocrystalline starting material were prepared by dropping of ethanolic solution of the sample onto the grid of a specimen holder. Samples of compressed material after a DAC experiment were prepared by Focused Ion Beam Thinning [181] at GFZ.

3. *Ab-initio* Calculations

Ab-initio all-electron density functional electronic structure simulations were performed on the TiO₂ polymorphs rutile, anatase, brookite, TiO₂II and baddelyite structured phase in order to explore the ground state energetics. The PAW method [182] as implemented in the Vienna *Ab-Initio* Simulation Package (VASP) [129,183] and the LAPW method [184] as implemented in the WIEN2k code [185,186] were used. Computations were performed, using LDA [128] and GGA [129] for VASP and WIEN2k, applying the approximation of *Perdew et al.* [187] as well as WC for Wien2k [188]. WC is a new GGA approximation, developed in the context of Ti-based ferroelectric phases [188]. It may be appropriate for computations on TiO₂, but has not been applied to date. In the plane wave computations, plane wave cutoffs of $E_c = 1000$ eV were included. They have been found necessary for computations on transition metal bearing oxides and silicates. In the LAPW method, the plane waves were expanded up to $RK_{\max} = 9.0$, with uniform muffin tin radii of 1.8 Bohr for Ti and 1.6 Bohr for O for all structures. Crystal structures were optimized for internal and external degrees of freedom at constant volumes, starting from experimental structures. Reciprocal space was sampled on Monkhorst-Pack k-point grids [189], with the product of kpoints \cdot atoms per unit cell > 1944 . Computations were performed for a wide volume range allowing for a reliable equation-of-state fit with a third order finite strain (Birch-Murnaghan) equation-of-state [190]. Results of the study are presented in chapter III. section 6. “Computational ground states of TiO₂”.

Another set of computations, using PAW method with LDA and PBE, was performed to calculate ground state energetics of Ti₈O₁₆ as well as Zr₁Ti₇O₁₆ supercells for varying volumes. The variation of cell parameters as well as energies and atomic positions as a function of the volume were explored. A 2 \times 1 \times 1 supercell was used for anatase along with a Zr doped version of this cell (Zr₁Ti₇O₁₆). Reciprocal space was sampled on a 6 \times 12 \times 4 Monkhorst-Pack k-point grid [189]. Both cells were relaxed for internal and external degrees of freedom, leaving the volume fixed for volumes ranging from 10.0–12.5 Å³ for TiO₂ and 10.0–13.0 Å³ per atom for ZrTi₇O₁₆.

4. Compressing Materials: Equation of State

The change in volume of a material with changing pressure and temperature depends on the isobaric thermal expansion α as well as the isothermal compressibility β such that:

$$V_{T,P} = V_{1,298} [1 + \alpha(T-298) - \beta(P-1)] \quad (3)$$

where α and β are not constant but approximate to a certain value, resulting in finite strain. The isothermal volume change upon compression can be described by a number of Equations of State (EoS). Here, the Birch-Murnaghan EoS for finite strain was used. It is based upon the assumption that the strain energy of a solid undergoing compression can be expressed as a Taylor series in the finite strain, f . The Birch-Murnaghan EoS [190] is based upon the Eulerian strain:

$$f_E = 0.5 [(V_0/V)^{2/3} - 1]/2 \quad (4)$$

and the expansion to third order in the strain yields the Birch-Murnaghan EoS:

$$P = 1.5 K_0 [(V_0/V)^{7/3} - (V_0/V)^{5/3}] \cdot \{1 - 0.75 (4 - K_0') \cdot [(V_0/V)^{2/3} - 1]\} \quad (5)$$

with K_0 = isothermal bulk modulus ($K_0 = 1/\beta (dP/dV)_T$) and $K_0' = dK_0/dP$. In this study, pressure-volume data upon compression of the samples were gained during diamond anvil cell experiments. The data were then fitted to a third order Birch Murnaghan EoS and for some instances to a second order EoS with K_0' fixed to 4, which is typical for most materials. In order to yield estimates for the EoS parameters and their uncertainties in a least square refinement, application of a weighing scheme was necessary. For each data point i , the weight w_i was assigned such that:

$$w_i = \sigma^{-2} \quad (6)$$

where σ^2 is the true variance of the data point, comprised of the contribution from uncertainties in the pressure and volume measurements.

In order to express the relations of P and V linearly, the F - f plot was used. Here, Birch's normalized pressure F was plotted versus the Eulerian strain f_E with:

$$F = P/(3 f_E (2 f_E + 1))^{5/2} \quad (7)$$

The data are described by a third order truncation of the EoS and as an advantage, K_0 and K_0' can be fitted as parameters of a linear function. The slope of such a fit equals $3K_0(K_0'-4)/2$. To calculate f_E (equation 4), V_0 was gained from

experimental data. If no experimental V_0 was available, the refined V_0 was used as fitted by the EoS refinement (equations 5 and 6).

In this study, experimental pressure-volume data obtained from DAC experiments were fitted to Birch-Murnaghan EoS and plotted as F - f . Furthermore, in *ab-initio* computations the internal energy E was calculated for varying pressures. Given that $-P = dE/dV$, it follows that:

$$E(V) = V_0 K_0 / K_0' [(1/K_0' - 1) \cdot (V_0/V)^{K_0' - 1} + (V/V_0)] + \text{const}, \quad (8)$$

allowing for direct comparison of computational and experimental results of K_0 and K' .

III. Results and Discussion

1. *Synthesis and Characterization of Starting Materials*

Due to small sample volumes, experimental studies at high pressures and temperatures require a starting material with distinct stoichiometry that is homogeneous on a nanometer scale. Because TiO_2 and ZrO_2 are poor glass builders, homogeneous mixtures can not be gained from quenching a melt. The typical manufacturing process of mixtures is therefore the sintering of ceramics from oxides or carbonates at temperatures of 1400°C or higher [70,191]. However, such a synthesis path has clear limitations due to the immiscibility of TiO_2 and ZrO_2 , and the very slow diffusion of the solid state reaction. At calcination conditions, there are immiscibility gaps of solid solutions between ~ 30 and ~ 45 mol% TiO_2 and ~ 60 and ~ 90 mol% TiO_2 (compare Figure 7). Samples with relevant compositions will therefore always consist of two phases. The effect leads to inhomogeneous distribution of Ti and Zr atoms, especially when grain sizes are in the μm range or bigger.

1.1. Sol-Gel Synthesis of TiO_2 - ZrO_2 Powders

As an alternative to sintering of oxides, zirconium-titanium oxides were prepared by sol-gel synthesis. There are a number of sol-gel studies with the goal to obtain zirconia-titania powders with high surface energy, e.g. for application as humidity sensors [71,192-195]. The goal of this study was to synthesize a series of amorphous or nanocrystalline materials with a distinct stoichiometry, which are homogeneous on a nanometer scale and free of organic material. Therefore, a route of sol-gel synthesis was established in which temperature and duration of the hydrolysis reaction were optimized, having the following constraints: In order to gain carbon free material, the hydrolysis should last for a long period of time at high temperature. At the same time, diffusion and growth to bigger crystallite sizes was to be hindered, requiring lower temperature and shorter duration of the hydrolysis reaction.

The precursor powders were synthesized as previously reported [196]. 1 mole acetylacetone was added slowly to one mole zirconium-*n*-propoxide, or titanium-*n*-ethoxide, respectively. The yellow solution obtained was stirred at 40°C for one hour. 3 mole distilled water were added and stirred for 30 minutes at 80°C. The solution was distilled by rotational evaporation at 80 mbar air pressure and 80°C. The powder obtained had a concentration of ~53 wt% with respect to the oxide, given from heat loss analysis after heating at 1000°C.

The precursor powders were weighed, yielding stoichiometries of $Ti_x:Zr_{1-x}$ with $x = 0.00, 0.10, 0.25, 0.33, 0.50, 0.67, 0.75, 0.90$ and 1.0 and dissolved in either H₂O- or ethanol-based solutions, so that concentrations were 10 wt% in the sol with respect to the corresponding oxide. The sols were stirred for about one hour until they were clear. In the sols, the Ti and Zr atoms are homogeneously distributed to the atomic scale, ideal for obtaining homogeneous gels and powders. The sols were distilled under rotational evaporation at 80 mbar air pressure and 80°C, obtaining gel powders.

The gel powders were heated at 200°C for one hour, ground in an agate mortar, heated at 200°C for another 30 minutes and ground again. In six portions of ~8 g each, the dried powders were put into ceramic crucibles, placed in a metal chamber of a furnace with the volume of 2110 cm³ and heated to 400°C or 500°C, respectively for 2 hours, while 400 ml of distilled water were sprayed into the chamber and supported the hydrolysis of the material. Afterwards, the samples were heated at the same temperature in the dry furnace for another hour.

In order to study the crystallization behavior of the material synthesized, and to minimize its water content, the samples were annealed at 1400°C for 72 hours.

1.1.1. Purity and Microstructure of Sol-Gel Powders

In order to gain more information about the grain sizes and the texture of the reaction products, HRTEM images were taken. Differential Thermal Analysis (DTA) and ThermoGravimetric Analysis (TGA; Setaram TAG24, Caluire, France) of the powders were performed with a heating rate of 10 K/min in dry air atmosphere. Nitrogen sorption was measured, using an automated volumetric analyser (Model Autosorb 3B, Quantachrome Instruments, Boynton Beach, USA). Prior to nitrogen adsorption analysis, samples were dried at 110°C for 16 h at reduced pressure. The

multipoint-method was used to determine the specific surface area according to Brunauer, Emmet and Teller (BET).

The samples synthesized via sol-gel process are mainly colorless powders, excluding samples with nominally 100 mol% ZrO_2 , which are always dark grey or black and thus, contain small amounts of carbon (<0.5 wt%). Studies by *Bockmeyer et al.* [197] showed that small contents of organic material can be indicated by eye as they lead to a brownish color, at contents greater than 0.5 wt% carbon the samples turn black. The synthesis path using a hydrous sol and a temperature of the hydrolysis reaction of 400°C was most sufficient. Here, colorless and thus, mainly organic free samples of $\text{Ti}_x\text{Zr}_{1-x}\text{O}_2$ within the compositional range of $0.10 < x \leq 1.0$ were produced. The following characterization will therefore focus on these samples. Other paths produced powders with small carbon contents. The study clearly demonstrates that H_2O enhances the hydrolysis reaction, which works best when H_2O is present as steam as well as solvent of the sol.

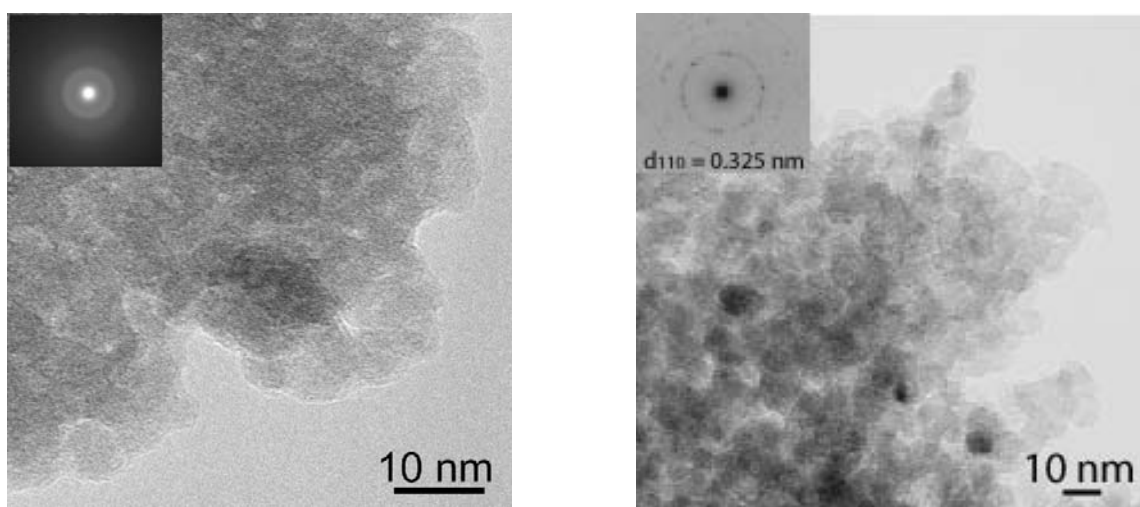


Figure 16: High resolution TEM images of sol-gel samples, hydrolyzed at 400°C from a hydrous sol. On the left: amorphous sample with 50 mol% TiO_2 ; on the right: crystalline sample (anatase) with 90 mol% TiO_2 .

The microstructures of the sol-gel powders were characterized as follows. TEM images of the samples with $x=0.50$ and $x=0.90$, hydrolyzed at 400°C show amorphous and nanocrystalline material with crystallite sizes in the range of 10 to 15 nm (Figure 16). This appearance and the range of grain sizes is representative for other samples. N_2 -sorption experiments on a sample with $x=0.50$ revealed a highly porous microstructure

with a pore volume of $0.16 \text{ cm}^3/\text{g}$, which is typical for sol-gel materials (Figure 17). The type 1 isotherm indicates a microporous network with an average pore diameter of around 1.8 nm.

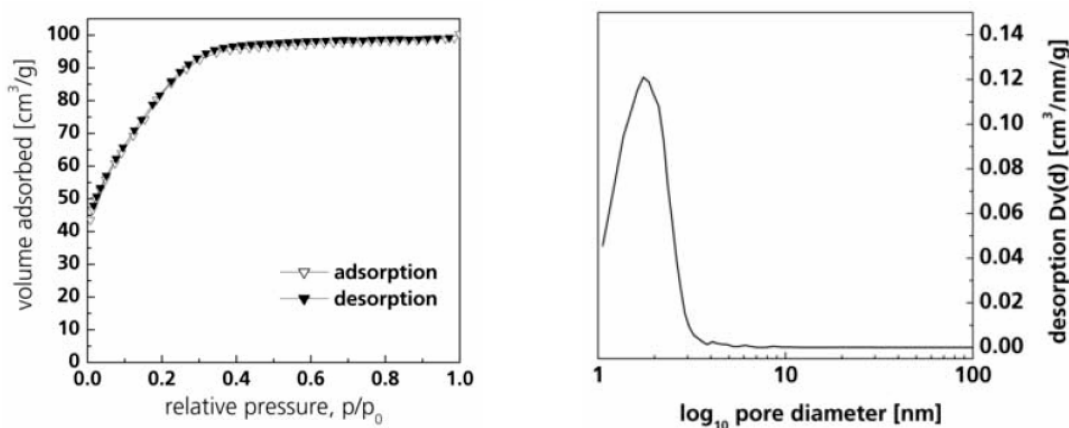


Figure 17: N_2 -sorption of sol-gel sample with 50 mol-% TiO_2 . The pore size distribution (left) shows a highly porous material with a pore volume of $0.16 \text{ cm}^3/\text{g}$, the isotherm (right) indicates an average pore diameter of 1.8 nm.

The results of the TGA and DTA/TG experiments are presented in Figure 18. The total overall mass loss up to 1000°C is 6 wt% and can be separated in two temperature regimes. The first, major mass loss until 250°C of $\sim 5 \text{ wt}\%$ is directly associated with a broad endothermic DTA signal due to the evaporation of adsorbed water in the micropores. The minor mass loss at $T=250\text{-}1000^\circ\text{C}$ of $\sim 1 \text{ wt}\%$ may be explained by decomposition reactions of organic residues or the continued condensation of OH-groups within the material. At a temperature of 717°C , the DTA data show a large exothermic signal (onset at $T=714^\circ\text{C}$), indicating the crystallization of srilankite from the amorphous phase. It can be concluded that the total amount of carbon + H_2O of the sol-gel samples produced is smaller than 1 wt%.

A standard drying procedure at 250°C for 24 h was used to reduce the water content of the powders. The overall mass loss was reduced to $\sim 3\%$, as can be seen from the differential thermal DTA/TG experiments (Figure 18). However, it has to be noted that still a minor endothermic vaporization of water occurs. Also the small weight loss at temperatures $>250^\circ\text{C}$ is still present.

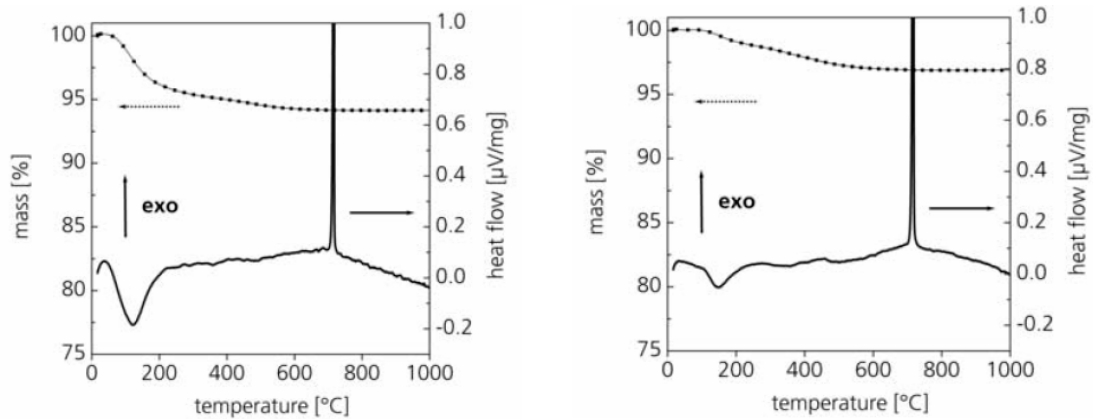


Figure 18: Results of DTA/TG measurements of a sol-gel sample with 50 mol% TiO_2 , before (left) and after (right) drying at 250°C .

1.1.2. Phase Characterization of Sol-Gel and Annealed Powders

XRD patterns show that sol-gel samples with nominal bulk compositions of $x=0.25-0.67$ are amorphous, samples with $x \leq 0.10$ are solid solutions with the structures of cubic zirconia and baddeleyite, and at $x \geq 0.67$ an anatase structured phase appears. The crystalline phases show very broad peaks, indicating crystallite sizes in the nanometer range (Figure 19).

After annealing at 1400°C , samples with nominal bulk compositions of $x \leq 0.33$ contain solid solutions with the structure of baddeleyite, samples with $x=0.33-0.75$ contain a srilankite-structured phase, and with $x \leq 0.90$ solid solutions with the structure of rutile. The very sharp peaks confirm an increase in crystallite size after annealing (Figure 19). Cubic zirconia is not present after annealing and thus, Ti does not stabilize the cubic zirconia phase, as opposed to other cations, e.g. Y. The amorphous intermediate phase transforms to srilankite at a temperature of about 720°C , as indicated by TGK. The temperature of transformation from anatase into rutile was not measured in this study, *Borkar et al.* [198] present a detailed study on the phase transition and give a temperature of 700°C for the onset of the phase transformation for undoped anatase.

III. Results and Discussion

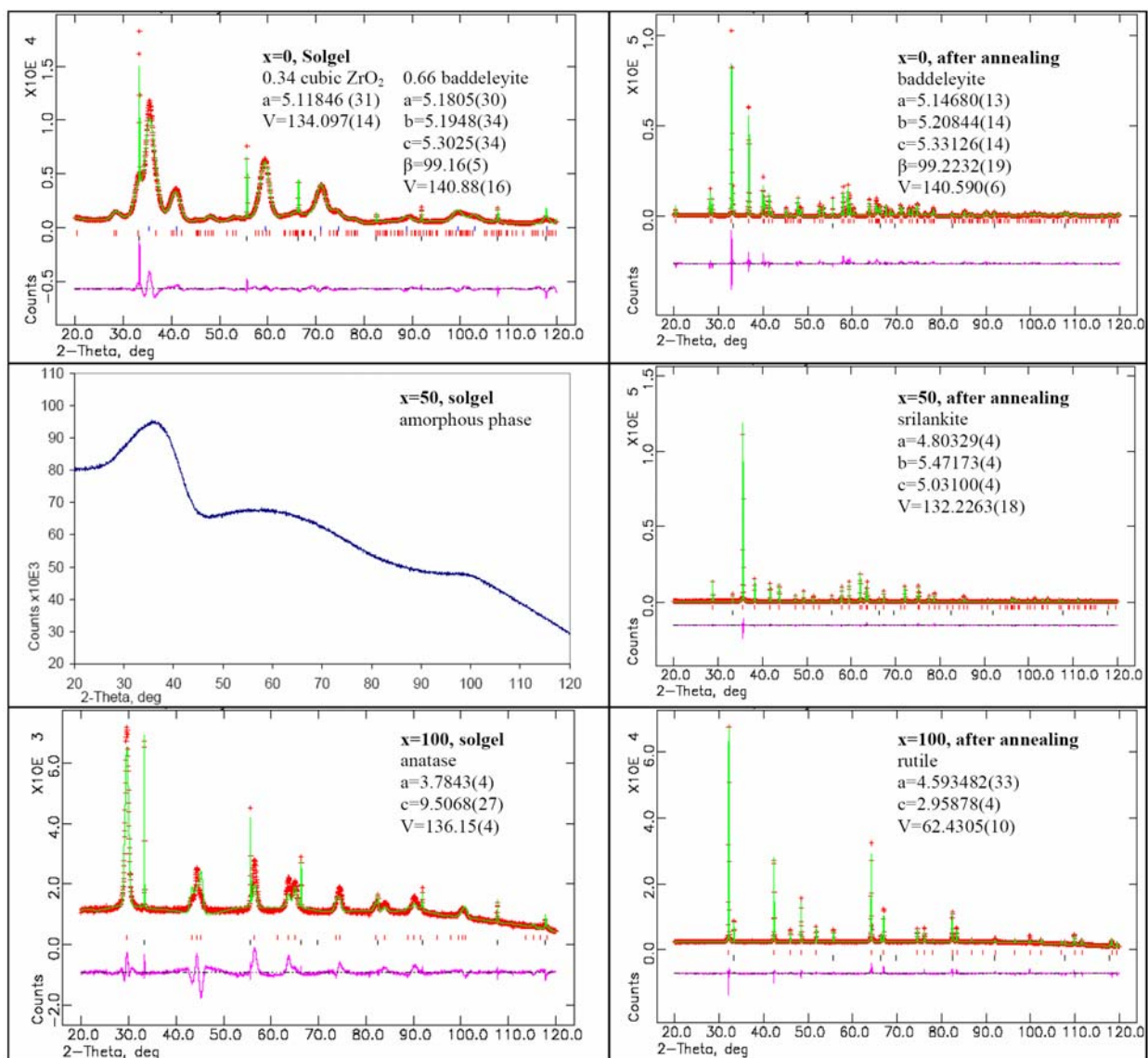


Figure 19: Full profile refinements of X-ray powder diffraction patterns from the samples with $x=0$ (top), $x=50$ (middle) and $x=100$ (bottom) before (left) and after (right) annealing at 1400°C . Patterns were collected using $\text{Co K}\alpha_1$ radiation (1.78897 \AA) with Si as internal standard.

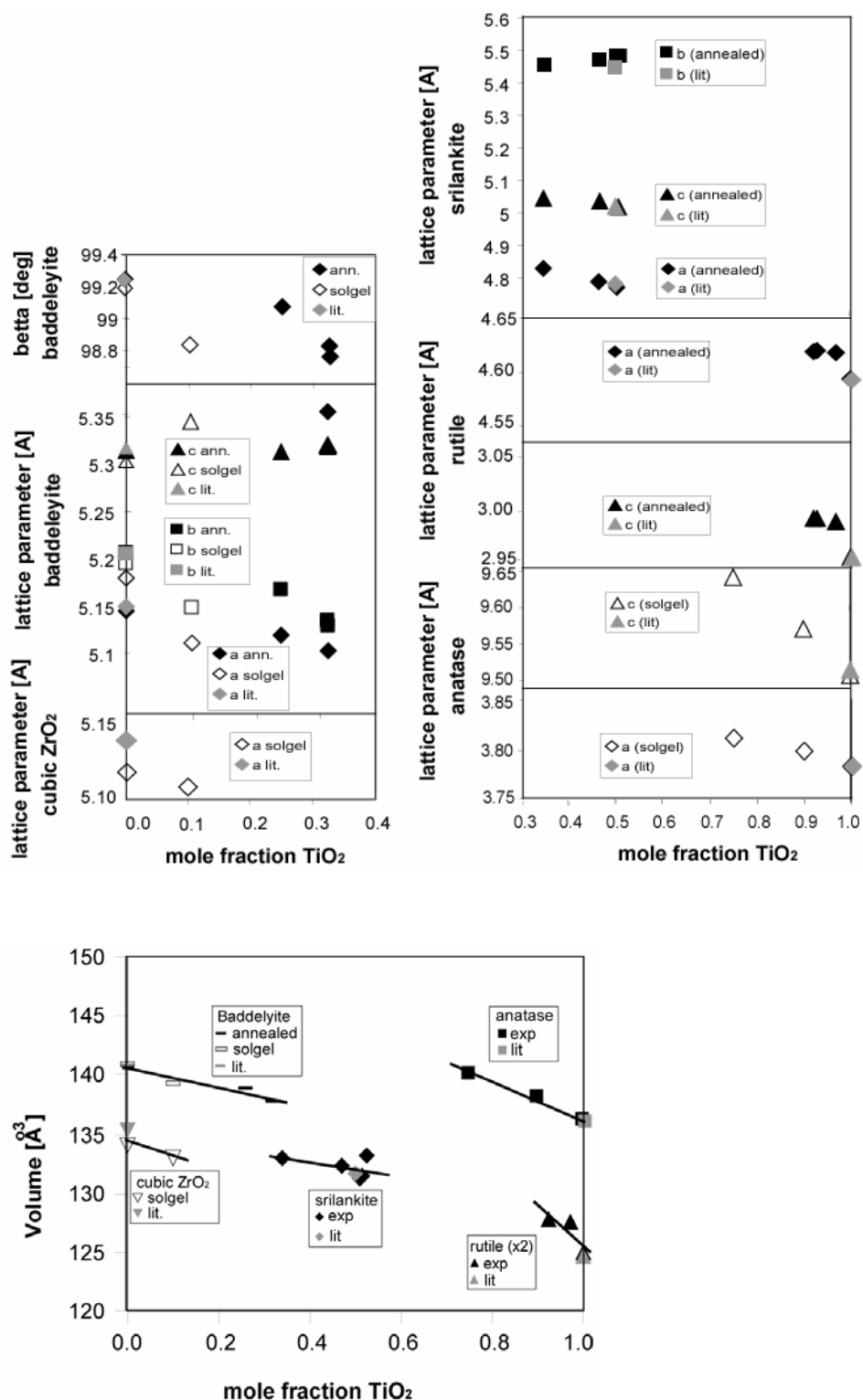


Figure 20: Lattice parameters and volumes of synthesized oxides as refined by full profile analysis. Values are given for experiments with nominal bulk compositions in mol% TiO_2 . Literature data are: Baddeleyite [199], cubic ZrO_2 [79], srilankite [200], rutile [201] and anatase [202]. Mole fractions are refined occupancies (annealed samples), nominal bulk compositions (single phase sol-gel products) or estimates from phase diagrams (multi phase sol-gel products), respectively. Lines are linear fits (see text).

Results of full profile refinements are presented in Figure 20, showing lattice parameters as a function of the composition. The refined lattice parameters of all end-members of solid solutions are in very good agreement with literature data. The volume of baddeleyite was refined to $140.88(16) \text{ \AA}^3$, *Yashima et al* [199] give a value of 140.76 \AA^3 . The volume of cubic ZrO_2 was refined to $134.09(14) \text{ \AA}^3$, *Wang et al.* [79] present 135.4 \AA^3 . It is remarkable that the high temperature phase (cubic zirconia) has a smaller volume than the low temperature phase (baddeleyite). The volume of rutile was refined to $62.43(1) \text{ \AA}^3$, *Gonschorek* [201] describes a value of 62.43 \AA^3 ; the volume of anatase was refined to $136.15(4) \text{ \AA}^3$, *Howard et al.* [202] found a value of 136.27 \AA^3 ; the volume of srilankite was refined to $132.2264(18) \text{ \AA}^3$, *Newnham* [200] gives a value of 131.73 \AA^3 . Following the same trend, the lattice parameters of all solid solutions decrease with the substitution of the bigger cation Zr by the smaller Ti (Figure 20). Especially anatase and rutile show a significant change in volume with the incorporation of Zr.

The results of the non-equilibrium synthesis differ from those expected by the equilibrium phase diagram of *McHale et al.* [70] (Figure 21). In the sol-gel synthesis, tetragonal zirconia was not synthesized but baddeleyite along with cubic zirconia. In the synthesis at 500°C and 400°C with bulk composition $x=0.10$, solid solutions with structure of baddeleyite and the cubic ZrO_2 were produced and thus, the amount of TiO_2 that can be incorporated into the structures is higher than described before.

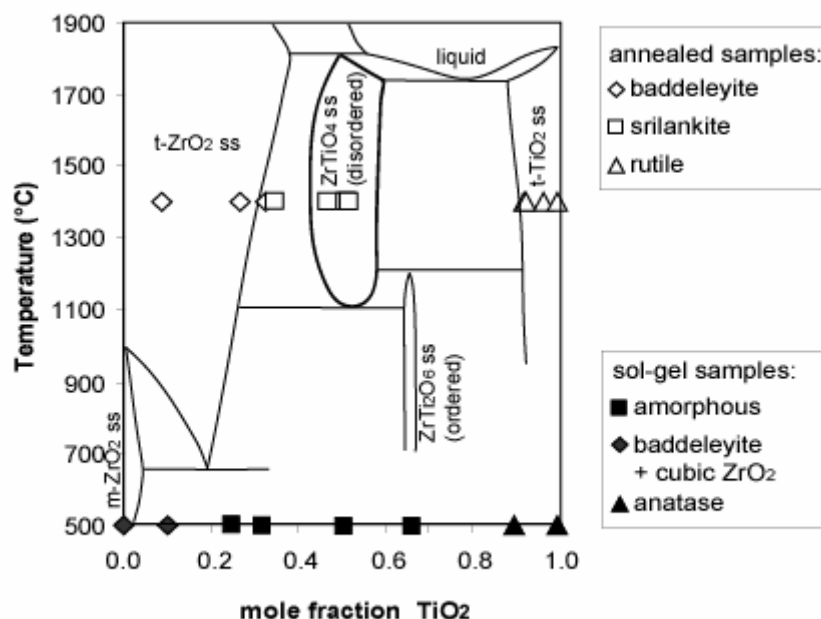


Figure 21: Phase diagram of the system TiO₂-ZrO₂. t-ZrO₂ ss indicates the solid solution with structure of tetragonal zirconia, m-ZrO₂ ss the solid solution with structure of baddeleyite, t-TiO₂ ss the solid solution with structure of rutile. Plotted are solid solutions from annealed samples (open symbols) and from samples of sol-gel synthesis (filled symbols) in the structures of anatase, rutile, baddeleyite, cubic ZrO₂, srilankite and an amorphous phase. Compositions are refined from full profile analysis (annealed samples) and nominal bulk compositions (sol-gel samples). Redrawn after *Mc Hale et al.* [70].

Furthermore, stable fits of Rietveld refinements on the annealed sample with $x=0.33$ were found in which the occupancies of both, baddeleyite and cubic zirconia, are refined to $x\sim 0.33$. These values again extend the metastability fields of the phases. It is therefore confirmed that the high temperature srilankite phase has disordered structure as full profile refinements do not show any superstructural reflexes. Furthermore $x=0.92$ was refined as lowest value for the annealed solid solutions with rutile structure, consistent with the phase diagram by *McHale et al.* [70].

As demonstrated above we were able to obtain homogeneous starting materials of Ti_xZr_{1-x}O₂ with $x=0.00, 0.10, 0.25, 0.33, 0.50, 0.67, 0.75, 0.90$ and 1.0. The synthesis path using a hydrous sol and hydrolysis temperature of 400°C was most appropriate and produced samples with carbon contents <0.5 wt% in the compositional range of $0.10 < x \leq 1.0$. Products of the synthesis with $x=0.90$ and 1.0 were nanoscale anatase and microscale rutile as the annealed counterpart, which were used for compression experiments in the DAC.

1.2. Synthesis of Microscale Anatase and Nanoscale Rutile $\text{Ti}_{0.9}\text{Zr}_{0.1}\text{O}_2$

Hydrothermal experiments as well as dry annealing experiments were performed, using nanoscale anatase $\text{Ti}_{0.9}\text{Zr}_{0.1}\text{O}_2$ as starting material which was synthesized by the sol-gel method. For hydrothermal experiments, the starting material was filled in a gold capsule, 5 wt% H_2O was added and the capsules were welded shut. For the synthesis of microscale anatase conditions below the estimated transformation temperature to rutile were chosen (pressure=1 kbar, temperature=500°C) and a duration of 5 days to allow for growth of the crystallites. The run product was a mixture of microscale rutile and microscale anatase, determined by XRD. In order to prevent the transformation into rutile, a second experiment at 300°C was performed. The experiment was successful and the run product was pure microscale Zr-doped anatase (Figure 22).

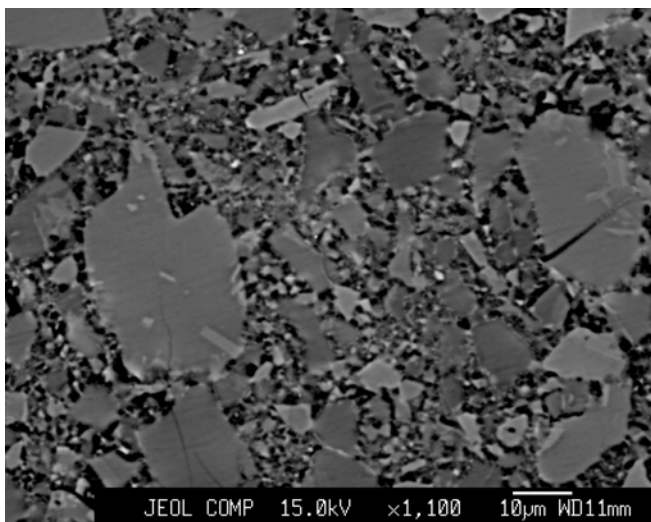


Figure 22: Back scattered electron image of microscale anatase $\text{Ti}_{0.9}\text{Zr}_{0.1}\text{O}_2$

For the synthesis of nanoscale rutile, conditions above the estimated transformation temperature (pressure=1 kbar, temperature=750°C) and a short run duration of one hour were chosen in order to suppress crystal coarsening. Nevertheless, the run product obtained was microscale rutile. Taking into account that the synthesis at 500°C also produced microscale rutile and anatase it is suggested that it is not possible

to find the conditions required for a successful synthesis of nanoscale rutile upon the hydrothermal route. This is because the coarsening of the material seems to happen before the transformation is complete. Therefore, dry annealing experiments were performed for the transformation to nanoscale rutile. The starting material was placed into platinum crucibles and heated in the furnace under air. The phase transformation was expected to take place at $\sim 500^{\circ}\text{C}$, but it was found that after heating at temperatures between 500°C and 1000°C for 1 hour only anatase was present. Therefore, heating time or temperature were decreased and it was found that heating at 800°C for 7 days as well as at 1200°C for 10 minutes led to the transformation into a mixture of microscale TiO_2 and rutile. It can be assumed that the transformation occurs in the form anatase $\rightarrow \text{TiO}_2$ \rightarrow rutile. During or even before the transformation the crystallites coarsen to the micrometer range, making it impossible to synthesize nanoscale rutile.

2. Experimental Results on the System $\text{TiO}_2\text{-ZrO}_2$ to 10 GPa

High pressure experiments were carried out in the piston cylinder apparatus at pressures of 2 GPa and 3.5 GPa and temperatures of 1300°C and 1600°C, as well as on the multi anvil apparatus at a pressure of 10 GPa and temperatures of 1200°C and 1350°C. As starting material, mixtures of TiO_2 (99,999%) and ZrO_2 (99,99%) with a TiO_2 content of 75 and 40 mol% were used. In order to get a homogeneous and fine grained mixture, the oxides were ground for 6 hrs, using an achate mortar and pestle and heated in a furnace at 1300°C for 24 hrs, then grinded again for 12 hrs.

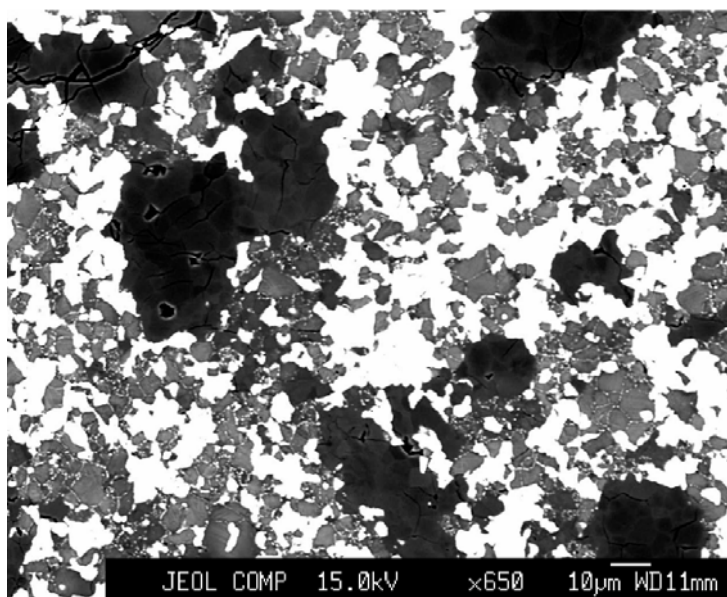


Figure 23: Back scattered electron image of the recovered sample from a piston cylinder experiment with 75 mol% TiO_2 , performed at $P=3.5$ GPa, $T=1220^\circ\text{C}$ and a duration of 21 hrs. The appearance is representative for other experiments. The light grains are Zr- rich solid solutions, the dark grains are Ti- rich solid solutions, grey grains have intermediate composition.

Microprobe analyses show that the run product is a sintered material that contains crystallites with the size of some micrometers. Figure 23 shows the back scattered electron image of a recovered sample from a piston cylinder experiment with $x=75$ mol% TiO_2 , which is representative for all run products of our series of

experiments. The grains have reaction rims, indicating that chemical equilibrium is not yet achieved.

The chemical compositions of the phases produced were analyzed, using the Wavelength Dispersive Spectrometry (WDS). Rutile and zirconia standards were used for calibration. Duration for the measurements were 20 seconds on the peak position and 10 seconds on the background. For each sample, 100 points were measured and it was assured that every measured point was placed well within a grain. The results were transformed to whole-numbered mol% TiO₂ and the amount of each mole-number was counted, Figure 24 shows the results for the samples synthesized at 2 GPa and 1650°C. A Ti rich solid solution with ≤ 12 mol% ZrO₂, an intermediate phase with 45-70 mol% TiO₂ and a Zr-rich phase with ≤ 28 mol% TiO₂ were found. It has to be noted here that chemical equilibrium is not claimed to be achieved. For that, multiple reversal experiments would have been necessary. Nevertheless, the experiments are sufficient to investigate the composition of solid solutions in the pressure- and temperature range analyzed and to determine the maximum amount of Zr-doping in TiO₂ polymorphs to ~10 mol%.

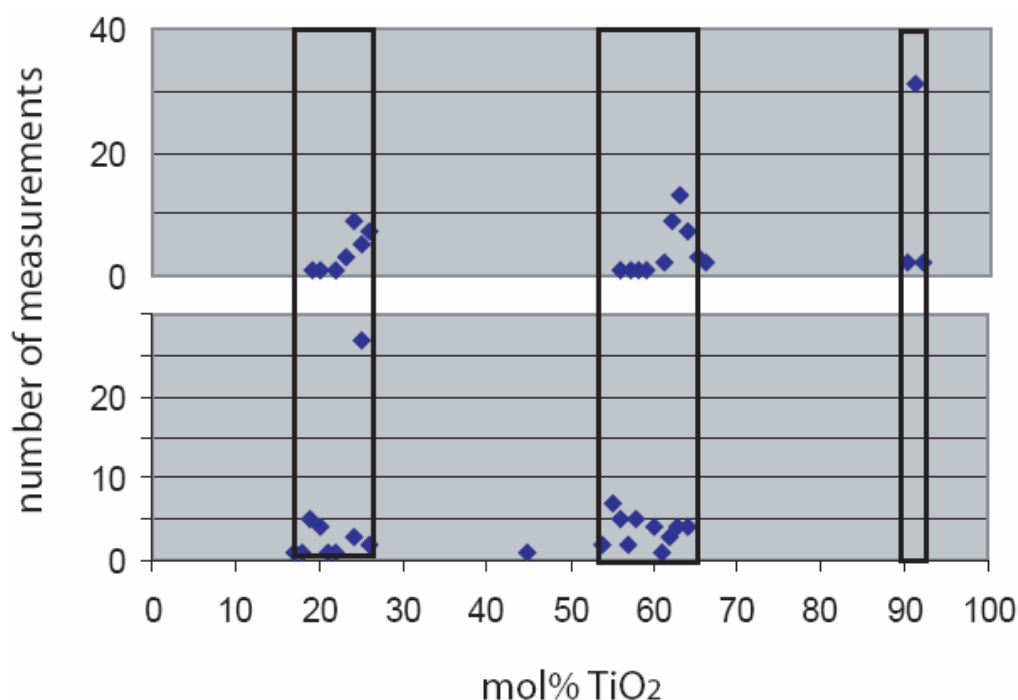


Figure 24: Chemical composition of quenched samples from piston cylinder experiments at 2 GPa and 1650°C. Starting materials had the composition of 75 (top) and 40 (bottom) mol% TiO₂. Datapoints are counts of whole-numbered values of mol% TiO₂.

Figure 25 shows the experimental results for the system $\text{TiO}_2\text{-ZrO}_2$ at pressures ≤ 10 GPa. Between 2 and 3.5 GPa, the Ti content of the Zr-rich phase (baddeleyite and high pressure polymorphs) and the intermediate phase (srilankite and high pressure polymorphs) increase with increasing pressure, as expected for the smaller cation in the high pressure phase. The phase boundary of the Ti-rich phase (rutile and high pressure polymorphs) does not shift with pressure, indicating that the Zr solubility in TiO_2 phases is limited to ~ 10 mol%.

XRD data show that disordered orthorhombic srilankite is stable up to at least 3.5 GPa and transforms to a high pressure polymorph between 3.5 and 6 GPa. Hydrothermal origin for srilankite can be ruled out and an igneous origin can be confirmed, consistent with the occurrence in high grade rocks such as eclogites, granulites, lamprophyres and chromatites. Furthermore, an upper pressure limit for the stability of srilankite of 6 GPa can be given.

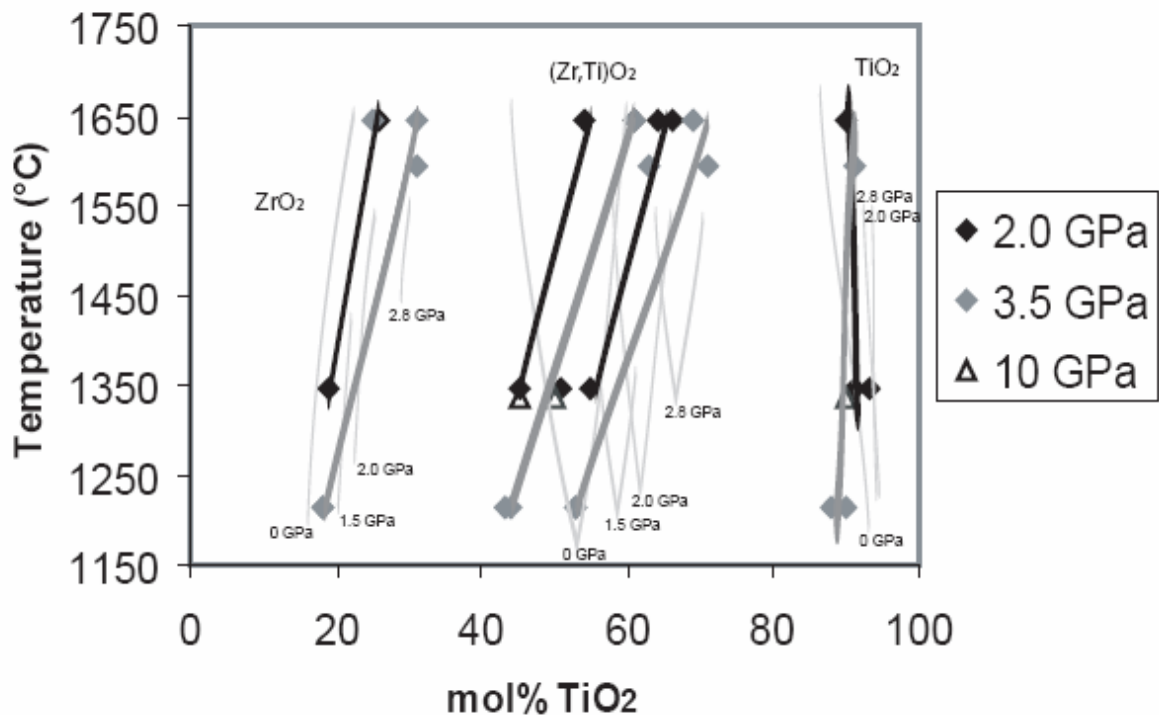


Figure 25: Experimental results of the system $\text{TiO}_2\text{-ZrO}_2$ at pressures ≤ 10 GPa. Thick lines label results of this study: Zr-rich phase is baddeleyite and high pressure polymorphs, the intermediate phase is srilankite and high pressure polymorphs, Ti-rich phase is rutile and high pressure polymorphs. Thin lines are after data from ref. [73].

3. Compression Behavior of Anatase and Rutile

A systematic experimental study was performed on pure TiO_2 and $\text{Ti}_{0.9}\text{Zr}_{0.1}\text{O}_2$ materials with micro- and nanometer scaled crystallite sizes. The compressibilities of the materials were determined by equation of state (EoS) fits. An overview over experimental studies is presented in Table 2. Only the compression behavior of microcrystalline TiO_2 anatase and rutile as well as of nanoscale TiO_2 anatase were studied sufficiently before (references are given in Table 2). In the following, new results on the compression behavior of TiO_2 nanoscale rutile and $\text{Ti}_{0.9}\text{Zr}_{0.1}\text{O}_2$ anatase (micro- and nanoscale) and rutile (microscale) are presented. Unfortunately, experiments on Zr-doped nanoscale rutile can not be presented here because the material could not be synthesized. It should be noted again that the maximum amount of ZrO_2 incorporated by the TiO_2 polymorphs up to 10 GPa is 10 mol% (compare Figure 25), leading to the composition of the Zr-doped material studied here.

Table 2: Overview over experiments

	Size	Material	Literature	Comp.-cycles
Anatase				
TiO_2	μm	chemical	Sufficiently studied (ref. [1])	
	nm	sol-gel	Sufficiently studied (ref. [3,4])	
$\text{Ti}_{0.9}\text{Zr}_{0.1}\text{O}_2$	μm	hydrothermal	This study	
	nm	sol-gel	This study (ref. [203])	This study
Rutile				
TiO_2	μm	sol-gel/comm.	Sufficiently studied (ref. [14,19,20])	
	nm	sol-gel	This study	
$\text{Ti}_{0.9}\text{Zr}_{0.1}\text{O}_2$	μm	sol-gel	This study	
	nm	n.a.		

Material = starting material (comm = commercial chemical, sol-gel = synthesized by the sol-gel process at the Fraunhofer ISC, hydrothermal = grown hydrothermally) Comp.-cycles = experiment with cycles of compression and decompression.

In the following, the compression behavior of the various forms of anatase and rutile is described (this section). It is followed by a section on the pressure induced phase transitions that were observed during the compression experiments and a section on computational ground states of TiO_2 phases.

3.1. Compression Behavior of Zr-doped Anatase

3.1.1 Experimental Details

An experiment was carried out on the hydrothermally grown microscale Zr-doped anatase $\text{Ti}_{0.90}\text{Zr}_{0.10}\text{O}_2$, mixed homogeneously with LiF (99.99% purity) in a mass proportion of about 1:1. *In-situ* XRD patterns were collected at APS, using an X-ray beam with $\lambda=0.33 \text{ \AA}$ and a size of $6 \times 15 \text{ \mu m}$. The sample-to-detector distance was 248 mm. The seats of the DAC had an opening of 22° , allowing the collection of diffraction data to $\sim 1 \text{ \AA}^3$. The standard deviation of the LiF volume at the maximum pressure achieved (13 GPa) is less than 0.01 \AA^3 , corresponding to an uncertainty in pressure of less than 0.5 GPa.

Another experiment was carried out on nanocrystalline Zr-doped anatase $\text{Ti}_{0.90}\text{Zr}_{0.10}\text{O}_2$, synthesized with the sol-gel process, again mixed with LiF (99.99% purity) in a proportion of about 1:1. The crystallite size of the doped anatase was about $12(\pm 3) \text{ nm}$, as indicated by High-Resolution Transmission Electron Microscopy (Figure 35) and confirmed by convolution-based profile fitting of XRD data. *In-situ* XRD patterns were collected at APS, using an X-ray beam with $\lambda=0.31 \text{ \AA}$ and a size of $6 \times 15 \text{ \mu m}$. The distance sample to detector was 272 mm.

3.1.2 Experimental and Computational Results

The lattice parameters of Zr-doped nanoscale anatase at zero pressure were refined to $a=3.8110(3) \text{ \AA}$, $c=9.6101(12) \text{ \AA}$ and $V=139.57(2) \text{ \AA}^3$, results from fitting to an EoS for the microcrystalline counterpart give smaller values of $a=3.799(1) \text{ \AA}$, $c=9.589(6) \text{ \AA}$ and $V = 138.5(1) \text{ \AA}^3$. Lattice expansion of TiO_2 nanoparticles was observed before [204,205]. As the larger Zr is incorporated for the smaller Ti into the structure, the values are consistently higher than the ones for pure anatase obtained by *Swamy et al.* [1,4] The authors report $a=3.7910(5) \text{ \AA}$, $c=9.5146(9) \text{ \AA}$ and $V=136.74(5) \text{ \AA}^3$ for macrocrystalline anatase [1] and $a=3.7830(3) \text{ \AA}$, $c=9.513(9) \text{ \AA}$ and $V=136.15(2) \text{ \AA}^3$ for nanocrystalline anatase with crystallite sizes of 30 to 40 nm [4].

The XRD data of the nanocrystalline sample at ambient conditions were used to estimate the crystallite size of the starting material. We used the TOPAS-ACADEMIC software [159] for convolution-based profile fitting [160] and refined the

microstructure. The diffraction spectrum of a CeO_2 standard was used to determine the source emission profile and instrumental contribution to peak broadening. The effects of crystallite size and strain on the peak broadening were analyzed using the double-Voigt approach, results are $L_{Vol_IB}=11.0(3)$ nm, and $e_0=22(1)\%$. The resulting value for the starting material is $D=14.7(4)$ nm, which is in good agreement with the estimate from TEM analysis of $12(3)$ nm.

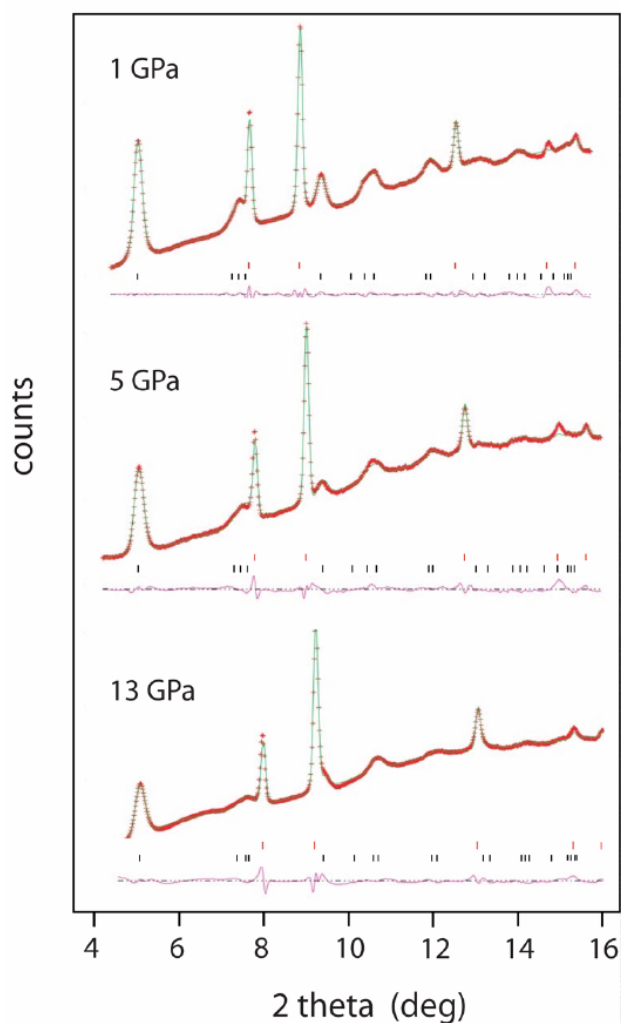


Figure 26: Results of full profile refinements of XRD patterns of nanoscale Zr-doped anatase at different pressures, obtained from DAC experiments, using radiation with $\lambda=0.31$ Å. Upper red tickmarks label LiF peaks, lower black tickmarks label peaks from anatase $\text{Zr}_{0.1}\text{Ti}_{0.9}\text{O}_2$.

The Zr-doped nano- and microanatase were observed as pure phases up to a pressure of 13 GPa, as indicated by the refined XRD patterns (Figure 26). The trends of the variations of the lattice parameters are presented in Figure 27. While all relative lattice parameters of microscale Zr-doped anatase decrease linearly upon compression,

the slope of the relative lattice parameter a/a_0 of the nanoscale material decreases for pressures >4 GPa, indicating a decrease in compressibility of the a parameter at higher pressures. Because the slope c/c_0 remains the same, the ratio of a/c strongly increases at pressures >4 GPa. For the nanoscale material, a difference in the slope is also observed for the average metal oxygen (M–O) bond lengths in the octahedra (Figure 28), indicating a change in the compression behavior at a pressure of ~ 4 GPa. The variation of the M–O4 bond length (between equatorial atoms) is slightly larger than the error of data points and therefore can be taken as almost constant. In contrast, the M–O2 bond length (in between apical atoms) has a negative slope at pressures <4 GPa and a positive slope at higher pressures. It is worth noting that the change in compression behavior is not related to a phase transformation, as can be seen from the refined X-ray pattern (Figure 26), which clearly indicates the presence of only anatase and LiF up to a pressure of 13 GPa.

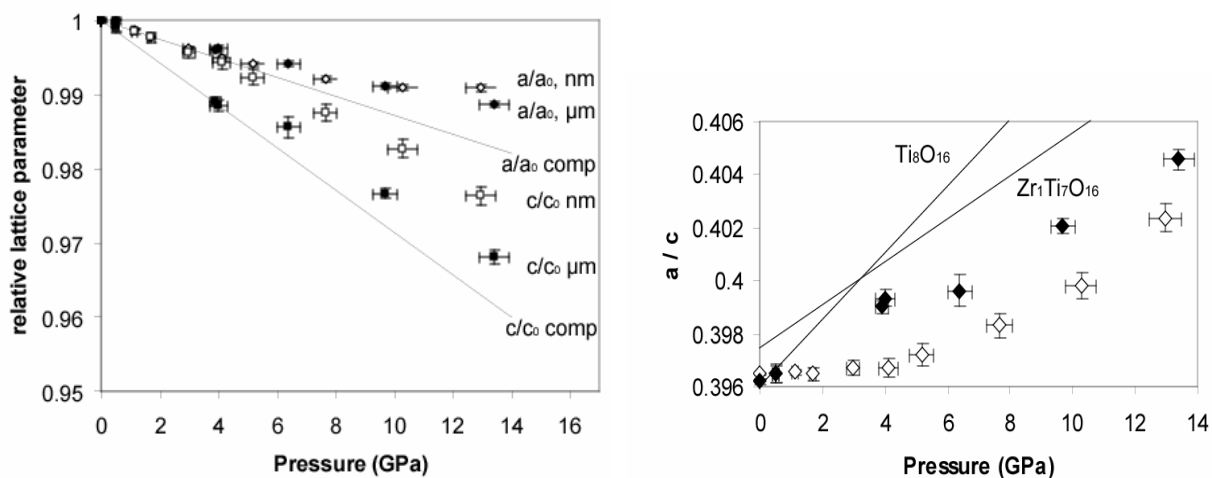


Figure 27: Relative lattice parameters as a function of pressure for Zr-doped anatase. The left figure shows a/a_0 and c/c_0 versus pressure, the right figure shows the ratio of the lattice parameters a/c versus pressure. Shown are data for nanoscale anatase $\text{Zr}_{0.1}\text{Ti}_{0.9}\text{O}_2$ (from experiments, open symbols), microscale anatase $\text{Zr}_{0.1}\text{Ti}_{0.9}\text{O}_2$ (from experiments, filled symbols) as well as anatase Ti_8O_{16} and $\text{Zr}_1\text{Ti}_7\text{O}_{16}$ (from computation, lines).

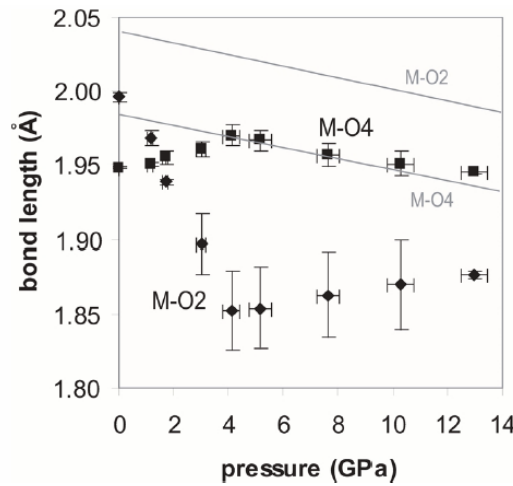


Figure 28: Metal-oxygen bond lengths of the MO_6 octahedra for nanoscale Zr-doped anatase. M-O2 indicates average bond length between metal atom (Ti, Zr) and apical oxygen atom (O2), M-O4 indicates average bond length between metal atom (Ti, Zr) and equatorial oxygen atom (O4); black points are experimental results from XRD; grey continued lines are results from *ab-initio* computations.

The pressure versus volume data obtained from full profile analysis were fitted to Birch-Murnaghan equations of state (EoS). For of the nanoscale Zr-doped anatase, V_0 was experimentally determined to $139.57(1) \text{ \AA}^3$ and the data were fitted to a third order EoS, resulting in $V_0=139.58(2) \text{ \AA}^3$, $K_0=227(18) \text{ GPa}$ and $K_0'=14(6)$ (Figure 29). The value of K_0' is 4 for most materials, a value of 14 is anormously high. Figure 29 shows a plot of Birch's normalized pressure F versus the Eulerian strain f , referred to as F-f plot, for the nanoscale material, using the experimentally determined V_0 . Fitting of the data resulted in $F = 3799f + 221$, it follows that $K_0=226(6) \text{ GPa}$. Given that the slope of the fit is $3K_0(K'-4)/2$, it follows that $K_0'=14$. These results are compatible with the results from the EoS fits presented above. For comparison with other materials, the data were fitted to a second order EoS with $K_0'=4$, results are shown in Figure 29. However, the quality of the fit is much poorer than for the fit with $K_0'=14(6)$.

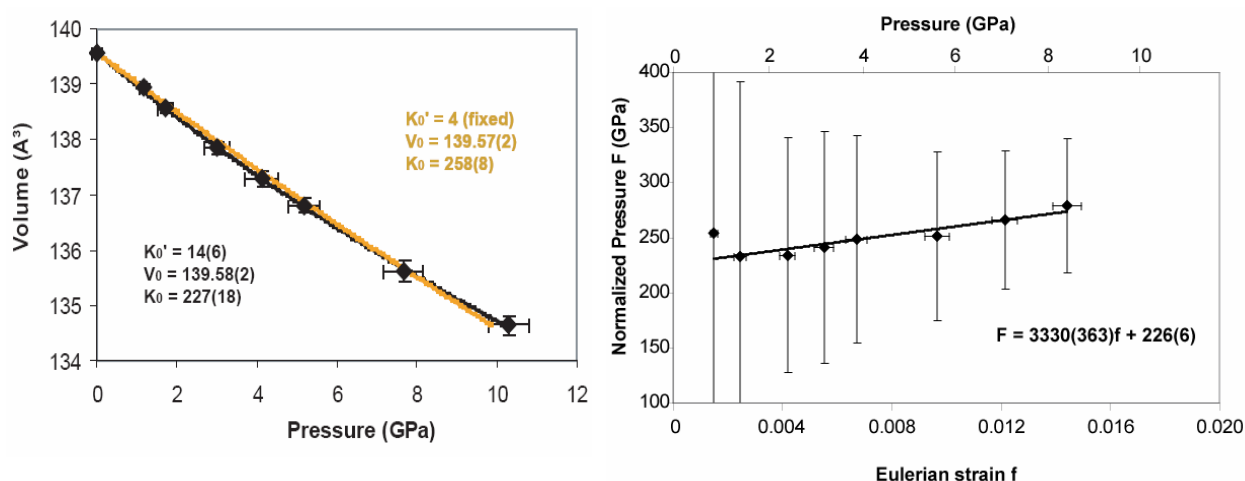


Figure 29: Compression behavior of nanoscale anatase $\text{Zr}_{0.1}\text{Ti}_{0.9}\text{O}_2$. The left figure shows experimental pressure-volume data from room temperature experiments (diamonds), a third order Birch-Murnaghan EoS fit (black curve) and a second order EoS fit with $K_0' = 4$. The right figure shows an F-f plot, data are described by a third-order truncation of the EoS and the linear fit has a slope of $3 K_0 (K' - 4)/2$, fitted to $F = 3799 f + 221$.

The F-f plot of microscale Zr-doped anatase (Figure 30) shows a horizontal slope with $K_0' = 4$, typical for most materials and different from the nanoscale counterpart, where $K_0' = 14$. Unfortunately, V_0 was not determined experimentally and therefore, the value of $V_0 = 138.39(51) \text{\AA}^3$ was used for fitting an EoS with $K_0' = 4$. Here, the bulk modulus was determined to $K_0 = 195(38) \text{ GPa}$ (Figure 30, left); fitting of the F-f plot (Figure 30, right) gave $K_0 = 241(8) \text{ GPa}$.

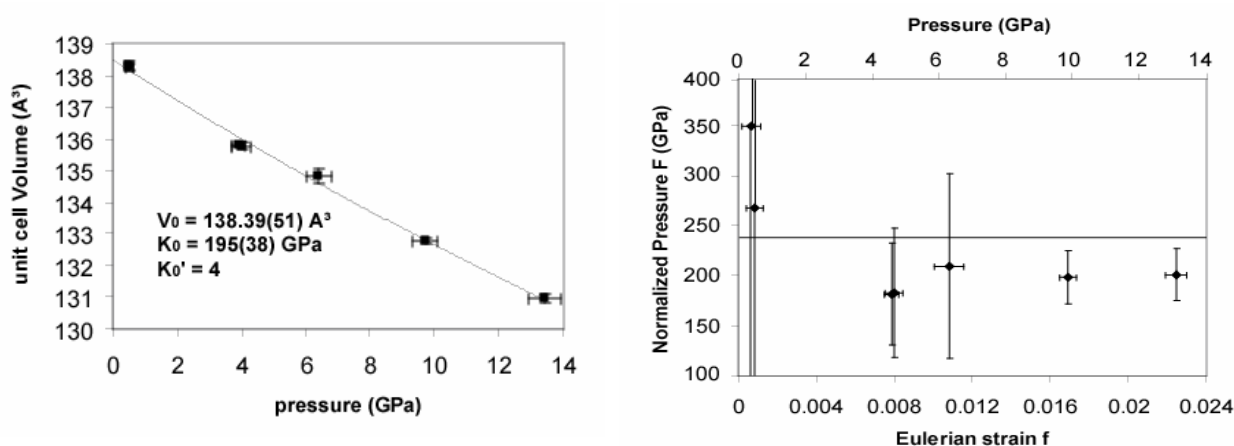


Figure 30: Compression behavior of microscale anatase $\text{Zr}_{0.1}\text{Ti}_{0.9}\text{O}_2$. The left figure shows experimental pressure-volume data from room temperature experiments (diamonds) and a second order Birch-Murnaghan EoS (black curve) with $K_0' = 4$. The right figure shows an F-f plot with a fitted slope of $F = 241(8)$.

Experiments were complemented by *ab-initio* computations on internal energies for different cell volumes of TiO₂ and Zr-doped anatase (Ti:Zr=7:1), for computational details see chapter II, section 3. The EoS parameters were obtained by fitting the E-V relation. In agreement with experiment it was found that doping of TiO₂ anatase with Zr expands the zero pressure volume by ~3% and decreases the compressibility markedly. We obtained $K_0'=4.0$ for both, TiO₂ and (Ti₇Zr)O₁₆, differing from experimental results for Zr-doped nanocrystalline anatase. Additionally, the computational results were compared to the experimentally determined relative lattice parameters (Figure 27) and bond lengths (Figure 28). The calculated slopes of relative lattice parameters a/a_0 and c/c_0 are constant and have a more negative slope than the experimental data. The bond lengths of the metal to the equatorial oxygen atoms of a polyhedron (M–O₄) are smaller than the ones to the apical atoms (M–O₂), in contrast to experimental data where the polyhedra are found largely incompressible.

In order to gain insight into the Zr-distribution in the TiO₂-ZrO₂ solid solution and to investigate the possible tendency of clustering of zirconium atoms, computations on alternative supercells were performed. Computations were conducted on cells with a volume of 11.0 Å³ per atom and the ratio of Ti:Zr=7:1. In the Ti-Zr supercell, the a parameter was doubled while b and c remained the same as in anatase, the notation is therefore $2a \times b \times c$. In this cell, next neighboring Zr atoms with a distance of 3.78 Å were found along the b direction. A different supercell with the setup $a \times b \times 2c$ had next neighboring Zr atoms with the same distance in both, a and b directions and therefore showed a tendency of clustering when compared to the $2a \times b \times c$ cell. In another supercell, the Zr atoms were spread equally, opposing the tendency of clustering. The setup was $2a \times 2b \times c$ and the next neighboring Zr atoms had a distance of 5.38 Å. The cell had a doubled size and two Zr atoms were placed in the positions 0, 0, 1/2 and 0, 1/2, 1/8. For all supercells, ions and cell shape were relaxed. Reciprocal space was sampled using k-point meshes of $6 \times 12 \times 4$ for $2a \times b \times c$, $12 \times 12 \times 2$ for $a \times b \times 2c$ and $4 \times 4 \times 4$ for $2a \times 2b \times c$.

The results are shown in Figure 31, indicating that the Zr atoms in anatase have a tendency to cluster. The cell with evenly spread Zr atoms ($2a \times 2b \times c$) with the longest possible Zr–Zr distance for nearest neighbors of 5.377 Å is energetically least favorable.

The cell $a \times b \times 2c$ in which the nearest neighbors with a Zr–Zr distance of 3.785 Å are found in the directions parallel to the a and b axis has the lowest energy.

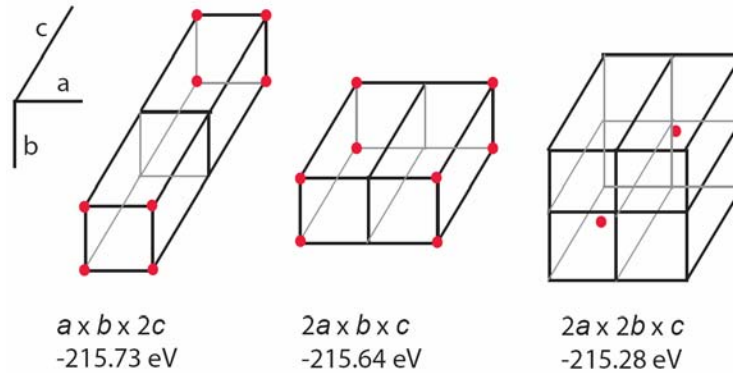


Figure 31: Energies of $\text{Ti}_7\text{ZrO}_{16}$ anatase supercells with different setups, indicated by the dimensions in a , b and c -direction and the position of the Zr-atom (red points). The supercell on the left exhibits the highest amount of Zr-clustering and has the lowest energy, thus is most stable.

3.1.3 Discussion

The bulk modulus of anatase strongly increases with a decreasing crystallite size to the nanometer scale as well as with doping of Zr. Values of the bulk modulus from fitting an EoS with $K_0' = 4$ for periodic cells from *ab-initio* computations are $K_0 = 153$ GPa for TiO_2 and $K_0 = 161$ GPa for $\text{ZrTi}_7\text{O}_{16}$. Values for microscale anatase are $K_0 = 178(1)$ GPa [1] and $K_0 = 179(2)$ GPa [2] (TiO_2) and $K_0 = 195(38)$ GPa ($\text{Ti}_{0.90}\text{Zr}_{0.10}\text{O}_2$). For nanoscale anatase, $K_0 = 237(3)$ GPa [3] and $K_0 = 243(3)$ GPa [4] are reported for TiO_2 and $K_0 = 258(8)$ GPa was measured in this study for $\text{Ti}_{0.90}\text{Zr}_{0.10}\text{O}_2$ (compare Figure 32 and Table 12).

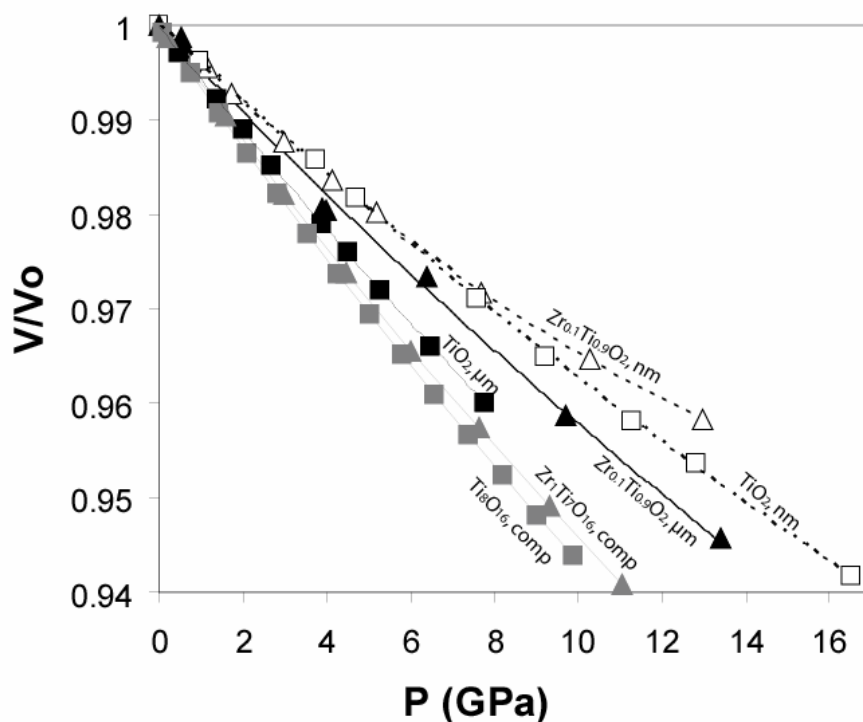


Figure 32: Compressibility of various forms of anatase. Grey symbols are computational results (“infinite crystal”), black symbols are from experiments on microscale crystallites. Open symbols indicate experimental results on nanoscale crystallites. Squares represent TiO_2 anatase, triangles show Zr-doped anatase. Lines are from fitting to an EoS.

The experimental results on Zr-doped nanoanatase show a significant change in compression behavior at pressures >4 GPa: The slope of a/c strongly increases and the slope of the bond length M-O_2 of the octahedral changes from negative to positive. This change in compression behavior can be understood by considering the crystal structure. Figure 33 shows the structure of anatase in the b - c plane. Each Ti is surrounded by an octahedron of six oxygen atoms. The octahedra are linked via edges and build a “zig-zag” chain parallel to a as well as b . The chains are stacked antiparallel to the c axis and, as the data suggest, can be compressed parallel to c with the same rate over the whole pressure range analyzed. However, along the directions a and b , the chains can be compressed more readily at pressures <4 GPa. This phenomenon also affects the bond lengths and thus the distortion of the octahedra: At pressures below 4 GPa the degree of distortion of individual octahedra increases, while above 4 GPa the distortion decreases.

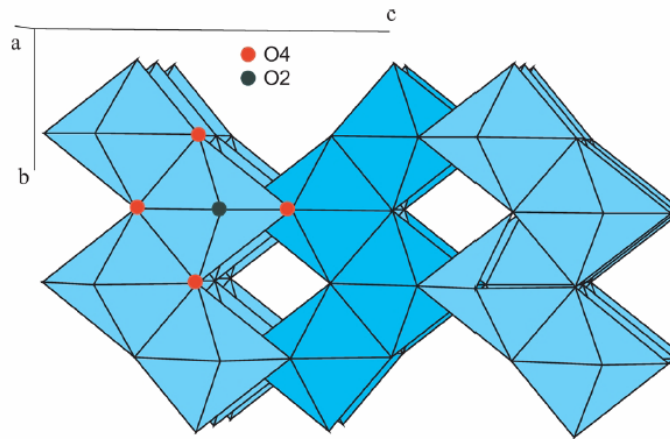


Figure 33: Structure of anatase. The lattice is shown in the b - c plane, dimensions are $3a \times 2b \times 2c$. O4 are marked red and display equatorial oxygen atoms (edge sharing), O2 are marked black and display apical oxygen atoms (cornersharing).

The change of compression behavior as it is seen for nanoscale Zr-doped anatase is not observed in experiments on the microscale material or computations (compare Figures 26 and 27). It is suggested that the anomalous compression behavior is attributed to the deviatoric stresses that play an important role in the compression of nanoscale material. Even though the pressure medium LiF was used, which is characterized by a small shear modulus [206], the spatial pressure distribution within the cell is most likely not even, resulting in deviatoric stresses. It can be concluded that the strong decrease of compressibility at higher pressures is related to the nanocrystallinity of the Zr-doped anatase material. It appears that Zr-doping and the tendency of clustering of Zr-atoms can affect the structural parameters and influence the elastic properties: opposed to the conclusion one would draw from comparison of elastic constants for TiO₂ and ZrO₂ polymorphs (Table 1), the incorporation of Zr into TiO₂ anatase results in an increasing bulk modulus.

3.1.4. Experiment with Cycles of Compression and Decompression

In order to find out, whether the anomalous compression behavior of Zr-doped nanoanatase is reversible upon compression and decompression, additional DAC experiments were performed with cycles of compression and decompression. As starting material, Zr-doped anatase Ti_{0.90}Zr_{0.10}O₂ was mixed with LiF (99.99% purity) in a mass proportion of about 1:1. XRD patterns were collected at APS beamline BM-D, X-ray beam with $\lambda=0.3344$ Å and a size of 6×15 μm. The sample-to-detector distance

was 201 mm. The seats of the DAC were made from cBN, allowing for collection of diffraction data to $d=1 \text{ \AA}$. Unlike other DAC samples, the sample was loaded without any compression applied during the loading process, then compressed at room temperature to 12 GPa, decompressed to 0.5 GPa, compressed to 12 GPa and decompressed to ambient conditions. A second DAC experiment was performed on Zr-doped nanoanatase, using Raman spectroscopy. The material was loaded together with a small ruby-sphere, serving as a pressure calibrant, no pressure medium was used. The pressure-induced frequency shifts were monitored while the sample was compressed and decompressed in the same way as for the previous experiment. After the experiment, the sample was prepared for TEM analysis, using a Focused Ion Beam Device [181]. The produced foil with a thickness of $\sim 50 \text{ nm}$ was analyzed at the TEM at the GeoForschungszentrum, Potsdam. The crystallite size of the doped anatase was measured before and after the experiment, using high-resolution TEM and convolution-based profile fitting of XRD data.

Table 3 presents refined lattice parameters of anatase and LiF as well as the pressure. Figure 34 shows the pressure-volume data of the sample as refined from XRD data and results of the fitting to a second order EoS with K' fixed to 4. The bulk modulus of the material was determined during the first compression to $K_0=211(7) \text{ GPa}$, upon the decompression K_0 decreased to $199(3) \text{ GPa}$ and it was increased upon the second compression to $249(9) \text{ GPa}$. The precompressed sample is stiffer than the uncompressed sample. The figure also shows the data of the previous experiment performed on the same material. It is worth noting at this point that the experiment was performed on a sample which was compacted and precompressed between diamond anvils during the sample loading. The bulk modulus was measured as $K_0=266(6) \text{ GPa}$, confirming the hypothesis that precompressed samples are stiffer than originally uncompressed samples.

Table 3: Experimental lattice parameters and pressures

Exp.	Anatase			LiF		
	a (Å)	c (Å)	V (Å ³)	a (Å)	V (Å ³)	p (GPa)
1	3.801(1)	9.583(4)	138.45(6)	4.031(1)	65.47(1)	0.3(1)
2	3.800(1)	9.583(4)	138.39(7)	4.030(1)	65.46(1)	0.3(1)
3	3.800(1)	9.583(5)	138.35(8)	4.030(1)	65.46(2)	0.3(1)
4	3.799(2)	9.577(1)	138.20(20)	4.003(1)	64.14(1)	1.9(1)
5	3.794(1)	9.544(6)	137.35(10)	3.988(1)	63.44(1)	2.8(2)
6	3.790(2)	9.528(11)	136.86(18)	3.964(1)	62.28(1)	4.0(3)
7	3.784(1)	9.493(8)	135.89(14)	3.946(1)	61.42(1)	5.7(3)
8	3.778(2)	9.465(11)	135.11(19)	3.924(1)	60.43(1)	7.3(4)
9	3.770(1)	9.411(6)	133.79(10)	3.904(1)	59.49(1)	8.9(4)
10	3.767(2)	9.393(9)	133.29(15)	3.887(1)	58.75(1)	10.3(5)
11	3.762(2)	9.368(14)	132.57(23)	3.873(1)	58.09(1)	11.6(5)
12	3.761(2)	9.339(9)	132.09(14)	3.872(1)	58.05(1)	11.7(5)
13	3.761(1)	9.343(7)	132.15(11)	3.880(1)	58.42(1)	10.9(5)
14	3.761(1)	9.347(6)	132.24(9)	3.885(1)	58.62(1)	10.6(5)
15	3.763(1)	9.347(7)	132.37(11)	3.893(1)	59.00(1)	9.8(4)
16	3.768(1)	9.393(8)	133.37(13)	3.917(1)	60.11(1)	7.8(4)
17	3.770(1)	9.397(8)	133.52(13)	3.919(1)	60.17(1)	7.7(4)
18	3.772(1)	9.410(6)	133.87(11)	3.926(1)	60.53(1)	7.1(4)
19	3.777(1)	9.447(7)	134.75(12)	3.946(4)	61.46(1)	5.6(3)
21	3.781(1)	9.473(7)	135.40(12)	3.960(5)	62.10(1)	4.6(3)
22	3.783(1)	9.490(6)	135.80(10)	3.9732(6)	62.72(2)	3.8(2)
23	3.800(1)	9.556(5)	137.96(8)	4.024(1)	65.17(2)	0.6(1)
24	3.798(1)	9.550(7)	137.73(12)	3.982(1)	63.13(1)	3.2(2)
25	3.793(1)	9.521(5)	136.95(8)	3.959(4)	62.06(1)	4.7(3)
26	3.787(8)	9.494(5)	136.14(8)	3.933(1)	60.83(2)	6.6(3)
27	3.780(1)	9.462(6)	135.18(10)	3.909(1)	59.72(2)	8.5(4)
28	3.771(1)	9.417(6)	133.88(9)	3.880(1)	58.40(2)	11.0(5)
29	3.803(1)	9.567(3)	138.36(6)	4.026(1)	65.25(1)	0.5(1)

Figure 34 presents the ratio of lattice parameters a/c as a function of the pressure. The slope of the curve is linear for the first compression and more or less also for the decompression. Upon the second compression however, the slope becomes steeper at pressure larger than 5 GPa (line 3), which is comparable to the previous experiment (line 3'). The anomalous compression behavior for nanoscale Zr-doped anatase reported before is therefore partly reproduced in this study.

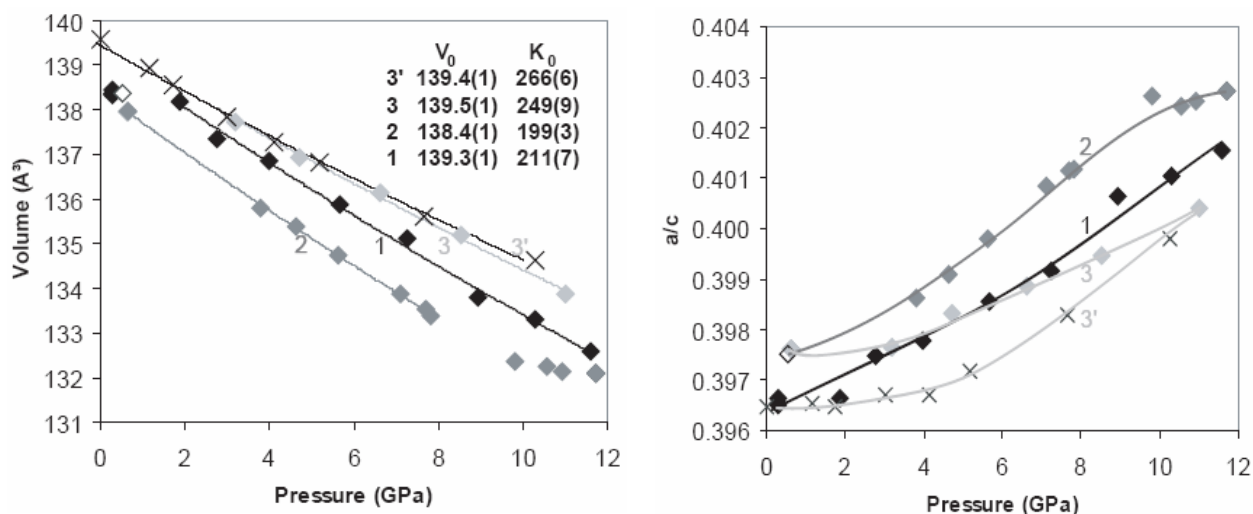


Figure 34: Results of a DAC experiment on nanocrystalline $Zr_{0.1}Ti_{0.9}O_2$ with cycles of compression and decompression. Experimental room temperature pressure-volume data are shown on the left side, curves are fits to a second order Birch-Murnaghan EoS with $K_0'=4$. The ratio of the lattice parameters a/c are presented on the right side, curves are to guide the eye. Data are from the experiment on an originally uncompressed sample (diamonds) and the experiment on a precompressed sample (crosses). The black symbols (labelled “1”) are from the first compression; the dark grey symbols (labelled “2”) are from the first decompression, the light grey symbols (labelled “3”) are from the second compression, the open symbol diamonds are from the second decompression and the light grey symbols labeled “3'” is from the experiment on precompressed material.

The XRD data of the sample at ambient conditions at the beginning (a) and at the end (b) of the experiment were used to estimate the crystallite size and to see whether a change of the microstructure can be observed. Results of convolution-based profile fitting revealed that the strain of the material increased strongly during the experiment from $e_0=0.13(3)\%$ at the beginning to $e_0=0.26(4)\%$ at the end. Another confirmation of the additionally induced strain is the relationship between a and c lattice parameters (Table 4). The unit cell at the end of the experiment is deformed with an elongation of the a parameter and shortening of the b parameter. At the same time, the unit cell volume and pressure are practically the same.

Table 4: Results of convolution-based profile fitting

	p (GPa)	V (\AA^3)	a (\AA)	c (\AA)	$L_{Vol, IB}$ (nm)	D (nm)	e_0 (%)	Rwp
a	0.29	138.30(4)	3.7998(4)	9.578(2)	8.2(4)	10.9(6)	0.13(3)	8.6
b	0.52	138.22(5)	3.8017(4)	9.563(3)	9.3(6)	12.4(1)	0.26(4)	9.1

at the beginning (a) and at the end (b) of the experiment;

Figure 35 shows high-resolution TEM images of the starting material as well as the quenched sample of the second experiment, performed on anatase $Ti_{0.90}Zr_{0.10}O_2$

without the use of a pressure medium. The crystallite sizes are $12(\pm 3)$ nm for both samples and therefore remain more or less constant during the experiment. The crystallites of the quenched sample show spherical crystal shape and are defect free.

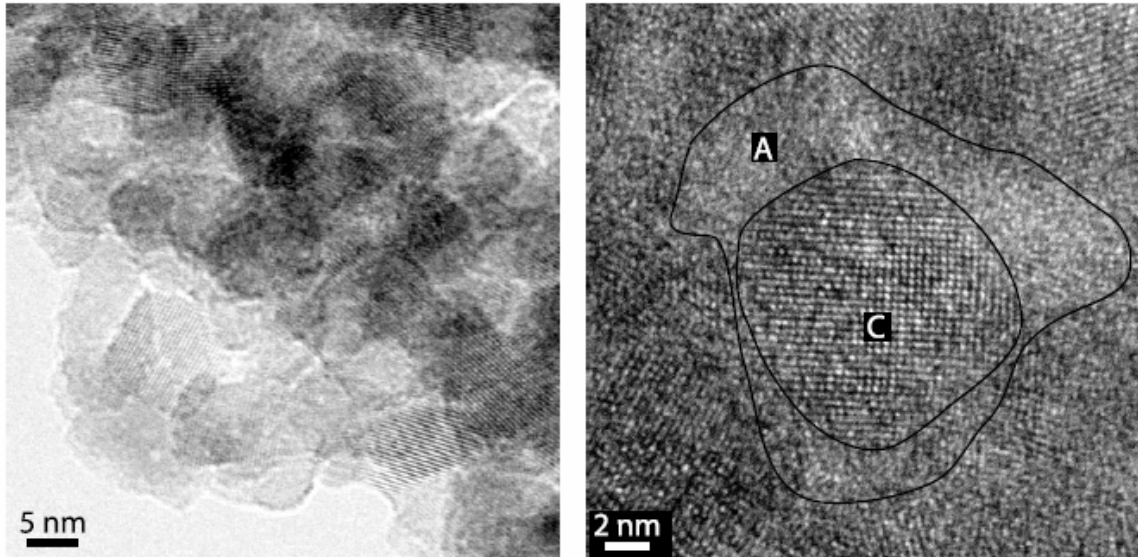


Figure 35: HRTEM images of the nanoscale anatase $\text{Ti}_{0.90}\text{Zr}_{0.10}\text{O}_2$ sample before (left) and recovered after the experiment (right). A indicates an area of a suggested amorphous rim, C indicates a crystalline area.

There are several lines of evidence suggesting that the crystallites are surrounded by amorphous rims and that amorphization takes place gradually upon compression. Pressure induced amorphization was observed before by *Swamy et al.* [207], who claimed that anatase with crystallite size of <10 nm transforms upon compression to a high density amorphous phase, which transforms to a low density amorphous phase upon the quenching process. In contrast, coarser samples undergo transformations to crystalline high pressure polymorphs. Partial amorphization was suggested earlier for experimental studies (e.g. [3]), but could not be detected by the *in-situ* XRD analysis because the broad amorphous features would be hidden in the background signal – a phenomenon that applies also for this study. Partial amorphization was theoretically predicted by *Pischedda et al.* [3], who performed molecular dynamics computations, using a simple Buckingham potential, and computed compression of a single anatase nanoparticle in a box of 10 nm dimension in excess of the nanoparticle volume. At 25 GPa, the simulations suggest the appearance of disorder in the surface-shell region (about 30-40% of the atoms), surrounding a more rigid

crystalline core, which also contains some defects. In our study, the TEM analysis of the material after compression shows in fact features that can be assigned as rims of amorphous material with a thickness of several nanometer (Figure 35, right), confirming the suggested appearance of partial amorphization. However, the TEM image shows a foil of the sample in which several crystallites overlap and the features seen could be the consequence of that. To avoid overlap of crystallites, TEM foils with a thickness of 10-15 nm would be necessary.

The lines of evidence described lead to the conclusion that the nanoscale anatase $\text{Ti}_{0.9}\text{Zr}_{0.1}\text{O}_2$ undergoes partial pressure induced amorphization, which leads to stiffening of the material. Upon compression, amorphous rims start to envelop the crystallites. The amorphization takes place gradually and starts at lower pressures than predicted theoretically (12 GPa as opposed to 25 GPa [3]). We can use the phenomenon of amorphization to explain the compression behavior of the sample in the following way: Part of the compression energy is used for the formation of amorphous crystallite rims. The rims seem to shield the anatase particles against pressure change and most probably deform and exhibit strain while they are assimilating the compression energy. The anatase nanocrystallites therefore undergo less pressure change than the LiF particles. The partial amorphization is accompanied by stiffening of the material, making it an interesting phenomenon for material research with the goal to create new abrasive materials.

3.1.5. Conclusions

Experimental and computational results show that anatase becomes less compressible when the crystallite size is decreased to the nanometer scale and when the material is Zr-doped (compare Figure 32 and Table 11). The fact that Zr-doped nanoanatase is least compressible is opposite to the expectation from the comparison of elastic constants for TiO_2 and ZrO_2 polymorphs: while ZrO_2 polymorphs show a smaller bulk modulus than the corresponding TiO_2 forms, the incorporation of Zr into TiO_2 anatase results in an increasing bulk modulus.

For the Zr-doped nanoanatase, XRD analysis showed a significant change in compression behavior at pressures >4 GPa: The slope of a/c strongly increases (Figure 27), the slope of the bond length M-O2 of the octahedra changes from negative to

positive (Figure 28). Computations on supercells with different distances of neighboring Zr-atoms showed that Zr atoms at close distances are energetically favored, hinting at possible cluster formation of Zr in the (Ti,Zr)O₂ compounds (Figure 31). The change in compression behavior at ~4 GPa observed in the experiments is not reproduced by the computations for the perfect bulk crystal, suggesting that the anomalous compression behavior is caused by the nano-crystallinity of the samples. The cluster formation and resulting structural distortions can further augment the change in compression behavior.

It was furthermore observed that Zr-doped nanoanatase becomes stiffer upon multiple compression cycles. The first compression of the sample showed a bulk modulus of 211 GPa, after the sample was decompressed, the bulk modulus for the second compression was 249 GPa. We suggest that partial pressure induced amorphization plays an important role for the process of stiffening observed.

3.2. Compression Behavior of TiO₂ Nanoscale Rutile

Compression experiments at ambient temperature on nanoscale rutile were performed before by *Olsen et al.* [20]. In that study, the starting material was obtained via milling of bulk material to a final crystallite size of ~10 nm. Upon compression, the material transformed to the MI structure at ~20 GPa and the pressure-volume data resulted in a value of $K_0=211(7)$ GPa, identical for bulk rutile, and $K'=8(1)$. Milling can induce strain and structural disorder and therefore eventually affect the compression behavior of the material. To avoid this possibility, we used nanoscale rutile for the experiments which was synthesized from TiCl₄ starting material by a hydrothermal method, described by *Li et al.* [208]. The material was synthesized by the group of Prof. Guangshe Li, Fujian Institute of Research of the Structure of Matter, China and before at Brigham Young University, USA.

The DAC compression experiment was performed at APS under conditions as described for Zr-doped nanoanatase. The starting material with crystallite size of ~15 nm (Figure 46 left) was placed in the DAC along with Cu as pressure calibrant, no other pressure medium was used.

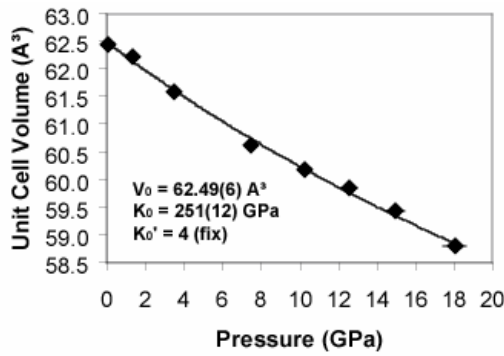


Figure 36: Pressure-volume data (diamonds) and a Birch-Murnaghan EoS fit (curve) of TiO₂ nanorutile from room temperature DAC experiments.

The pressure-volume data of nanorutile were used to determine the parameters of the EoS. V_0 was not available from experiments and therefore fitted in a second order EoS with $K'=4$, results of the fit were $V_0=62.49(6)$ Å³ and $K_0=251(12)$ GPa (Figure 36). The F - f plot of the data revealed that $K_0'=4$ and $K_0=257(22)$ GPa (Figure 37), consistent with the EoS fit mentioned before. The bulk modulus is similar to that of bulk rutile (230 GPa, compare Table 5).

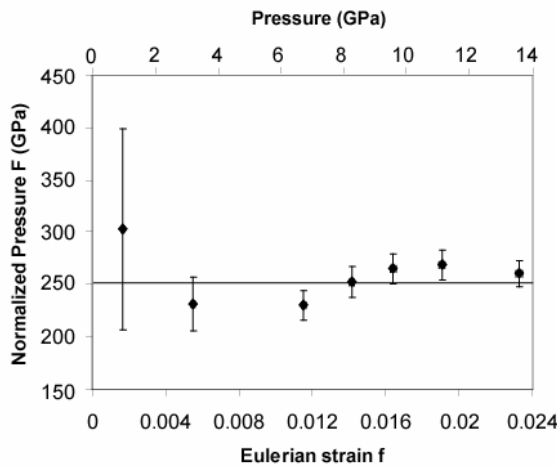


Figure 37: F - f plot of experimental data on TiO₂ nanorutile, based on the Birch-Murnaghan EoS. The data are described by a third-order truncation of the EoS and the linear fit has a slope of $3 K_0 (K' - 4)/2$.

Nanorutile shows the same compression behavior as the microscale counterpart in the pressure regime below 10 GPa. At higher pressures the data show slight stiffening in relation to the trend of microscale material. Furthermore, the bulk modulus obtained for hydrothermally grown material (this study) is essentially the same as for milled

starting material (Figure 38, compare ref. [20]). However, the latter one has a larger unit cell volume of 62.9 \AA^3 , compared to 62.5 \AA^3 for hydrothermally grown and bulk rutile.

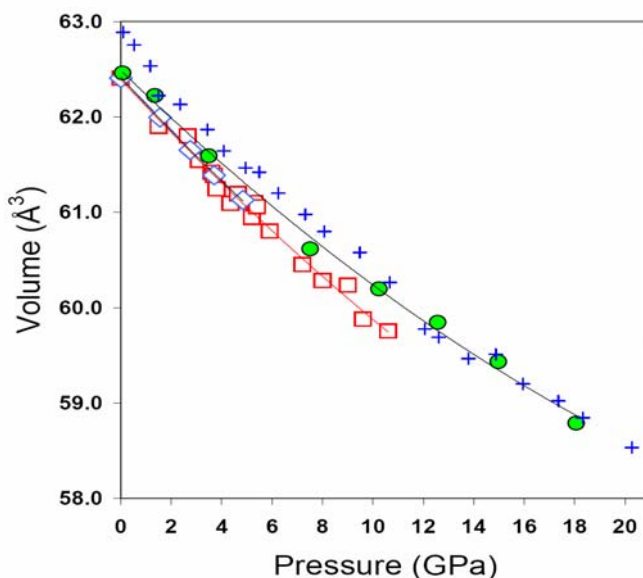


Figure 38: Pressure-volume data for bulk and nanocrystalline rutile. The diamonds [209] and squares [210] represent bulk rutile while the crosses represent ~ 10 nm rutile nanocrystals from milled starting material [20], and circles represent ~ 15 nm rutile nanocrystals from hydrothermal growth (this study).

3.3. Compression behavior of Zr-doped microscale rutile

DAC experiments were carried out analogous to experiments on Zr-doped nanoanatase. For the study on Zr-doped rutile, $\text{Ti}_{0.9}\text{Zr}_{0.1}\text{O}_2$ from sol gel synthesis was annealed at 1400°C for 20 hours, transforming to microscale rutile. The rutile obtained was mixed with LiF in mass proportions of 1:1 and the mixture was homogenized. The lattice parameters of Zr-doped rutile at zero pressure were refined to $a=4.622(1) \text{ \AA}$, $c=2.993(2) \text{ \AA}$ and $V = 63.944(5) \text{ \AA}^3$. Incorporating the larger Zr as substituent for the smaller Ti into the structure, the values are consistently higher than the ones for pure rutile with $a=4.5939(1) \text{ \AA}$, $c=2.9589(1) \text{ \AA}$ and $V=62.444(2) \text{ \AA}^3$ (NIST-certificated values).

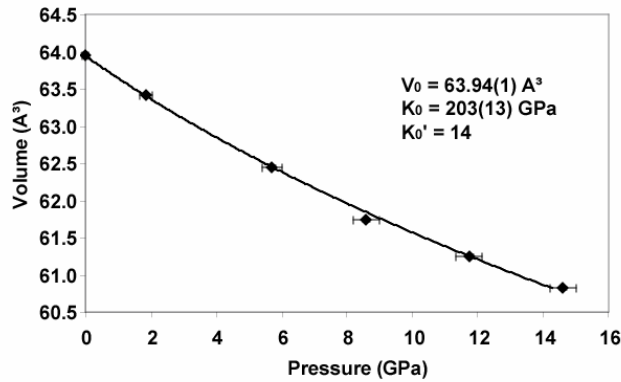


Figure 39: Pressure-volume data for microscale rutile (diamonds) with composition $\text{Ti}_{0.9}\text{Zr}_{0.1}\text{O}_2$ and Birch-Murnaghan equation of state fit (curve).

Least-square refinement of the data to a third order Birch Murnaghan EoS resulted in the following parameters: $V_0=63.94(1) \text{ \AA}^3$, $K_0=203(13) \text{ GPa}$ and $K_0'=14(4)$ (Figure 39). The value for K_0' of 14 is higher than for most materials and similar to the refined value of the nanoscale Zr-doped anatase (Figure 29). Figure 40 shows an F-f plot for Zr-doped rutile, for which the experimentally determined V_0 was used. Fitting of the data resulted in $F = 2999(948)f + 206(12)$, it follows that $K_0=206(12) \text{ GPa}$ and the high value of $K_0' = 14$ is confirmed.

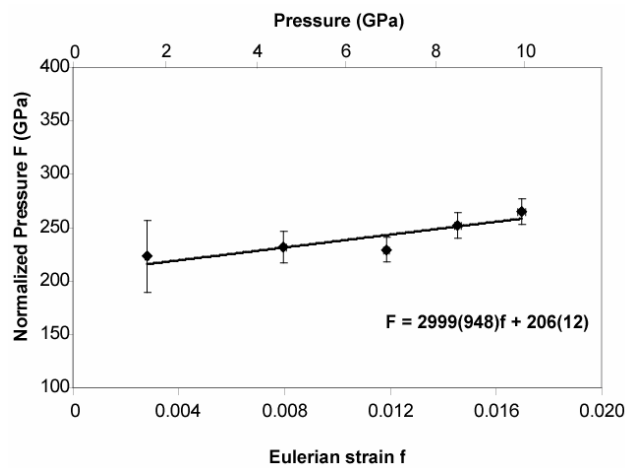


Figure 40: F-f plot of experimental data on $\text{Zr}_{0.1}\text{Ti}_{0.9}\text{O}_2$ microscale rutile, based on the Birch-Murnaghan equation of state. The data are described by a third-order truncation of the equation of state and the linear fit has a slope of $3K_0(K_0'-4)/2$.

Figure 41 shows the evolution of the relative lattice parameters a/a_0 and c/c_0 upon compression. The c -parameter has a constant slope over the pressure range

analyzed; the a -parameter shows a steeper slope at pressures <8 GPa than at higher pressures. This behavior is similar to the one described for Zr-doped nanoanatase.

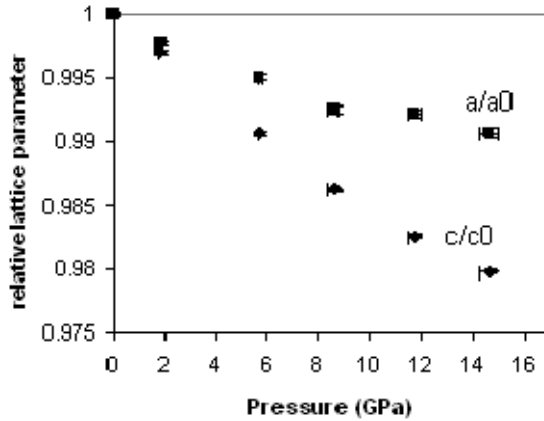


Figure 41: Relative lattice parameters a/a_0 and c/c_0 of $Zr_{0.1}Ti_{0.9}O_2$ rutile as a function of pressure from DAC experiments at room temperature.

Our data suggest that neither the incorporation of Zr nor the decrease of crystallite size to the nanometer range does modify the bulk modulus, differences of the values lie within the error of the fits (see Table 5). These results are different from those of anatase, where a decrease of crystallite size and doping with Zr leads to an increase of the bulk modulus.

Table 5: Volumes and bulk moduli of various forms of rutile

phase	V_0 (\AA^3)	K_0 (GPa)	K'_0	P (GPa)	Technique	Reference
TiO ₂ , bulk	62.5	230(20)	6.6(7)	0-20	DAC + XRD	[14]
TiO ₂ , bulk	62.5	210(10)	6.6(7)	0-8	MA + XRD	[19]
TiO ₂ , nano	62.49(6)	251(12)	4	0-18	DAC + XRD	this study
Ti _{0.9} Zr _{0.1} O ₂ , bulk	63.94(1)	203(13)	14	0-14	DAC + XRD	this study

K_0 = isothermal bulk modulus; V_0 = zero pressure Volume; * = fixed value; DAC = diamond anvil cell; XRD = *in-situ* X-ray diffraction; MA = multianvil

4. Pressure Induced Transformations of Anatase and Rutile

In the following, experimental results on the pressure induced phase transformations of anatase and rutile are reported. In the first section, a study on the phase boundaries anatase – TiO₂II and rutile – TiO₂II by means of sample synthesis with the multi anvil apparatus and XRD sample characterization is presented. Sections 4.2. and 4.3. address compression experiments in the DAC with *in-situ* phase characterization via XRD.

4.1. Multi Anvil Experiments on Phase Transition of Anatase and Rutile to TiO₂II

TiO₂II was found as accessory mineral in impact rocks (e.g.[13]) and raised the interest to determine the phase boundary between rutile and TiO₂II so that the pressure and temperature experienced by the rock could be constrained.

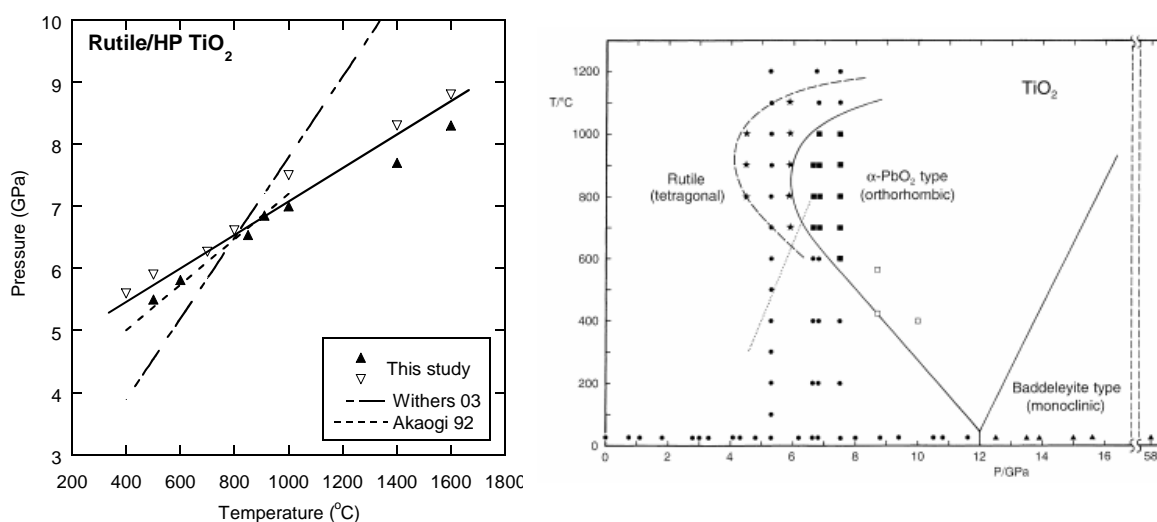


Figure 42: Phase diagram of the boundaries of rutile and TiO₂II. The left diagram (from Frost and Massonne, unpublished) shows phase boundaries of rutile (filled symbols) and TiO₂II (open symbols) bracketed by piston cylinder (<1000°C) and multi-anvil (>1000°C) experiments. Only the experiments that constrain the curve are shown. Curves from two previous studies are shown for comparison. The right figure is from ref. [19] and shows the phase diagram of TiO₂, obtained in heating and compression. Circles denote rutile; squares denote TiO₂II; triangles show MI. The full line marks the rutile/TiO₂II phase boundary for the bulk material, the broken line for the nanophase material, the dotted line is the phase boundary from ref. [56].

Experimental studies using the piston cylinder and multi anvil techniques were done by *Withers et al.* [24], *Akaogi et al.* [56], *Olsen et al.* [19] and also *Frost and Massonne* (personal information from D.J. Frost). The determinations of the phase boundary disagree considerably as shown in Figure 42, and changes from negative to positive slopes with increasing temperature are reported; for nanophase material, the phase boundary is shifted towards lower pressure [19]. The discrepancy between the studies demonstrates the complexity under which the conditions of the phase transformation are controlled. We therefore studied which parameters affect the conditions and mechanism of the transformation and conducted experiments on rutile and anatase starting material with different crystallites sizes under varying run conditions, using the multi anvil apparatus. Experimental conditions and starting materials are listed in Table 6, run pressure was 10 GPa for all experiments.

Table 6: Run conditions of multi anvil experiments

T (°C)	Start. mat.	#	time	rutile		TiO ₂ II			
				e_0	D (nm)	e_0	D (nm)		
1800	rutile (μm)	1	45min	min.	0.17(1)	>1000	maj.	0.010(1)	204(5)
1100	rutile (μm)	13	20sec	min	n.d.	n.d.	maj.	0.115(8)	41(3)
1100	rutile (μm)	2	45min	min	0.48(6)	84(9)	maj.	0.061(2)	105(5)
1100	rutile (μm)	3	22hrs	min	0.19(6)	>1000	maj.	0.044(1)	192(15)
1100	rutile (nm, hyd.)	16	45min	-	n.d.	n.d.	maj.	0.068(3)	75(3)
1100	rutile (nm, com.)	19	45min	min	n.d.	n.d.	maj.	0.054(6)	95(14)
1100	anatase (μm)	14	45min	-	n.d.	n.d.	maj.	0.041(2)	122(6)
1100	anatase (nm, sol.)	10	45min	-	n.d.	n.d.	maj.	0	34(1)
1100	anatase (nm, hyd.)	15	45min	-	n.d.	n.d.	maj.	0	42(1)
20	rutile (μm)	5	45min	maj.	0.27(5)	67(9)	-		

hyd. = hydrothermally grown; sol. = material from sol-gel synthesis; com. = commercial; min = minor phase (~5 wt%), maj. = major phase.

XRD analysis of the samples were performed at ESRF, Figure 43 shows representative patterns for the range of 2 theta of 6.5–18°. The peaks for the rutile starting material (green) are very sharp, whereas peaks of the cold compressed sample (blue) are much broader. Here, results from convolution based profile fitting indicate high strain with $e_0=0.27(5)$ and a small apparent crystallite size of 67(9) nm (Table 6, #5). Under compression at 1100°C, TiO₂II starts to form (red), but even though the run conditions lay within the proposed stability field of TiO₂II (Figure 42), ~5 wt% rutile is still present. Rutile in this sample has a much higher strain of $e_0=0.048(6)$ compared to

TiO₂II, where $e_0=0.061(2)$. The apparent crystallite size of rutile is smaller (84(9) nm) compared to TiO₂II (105(5) nm). Figure 44 shows a HRTEM image of the sample. TiO₂II phase makes up the bulk material and small lamella of rutile are intergrown. This appearance was observed before in natural minerals [211] as well as synthetic samples [67]. Longer run duration of 22 hrs leads to crystal growth of rutile to $D>1000$ nm and reduced strain with $e_0=0.19(6)$ (Table 6, #3), while extremely shortened duration of 22 sec produces a small amount of rutile for which the convolution-based profile fitting fails. Compression at higher temperature of 1800°C produces a sample similar to the one at 1100°C (compare #1 and #2 in table 6). In experiments with nanoscale rutile starting material, a very small amount of rutile is present in the experiment using ball milled commercial rutile, and no rutile is present when the nanoscale starting material was grown hydrothermally. XRD patterns of samples from experiments on anatase starting material do not allow to judge whether anatase is present as minor phase or not, because the peaks of anatase and TiO₂II strongly overlap.

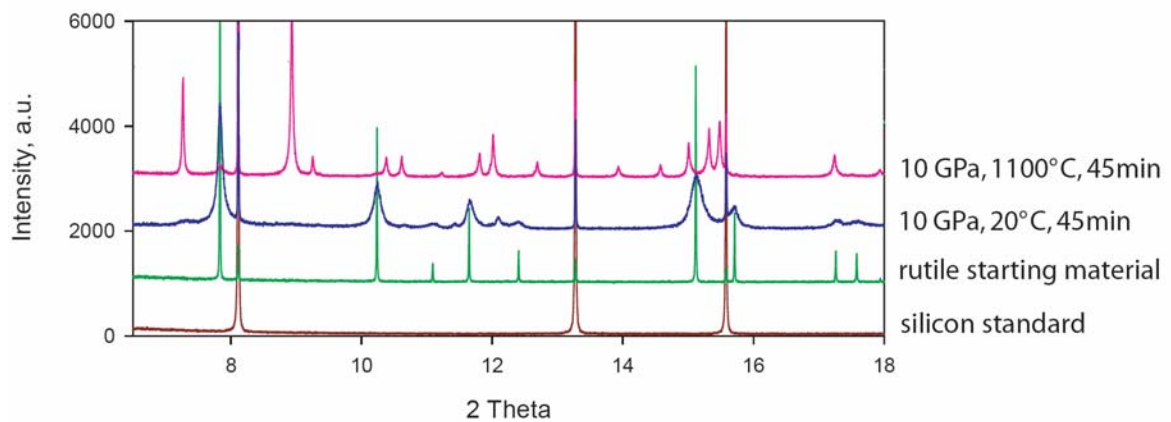


Figure 43: XRD patterns of the starting material and the recovered samples of multi anvil experiments in the range of 6.5-18°, collected at ESRF with radiation of $\lambda=0.711$ Å. The spectra show varying peak breadths and for broad peaks, strain or a decreased crystallite size is suggested. Results of convolution-based profile fitting are presented in table 6.

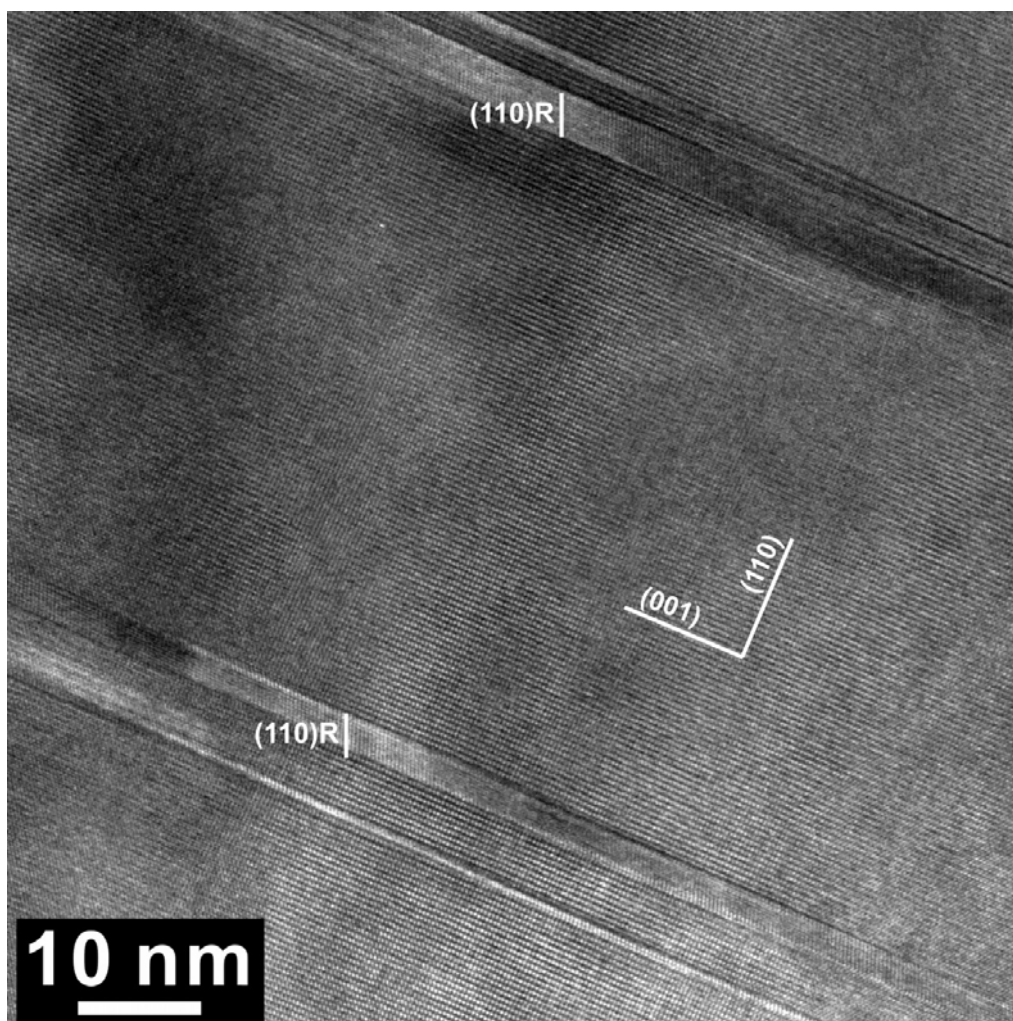


Figure 44: HRTEM image of the recovered sample of an experiment at 1100°C with duration of 45 min, using microscale rutile as starting material. The experiment was performed in the suggested stability field of TiO_2II , which is the main phase observed by X-ray diffraction. However, the sample contains lamella of rutile. Similar observations using HRTEM are described in refs. [67,211].

Even though experiments were performed in the proposed stability field of TiO_2II , ~5% of rutile remain present in recovered samples of multi anvil experiments at 10 GPa and 1100-1800°C. Small rutile lamella with breadths of a few nm and elongation parallel to the c -direction are found.

In multi anvil experiments, the volume is not constant as the transformation takes place and therefore, pressure can drop and may become buffered at the transition pressure where both phases coexist. In order to overcome this phenomenon, *in-situ* experiments are necessary, in which the pressure- and temperature conditions can be controlled more sufficiently. Pressure buffering does not occur in a natural environment

und therefore, TiO_2 can still be seen as an appropriate system to be used as Geothermobarometer to constrain pressure and temperature experienced by the rock.

4.2. DAC Experiments on Phase Transitions of Zr-doped Anatase

Experiments on anatase single crystals [2,17,58] as well as polycrystalline anatase [16,58] showed transformation to TiO_2II at 2.5-7 GPa. In contrast, *Arlt et al.* [2] observed the transformation of polycrystalline anatase to MI without the formation of TiO_2II at 13 GPa. The experiments by *Swamy et al.* [4] and *Wang et al.* [212,213] led to the conclusion that a decrease in crystallite size suppresses the formation of TiO_2II and leads to a higher pressure of the transformation anatase \rightarrow MI (compare Table 13). The transformation of MI to OI was found at 30 GPa by laser heating to 1300-1500 K [18]. In this chapter, the effect of doping with 10 mol% Zr on the transition behavior is studied for micro- and nanoscale anatase. Experimental details are the same as for experiments on the compression behavior (compare section 3.1.).

The compression experiment at room temperature on microscale Zr-doped anatase showed anatase as single phase up to 13 GPa and the transformation of Zr-doped anatase to the MI phase took place between 13 and 20 GPa, which is higher than for TiO_2 microscale anatase. TiO_2II was not observed. Upon further compression to 50 GPa, the OII phase was identified, which remained stable after laser heating to 1500 K. Further heating to 2000 K led to the transformation into a single new phase, which could not be identified yet. The high pressure phase could be quenched to ambient conditions.

The experiment on Zr-doped nanoscale anatase showed the following pressure induced phase transformations. TiO_2II was not observed and the first reflections of coexisting MI and OI phases appeared at 14 GPa. Anatase remained present until 17 GPa. Laser heating at 35 GPa to \sim 1500-1600K conserved the phase assemblage of MI plus OI. Upon decompression to ambient conditions, the phases transformed to a mixture of TiO_2II plus OII. *Swamy et al.* [4] observed the preservation of nanocrystalline anatase TiO_2 until 16.5 GPa, comparable to our study. The authors found the first appearance of MI reflection at 18.2(4) GPa as opposed to 14 GPa for Zr-doped nanoanatase. They furthermore observed anatase stable up to 25 GPa, which is much higher than 17 GPa for

Zr-doped nanoanatase. No occurrence of the OI phase is reported in the study by *Swamy et al.* We therefore conclude that the doping with Zr stabilizes the OI phase within the pressure range of 14–35 GPa, coexisting with MI. In order to analyze whether or not the coexistence of the MI and OI phases over such a broad P-intervall, even after heating, is related to a chemical decomposition, we carried out a multi anvil experiment on Zr-doped nano-anatase at 20 GPa and 1200°C. A backscattered electron microprobe image on the quench product indicates two distinct phases (Figure 45). The brighter phase has crystallites sizes of $\leq 2 \mu\text{m}$, too small for quantitative analysis. Nevertheless measurements on larger individuals could be performed and revealed that the two phases have very similar composition, both ranging from TiO₂ contents of 83 to 95 mol%. The results do not yield at a chemical breakup.

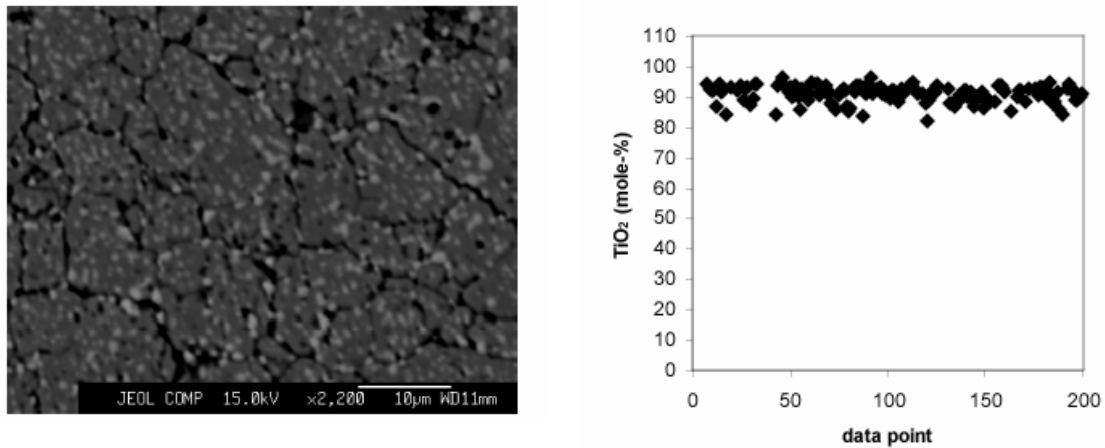


Figure 45: Backscattered electron image (left) and chemical composition (right) of multianvil experiment on Zr-doped nanoanatase at 20 GPa and 1200°C

4.3. DAC Experiments on Phase Transitions of Rutile

Upon compression, bulk rutile transforms to MI at ~12 GPa [19]. Nanoscale anatase was studied by *Olsen et al.* [20], using a ~10 nm starting material and the transformation to the MI phase was found between 20 and 30 GPa, which is much higher compared to bulk material. However, for this study ball milled powder was used and it is not clear how the strain induced by the method might affect the transition behavior. For a mixture of nanorutile + nanoanatase (30 nm) [213], transformation of nanoanatase to an amorphous phase after 16 GPa is reported, and of nanorutile to MI between 9 and 16 GPa. However, the high pressure transformation of rutile was not deduced explicitly. In order to do so, experiments on nanorutile were carried out on a number of samples with different crystallite sizes in the nanoscale, synthesized with a hydrothermal method [208] to reduce strain of the starting material. Furthermore, experiments on Zr-doped microscale rutile are reported.

4.3.1. TiO₂ Nanoscale Rutile

Several DAC experiments were carried out in order to reveal the effect of crystallite size on the pressure of transformation. It was furthermore tested, what effect the pressure medium has on the transformation behavior. Experiments using XRD without any pressure medium were performed on material with smallest dimensions of the crystallites of ~15 nm (a), ~10 nm (b) and ~8 nm (c), as indicated by high resolution TEM analysis (Figure 46) and on the smallest size additional experiments were performed with siliconoil as pressure medium, using XRD and XAS techniques. Experiments (a) and (b) and were performed at APS, using Cu as pressure calibrant and an X-ray beam with $\lambda=0.31$ Å and a size of 6×15 μm. The distance sample to detector was 272 mm. Experiment (c) was performed at BGI and the pressure was calibrated by Raman spectroscopy of a ruby crystal, incorporated in the sample chamber. The XRD experiment on the same sample with siliconoil as pressure medium was performed at APS and Cu served as pressure calibrant. The X-ray beam had a wavelength of $\lambda=0.275$ Å and a size of 6x15μm. The XAS experiment was performed in the transmission geometry at beamline ID12 at the ESRF, using soliconoil as pressure medium and a

ruby crystal as Raman-pressure calibrant, other experimental details can be found in ref. [165].

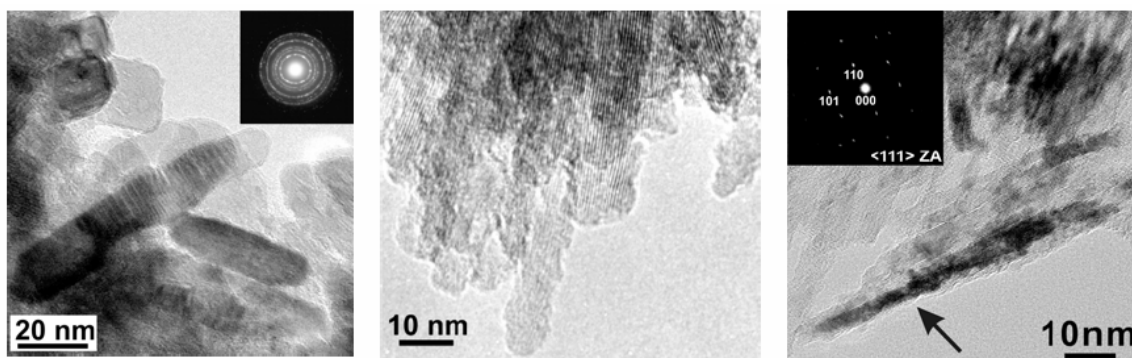


Figure 46: HRTEM images of nanoscale rutile starting materials a (left), b (middle) and c (right).

Rutile with the crystallite size of 15 nm (a) undergoes a phase transformation to the MI phase at pressures of ~ 18 GPa, which is much higher than observed for the bulk material (12 GPa). The MI phase was observed as the only phase at pressures of 32 to at least 45 GPa and remained present as the only phase after heating to ~ 1500 °C at 45 GPa (Figure 47), consistent with experiments on bulk rutile (APS).

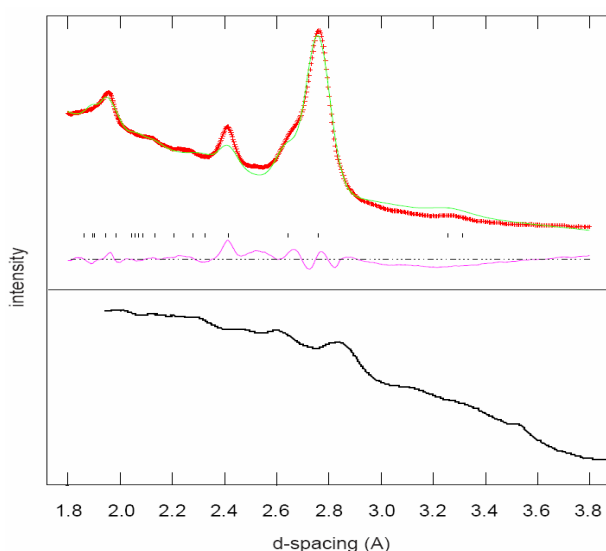


Figure 47: XRD patterns of high pressure phases upon compression of nanorutile. The top shows the full profile refinement of MI phase at 45 GPa after laser heating at 1500 °C, gained upon compression of starting material (a). The bottom shows an unidentified phase from compression of sample (b) to 44 GPa.

Rutile with smaller crystallite sizes of $\sim 10 \times 10 \times 50 \text{ nm}$ (b) remained present to even higher pressures: It was observed as single phase up to a pressure of 22 GPa, at 34 GPa the main phase was still rutile and at 44 GPa the material transformed in to a new phase which is not identified from the XRD data available (Figure 47). The sample with smallest crystallite size of $\sim 8 \times 8 \times 90 \text{ nm}$ (c) showed a decreasing intensity of rutile peaks at pressures $\geq 20 \text{ GPa}$ and vanishing 40 GPa. Unfortunately, the high pressure phase is not identified from the XRD data available (BGI), baddeleyite can be excluded. The comparison of experimental results from starting materials (a) and (b) suggest that decreasing crystallite size leads to stabilization of rutile to higher pressures. However, the use of siliconoil lowers the pressure of transformation as can be seen in XRD and XAS experiments on starting material (c): XRD patterns reveal that baddeleyite starts to form between 19 and 23 GP, while rutile remains present up to at least 33 GPa (Figure 48). In contrast, the baddeleyite phase could not be identified in the experiment in which no pressure medium was used. The results suggest that the choice of the pressure medium and thus the conditions of hydrostaticity affect the transition behavior.

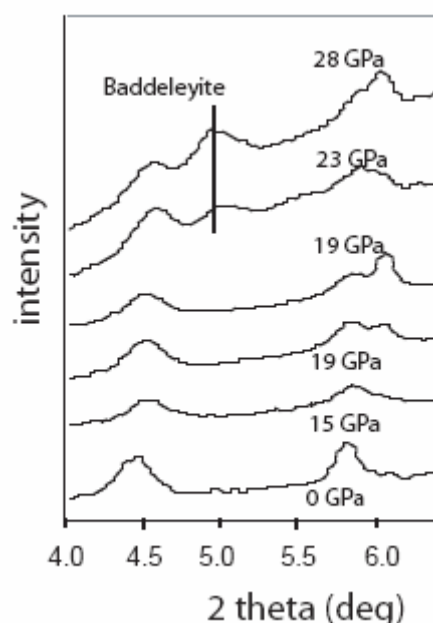


Figure 48: *In-situ* XRD spectra upon compression of nanorutile from the DAC experiment with starting material (c) and siliconoil

X-ray absorption spectroscopy (XAS) was performed in collaboration with Prof. Jean-Paul Itié at the synchrotron SOLEIL. K preedge spectra of Ti indicate that a transformation to the MI phase starts at 14 GPa and is complete at 20 GPa (Figure 49);

the quench product is TiO_2II . This pressure of transformation is lower than observed by XRD.

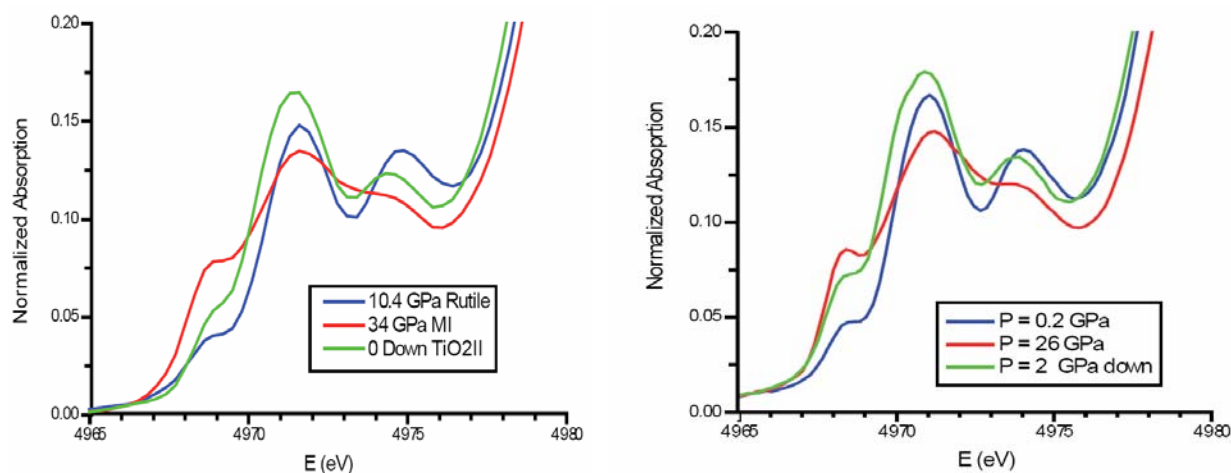


Figure 49: K pre-edge spectra for Ti. The left spectrum shows rutile, MI and TiO_2II phases for reference, the right spectrum shows *in-situ* experimental results from the compression of nanorutile.

Comparison of the results gained shows that the pressure of transformation generally increases with decreasing crystallite size and is lowered when siliconoil is used as pressure medium. However, results from XRD and XAS differ quantitatively.

4.3.2. Zr-doped Microscale Rutile

Experiments on Zr-doped rutile were performed in the presence of LiF, experimental details are described in section 3.3. The start of phase transitions to the MI phase was observed at 11 GPa, slightly lower pressure than observed for TiO_2 microscale rutile (12 GPa). Zr-doped rutile is present up to 20 GPa and the MI phase remained after laser heating to $\sim 1500^\circ\text{C}$ at 30 GPa.

5. Computational Ground States of TiO_2

Ab-initio all-electron density functional electronic structure simulations were performed, using the PAW method [182] as implemented in the Vienna *Ab-Initio* Simulation Package (VASP) [129,183] and the LAPW method [184] as implemented in the WIEN2k code [185,186]. LDA [128] and GGA [129] were used for computations with VASP and WIEN2k, and WC was used for computations with Wien2k [188].

Table 7: Equations of state from experiments and computations

Phase	Method	V (\AA^3)	E_0 (eV)	V_0 (\AA^3)	K_0 (GPa)	K_0'
rutile	exp [14]			62.50	230(20)	7(1)
	PAW_LDA	52-66	-9.788	60.93	246	4.0
	LAPW_LDA	52-66	-9087.058	60.55	254	4.0
	PAW_GGA	52-68	-8.969	64.37	214	4.0
	LAPW_GGA	52-68	-9111.519	64.16	219	4.0
	LAPW_WC	52-68	-9106.298	62.29	233	4.0
anatase	exp [2]			136.30	179(2)	5(1)
	PAW_LDA	112-140	-9.794	133.62	160	4.0
	LAPW_LDA	112-140	-9087.063	133.02	162	4.0
	PAW_GGA	120-152	-8.998	140.93	155	4.0
	LAPW_GGA	120-152	-9111.558	140.14	157	4.0
	LAPW_WC	120-144	-9106.315	137.19	149	4.0
α -PbO ₂	exp [19]			122.40	258(8)	4(1)
	PAW_LDA	104-128	-9.793	119.59	200	4.0
	LAPW_LDA	104-128	-9087.063	118.84	208	4.0
	PAW_GGA	104-136	-8.974	126.68	197	4.0
	LAPW_GGA	108-136	-9111.523	126.76	192	4.0
	LAPW_WC	104-128	-9106.288	123.16	167	4.0
brookite	exp [99]			257.80	255(10)	4
	PAW_LDA	208-272	-9.795	250.98	217	4.0
	LAPW_LDA	208-272	-9087.063	249.70	210	4.0
	PAW_GGA	208-288	-8.987	266.18	187	4.0
	LAPW_GGA	224-288	-9111.538	265.92	185	4.0
	LAPW_WC	208-272	-9106.307	256.82	203	4.0
baddeleyite	exp [14]			112.20	290(20)	4
	PAW_LDA	100-120	-9.802	112.00	190	4.0
	LAPW_LDA	100-120	-9087.069	111.50	194	4.0
	PAW_GGA	108-124	-8.940	120.72	147	4.0
	LAPW_GGA	108-124	-9111.483	121.27	134	4.0
	LAPW_WC	108-120	-9106.288	113.91	251	4.0

In the plane wave computations, plane wave cutoffs of $E_c=1000$ eV were included, which have been found necessary for computations on transition metal bearing oxides and silicates. In the LAPW method the plane waves were expanded up to $RK_{\max}=9.0$, with uniform muffin tin radii of 1.8 Bohr for Ti and 1.6 Bohr for O for all structures. Crystal structures were optimized for internal and external degrees of freedom at constant volumes, starting from experimental structures in the PAW computations (Table 9). Reciprocal space was sampled on Monkhorst-Pack k-point

III. Results and Discussion

grids [189], with the product of kpoints · atoms per unit cell >1944. Computations were performed for a wide volume range, allowing for a reliable fit to a third order Birch-Murnaghan EoS [190] (Table 8).

Table 8: Lattice parameters and atomic coordinates

Phase Space gr. (#)	Meth.	Atom (Pos.)	a (Å) x	b (Å) y	c (Å) z	α (°)	β (°)	γ (°)	V (Å ³)
rutile <i>P 4₂/m n m</i> (136)	exp	Ti (2a)	4.594	4.594	2.959	90	90	90	62.44
		O (4f)	0	0	0				
	LDA	Ti (2a)	0.3049	0.3049	0				
		O (4f)	4.563	4.563	2.927	90	90	90	60.93
	GGA	Ti (2a)	0	0	0				
		O (4f)	0.3038	0.3038	0				
anatase <i>I 4₁/a m d S</i> (141)	exp	Ti (2a)	4.658	4.658	2.968	90	90	90	64.37
		O (4f)	0	0	0				
	LDA	Ti (2a)	0	0	0				
		O (4f)	0.3046	0.3046	0				
	GGA	Ti (4a)	3.784	3.784	9.515	90	90	90	136.25
		O (8e)	0	0	0.2081				
α -PbO ₂ <i>P b c n</i> (60)	LDA	Ti (4a)	3.723	3.723	8.790	90	90	90	133.62
		O (8e)	0	0	0				
	GGA	Ti (4a)	0	0	0.2188				
		O (8e)	0	0	0.2057				
	exp	Ti (4c)	4.786	5.476	5.028	90	90	90	131.74
		O (8d)	0	0.2025	0.25				
LDA	Ti (4c)	0.2689	0.4024	0.4337					
	O (8d)	4.542	5.495	4.882	90	90	90	119.56	
brookite <i>P b c a</i> (61)	GGA	Ti (4c)	0	0.1743	0.25				
		O (8d)	0.2727	0.3812	0.4183				
	exp	Ti (4c)	4.582	5.606	4.934	90	90	90	126.68
		O (8d)	0	0.1773	0.25				
	LDA	Ti (8c)	0.2715	0.3805	0.4186				
		O (8c)	9.184	5.447	5.145	90	90	90	257.38
baddeleyite <i>P 2₁/c</i> (14)	GGA	Ti (8c)	0.1250	0.0980	0.8630				
		O (8c)	0.0080	0.1470	0.1820				
	exp	O (8c)	0.2290	0.1100	0.5300				
		Ti (8c)	9.125	5.403	5.091	90	90	90	125.49
	LDA	Ti (8c)	0.1289	0.0972	0.8618				
		O (8c)	0.0103	0.1494	0.1844				
baddeleyite <i>P 2₁/c</i> (14)	GGA	O (8c)	0.2303	0.1101	0.5348				
		Ti (8c)	9.282	5.521	5.194	90	90	90	133.09
	exp	O (8c)	0.1289	0.0926	0.8614				
		Ti (4e)	0.0103	0.1482	0.1826				
	LDA	O (4e)	0.2292	0.1068	0.5349				
		Ti (4e)	5.145	5.208	5.311	90	99.23	90	140.46
baddeleyite <i>P 2₁/c</i> (14)	GGA	O (4e)	0.2758	0.0404	0.2089				
		Ti (4e)	0.0690	0.3420	0.3450				
	exp	O (4e)	0.4510	0.7580	0.4790				
		Ti (4e)	4.744	4.844	4.947	90	101.63	90	112.01
	LDA	O (4e)	0.2794	0.0528	0.2119				
		Ti (4e)	0.0684	0.3352	0.3400				
GGA	O (4e)	0.4412	0.7592	0.4757					
	Ti (4e)	4.878	4.914	5.126	90	101.52	90	120.72	
	O (4e)	0.2753	0.0583	0.2180					
	O (4e)	0.0589	0.3159	0.3593					
		O (4e)	0.4510	0.7583	0.4548				

Following the known trend for most materials, LDA both in the PAW and LAPW computations underestimates experimental values of V_0 , although in the case of the TiO₂ structures by less than 3%. Bulk moduli of rutile are well reproduced, larger by

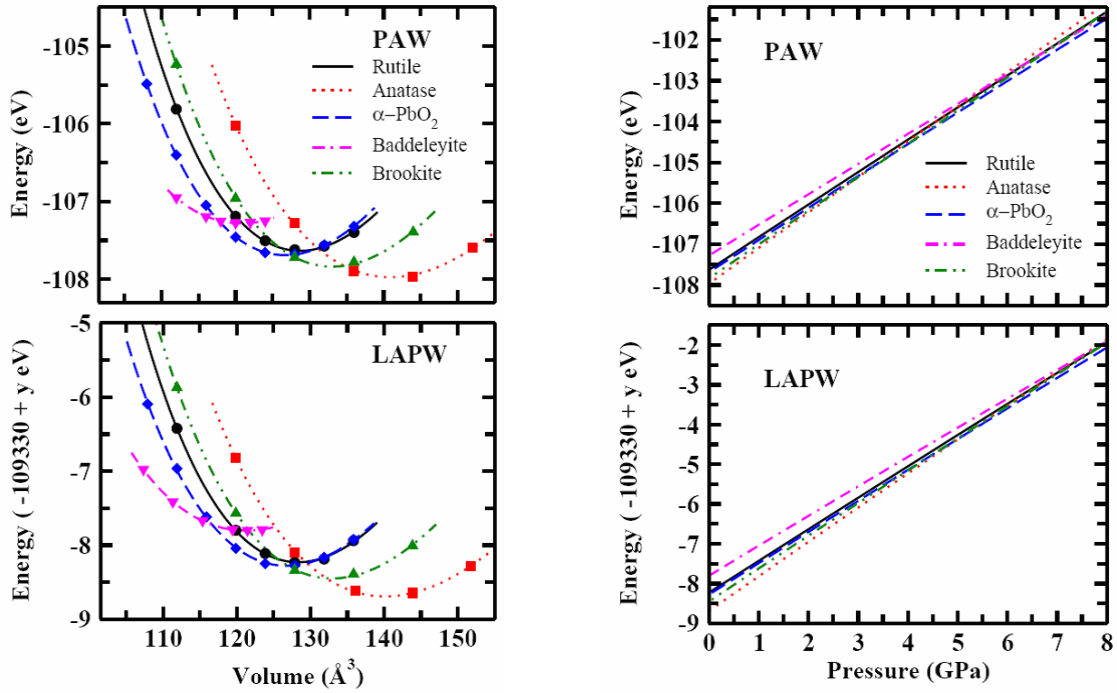


Figure 51: Computational results of PBE on TiO_2 phases. On the lefthand side, energy-volume data (symbols) and equation of state fits (lines) are shown, volumes are normalized to 12 atoms per unit cell. The right hand side shows energy-pressure data calculated from the equations of state.

In the PBE computations, experimental V_0 are overestimated by 8% for baddeleyite and less than 4% for other TiO_2 phases in PAW as well as LAPW computations, following the general trend for PBE. The bulk modulus of rutile is well reproduced, smaller by 7% for PAW and 5% for LAPW. Bulk moduli of anatase are underestimated by 14% (PAW) and 12% (LAPW), for $\alpha\text{-PbO}_2$ by 24% (PAW) and 26% (LAPW), for brookite by 27% (PAW and LAPW) and for baddeleyite by 49% (PAW) and 54% (LAPW). Axial ratios for all phases are within 2% of the experimental values. Atomic coordinates for rutile, anatase and brookite are in good agreement with experiment, for baddeleyite and $\alpha\text{-PbO}_2$ the atomic coordinates are considerably different (Table 9). The stable structure at ambient pressure is anatase. Rutile has low relative stability (Table 10 and Figure 51).

WC in the LAPW computations estimates experimental values of V_0 larger by only 0.4% and therefore is the most appropriate approximation. The bulk modulus of rutile is well reproduced, larger by only 1%. Bulk moduli for anatase are underestimated by 17%, for $\alpha\text{-PbO}_2$ by 35%, for brookite by 20% and for baddeleyite by 13%. The

stable structure at ambient pressure is anatase. Rutile has intermediate relative stability (Table 10 and Figure 52).

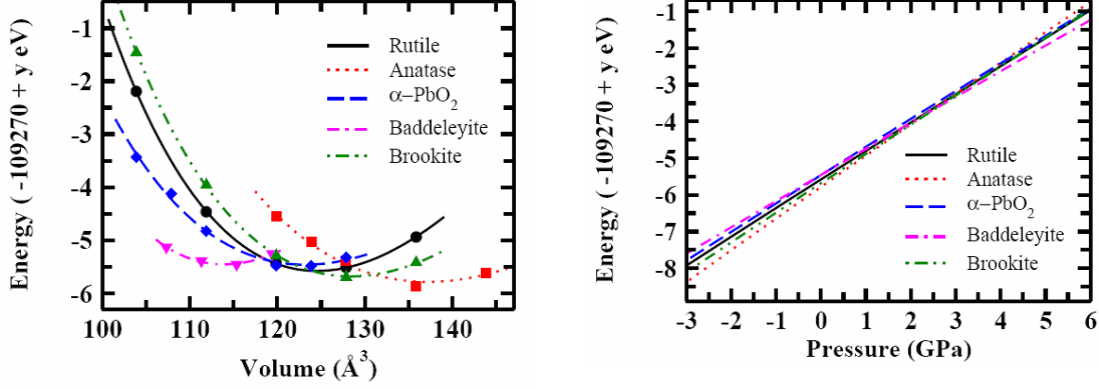


Figure 52: Computational results of WC on TiO_2 phases. On the lefthand side, energy-volume data (symbols) and equation of state fits (lines) are shown, volumes are normalized to 12 atoms per unit cell. The right hand side shows energy-pressure data calculated from the equations of state.

The stable structures at ambient pressure (0 GPa) is baddeleyite for LDA computations and anatase for GGA computations, contradicting experimental results that determine rutile as the most stable phase [64-66]. However, rutile appears to have the highest energy in LDA computations and intermediate energy in GGA computations.

Table 9: Internal energies and phase transformations at zero pressure

PAW_LDA phase	E_0 (eV)	LAPW_LDA phase	E_0 (eV)	PAW_PBE phase	E_0 (eV)	LAPW_PBE phase	E_0 (eV)	LAPW_WC phase	E_0 (eV)
rutile	-117.449	rutile	109044.699	baddeleyite	-107.281	baddeleyite	109337.804	baddeleyite	109275.455
α -PbO ₂	-117.516	brookite	109044.748	rutile	-107.635	rutile	109338.230	α -PbO ₂	109275.460
anatase	-117.534	α -PbO ₂	109044.749	α -PbO ₂	-107.691	α -PbO ₂	109338.279	rutile	109275.578
brookite	-117.538	anatase	109044.755	brookite	-107.838	brookite	109338.450	brookite	109275.682
baddeleyite	-117.617	baddeleyite	109044.832	anatase	-107.974	anatase	109338.693	anatase	109275.784
phase	P_{trans} (GPa)	phase	P_{trans} (GPa)	phase	P_{trans} (GPa)	phase	P_{trans} (GPa)	phase	P_{trans} (GPa)
anatase → baddeleyite	-0.7	anatase → baddeleyite	-0.6	anatase → brookite → α -PbO ₂	3.0 3.5	anatase → α -PbO ₂	5.2	anatase → brookite → baddeleyite	1.9 2.5

The following phase transformations are predicted by LDA: anatase → baddeleyite at -0.7 GPa (PAW) and -0.6 GPa (LAPW). For PBE results are anatase → brookite at 3.0 GPa → α -PbO₂ at 3.5 GPa (PAW) whereas LAPW predicts anatase → α -PbO₂ at 5.2 GPa. WC predicts anatase → brookite at 1.9 GPa and brookite →

baddelyite at 2.5 GPa. Compared to that compression experiments on single crystal and microcrystalline anatase showed transformation into α -PbO₂ at pressures of 2-4 GPa [2,16,17,58]. Rutile and α -PbO₂ transform into baddeleyite at ~ 13 GPa [2,11].

IV. Conclusions

This study addresses the effect of Zr-doping and crystallite size on the mechanical properties of TiO₂ rutile and anatase phases. Compression experiments in the diamond anvil cell using *in-situ* XRD were performed and the compressibilities of the samples were determined. Therefore, pressure-volume data were fitted to equations of state (EoS) and the zero-pressure volume V_0 , the bulk modulus K_0 and the first pressure derivative of the bulk modulus K_0' were obtained. During compression experiments, the transformations to high pressure polymorphs were observed and the effect of Zr-doping and crystallite size on the transition behavior was studied. Furthermore, *ab-initio* computations were performed to predict the EoS parameters theoretically. Table 11 shows a list of studies found in literature and performed here (marked with X).

Table 10: Experimental and computational studies on rutile and anatase

		μm	nm	comp
Anatase	TiO ₂	refs. [1,2]	refs. [3,4]	X
	Ti _{0.9} Zr _{0.1} O ₂	X	X	X
Rutile	TiO ₂	refs. [14,19,20]	X	X
	Ti _{0.9} Zr _{0.1} O ₂	X	n.a.	n.a.

μm = Experiments on microscale material; nm = experiments on nanoscale material; comp = *ab-initio* computational study

Crystallite Size Effect on TiO₂ Anatase and Rutile

Anatase becomes less compressible when the crystallite size is decreased to the nanometer scale. *Ab-initio* computations on TiO₂ anatase with periodic boundary conditions, thus computing an infinite crystal, have lowest bulk modulus of 149 – 153 GPa, depending on the computational approximations used (Table 12). The bulk modulus of microcrystalline anatase was measured as $K_0=178(1)$ GPa [1] and 179(2) GPa [2] GPa, the nanoscale counterpart shows $K_0=237(3)$ GPa [3] and 243(3) [4] GPa (Table 12).

In contrast, the compression behavior of rutile is not affected by variation of the crystallite size. Computations with periodic boundary conditions give a bulk modulus of 233 GPa, experiments on microscale rutile revealed a bulk modulus of $K_0=230(20)$ GPa [20] and the nanoscale counterpart has $K_0=203(13)$ (Table 12).

The pressure induced phase transformations of anatase and rutile are described in Table 13. Transformation of anatase to TiO_2II is only observed for TiO_2 single crystals and some microscale polycrystalline materials at a pressure of 2.6–7 GPa; TiO_2II transforms to the MI phase at 10–17 GPa (details in Table 13). The transformation of anatase to MI was observed for micro- and nanoscale TiO_2 . The pressure of transformation increases with a decrease of the crystallite size from 13 GPa (microscale material) to 18 GPa for 12 nm particles. Smaller particles transform to an amorphous phase at pressures of 20–24 GPa. Pressure induced transformation of rutile to the MI phase was observed at a pressure of 12 GPa, nanocrystals transform at higher pressures. The onset of transformation is at 16–23 GPa when ref. [213], in which the detection of the high pressure phase seems unreliable, is excluded.

The pressure induced phase transformations predicted by the *ab-initio* computational study are not consistent with experimental results. Rutile, which is the stable modification of TiO_2 (e.g. [63]), has lowest to intermediate energy (Table 12) in computations. The transformation of anatase into TiO_2II was predicted very well at a pressure of 3.5 GPa (PAW-PBE) and 5.2 (LAPW_PBE), the pressure of transformation of anatase into MI was calculated slightly lower observed experimentally at -1 GPa (LDA) and 2.5 GPa (WC) (Tables 10 and 12).

Table 11: Equation of state parameters for anatase and rutile

Material	Size	V_0 (Å ³)	K_0 (GPa)	K'_0	Reference
Anatase TiO ₂	WC ²	137.19	149	4.0	this study
	LDA ²	133.62	160	4.0	this study
	LDA ¹	141.1	153	4.0	this study
	μm	136.8	178(1), 179(2)		[1,2]
	nm	136.2	237(3), 243(3)		[3,4]
Ti _{0.9} Zr _{0.1} O ₂	LDA ¹	145.4	161	4.0	
	μm	138.5(1)	195(38)	4.0	
	nm	139.4(1)	258(8)	4.0	[203], this study
Rutile TiO ₂	WC	62.29	233	4.0	this study
	μm	62.5	230(20)	6.6(7)	[14,19,20]
	nm	62.50(9)	203(13)	4.0	this study
Ti _{0.9} Zr _{0.1} O ₂	μm	63.94(5)	236(5)	6.6(7)	this study

Effect of Zr-Doping on TiO₂ Anatase and Rutile

In order to determine the maximum amount of Zr that can be incorporated into TiO₂ polymorphs, experiments were carried out at temperatures of 1200–1600 °C and pressures of 2–10 GPa, using the piston cylinder and multi anvil press. Run products were analyzed by XRD and microprobe analysis. Results show that rutile and high pressure polymorphs to 10 GPa incorporate up to 10 mol% ZrO₂. Therefore, for experiments on Zr-doped anatase and rutile, starting materials with composition Ti_{0.9}Zr_{0.1}O₂ were used. The high pressure experiments furthermore revealed that the high pressure limit of the stability of srilankite lies between 3.5 and 6 GPa, important for geosciences in understanding the origin and conditions for the genesis of the mineral.

For synthesis of Zr-doped nanoscale and microscale starting materials, a route of sol-gel synthesis was developed and nanoscale anatase Ti_xZr_{1-x}O₂ with x = 0.90 and 1.0 was produced. Microscale Zr-doped rutile was synthesized hydrothermally at a pressure of 0.1 GPa and temperature of 300°C, using the nanoscale Zr-doped anatase from sol-gel synthesis as starting material.

Table 12: Pressure induced phase transformations of anatase and rutile

Chem.	Size	Anatase→TiO₂II P (GPa)	TiO₂II→MI P (GPa)	Anatase→MI, AP; P (GPa)	P- medium	Ref.		
TiO ₂	comp	3.5 – 5.2		-1 – 2.5		this work		
	SC	4.5; 4.5 - 7			Meth.-eth	[2,17]		
	μm			13 - 17		Meth.-eth.	[17]	
		2.6				Meth.-eth.	[58]	
		~ 7		~ 10		Siliconoil	[16]	
				13 (MI)		NaCl	[1]	
	30-40 nm			18 (MI)		none	[4]	
	12 nm			18 (MI)		Liqu. Nit.	[214]	
	7-11 nm			24 (AP)		Meth.-eth.	[212]	
	4-8 nm			20 - 24 (AP)		none	[207]	
Ti _{0.9} Zr _{0.1} O ₂	μm			13 – 20 (MI)		none	this work	
	12 nm			14 – 17 (MI)		LiF	this work	
Chem.	Size	Rutile→TiO₂II P (GPa)	TiO₂II→MI P (GPa)	Rutile→MI P (GPa)	P- medium	Ref.		
TiO ₂	μm			12		Meth.-eth.	[14]	
	μm			12		NaCl	[55]	
	30 nm			9 - 16		none	[213]	
	15 nm			18		none	this work	
	10 nm			20 - 30		none	[20]	
	8 nm			> 20		none	this work	
	8 nm				23 - 33		Si-oil	this work
							XRD	
8 nm				14 - 20		Si-oil	this work	
						XAS		
Ti _{0.9} Zr _{0.1} O ₂	μm			11 - 20		LiF	this work	

Comp = computations, compare Table 10, MI = baddeleyite structured phase, AP = amorphous phase

The compressibility of high-pressure polymorphs of TiO₂ is systematically smaller than for ZrO₂ (compare Table 1). Nevertheless, doping with 10% Zr leads to stiffening of nanoscale anatase: TiO₂ nanoanatase has a bulk modulus of K₀=237(3) GPa [3] and K₀=243(3) GPa [4] GPa, while the Zr-doped counterpart shows K₀=258(8) GPa. However, differences for microscale anatase samples are within the error: K₀=178(1) GPa [1] and K₀=179(2) GPa [2] for TiO₂ and K₀=195(38) GPa for

$\text{Ti}_{0.90}\text{Zr}_{0.10}\text{O}_2$. A similar relationship was observed for rutile, where the bulk moduli of the undoped microscale rutile and the doped counterpart are 230(20) GPa [20] and 203(13) GPa.

XRD analysis showed a significant change in compression behavior for the Zr-doped nanoanatase at pressures >4 GPa. It is likely to be a consequence of deviatoric stresses during experimental compression of the nanoscale material. Computations on supercells with different distances of neighboring Zr-atoms suggested cluster formation of Zr in the (Ti,Zr) O_2 anatase. The resulting structural distortions can further augment the change in compression behavior.

It was found that Zr-doped nanoanatase becomes stiffer upon multiple compression cycles. The bulk modulus of the first compression was 211 GPa. After decompression of the sample, the second compression showed a bulk modulus of 249 GPa. It is suggested that partial pressure induced amorphization plays an important role for the observed stiffening.

The transformation pressure of anatase and rutile to the MI phase is not affected by Zr-doping.

Acknowledgments

This work was made possible through collaboration with a number of people from BGI as well as other research groups and I want to thank them for their support. First of all, I want to thank my advisors Dr. Leonid Dubrovinsky, Dr. Gerd Steinle-Neumann and Prof. Gerd Müller for all of their teaching, advice and discussions about the design and evolving progress of my thesis. I was well supported. I appreciate the support of my colleagues at BGI in science (Dr. Dan Frost, Dr. Tiziana Boffa-Ballaran, Dr. Nobuyoshi Miyajima, Dr. Alexander Kurnosov, Dr. Innokenty Kantor, Dr. David Dolejš, Dr. Razvan Caracas, Dr. Ahmed El Goresy, Prof. Dave Rubie, Prof. Hans Keppler), organization (Dr. Stefan Keyssner, Lydia Kison-Herzing, Petra Buchert) and technical support (Gerti Gollner, Hubert Schulze, Heinz Fischer, Stefan Übelhack, Detlef Krauß, Sven Linhardt, Anke Potzel). I want to thank the following people from outside BGI: Dr. Vitali Prakapenka, Dr. Alexei Kuznetsov and Dr. Varghese Swamy for their support on the GeoSoilEnviroCARS 13 IDD at the Advanced Photon Source (APS), USA; Prof. Jean-Paul Itié for absorption experiments at the synchrotron SOLEIL, France; Prof. Vladimir Dmitriev for XRD measurements at the Swiss Norwegian beamline at ESRF, France; Dr. Richard Wirth from the GFZ, Potsdam for TEM analysis; Dr. Peer Löbmann and Matthias Bockmeyer from the Fraunhofer ISC, Würzburg, for support with the sol-gel synthesis. This work was financed by the Elitenetzwerk Bayern of the Bayerisches Staatsministerium für Wissenschaft, Forschung und Kunst in the international graduate school “Oxides”. I want to thank for the financial support and network activities.

Furthermore I would like to thank my family, friends and teachers who encouraged me to take my scientific path and stay on it. I want to thank Werner Ebert who helped me build the foundation of my scientific career; Werner Thiemann, Prof. Klaus Jacobs and Prof. Timothy Grove for sharing their great inspiration and passion for science with me; my teachers from the CITA studio for supporting me during hard times; Ulrike, Isabella, Silvia and Silke, you wonderful women who always reminded me of whom I am. And I want to thank Stefan.

Bibliography

- [1] V. Swamy and L.S. Dubrovinsky, Bulk modulus of anatase, *Journal of Physics and Chemistry of Solids* 62 (2001) 673-675.
- [2] T. Arlt, M. Bermejo, M.A. Blanco, L. Gerward, J.Z. Jiang, J.S. Olsen and J.M. Recio, High-pressure polymorphs of anatase TiO₂, *Physical Review B* 61 (2000) 14414-14419.
- [3] V. Pischedda, G.R. Hearne, A.M. Dawe and J.E. Lowther, Ultrastability and enhanced stiffness of similar to 6 nm TiO₂ nanoanatase and eventual pressure-induced disorder on the nanometer scale, *Physical Review Letters* 96 (2006) 035509.
- [4] V. Swamy, L.S. Dubrovinsky, N.A. Dubrovinskaia, A.S. Simionovici, M. Drakopoulos, V. Dmitriev and H.P. Weber, Compression behavior of nanocrystalline anatase TiO₂, *Solid State Communications* 125 (2003) 111-115.
- [5] J. Haines, J.M. Leger and O. Schulte, The high-pressure phase transition sequence from the rutile-type through to the cotunnite-type structure in PbO₂, *Journal of Physics-Condensed Matter* 8 (1996) 1631-1646.
- [6] J.M. Leger, J. Haines and A. Atouf, The high pressure behaviour of the cotunnite and post-cotunnite phases of PbCl₂ and SnCl₂, *Journal of Physics and Chemistry of Solids* 57 (1996) 7-16.
- [7] R. Ahuja and L.S. Dubrovinsky, High-pressure structural phase transitions in TiO₂ and synthesis of the hardest known oxide, *Journal of Physics-Condensed Matter* 14 (2002) 10995-10999.
- [8] R. Ahuja and L.S. Dubrovinsky, Cotunnite-structured titanium dioxide and the hardest known oxide, *High Pressure Research* 22 (2002) 429-433.
- [9] N.A. Dubrovinskaia, L.S. Dubrovinsky, R. Ahuja, V.B. Prokopenko, V. Dmitriev, H.P. Weber, J.M. Osorio-Guillen and B. Johansson, Experimental and theoretical identification of a new high-pressure TiO₂ polymorph, *Physical Review Letters* 87 (2001) 275501 1-4.
- [10] N.A. Dubrovinskaia, L.S. Dubrovinsky, V. Swamy and R. Ahuja, Cotunnite-structured titanium dioxide, *High Pressure Research* 22 (2002) 391-394.
- [11] L.S. Dubrovinsky, N.A. Dubrovinskaia, V. Swamy, J. Muscat, N.M. Harrison, R. Ahuja, B. Holm and B. Johansson, Materials science - The hardest known oxide, *Nature* 410 (2001) 653-654.
- [12] A. El Goresy, M. Chen, L. Dubrovinsky, P. Gillet and G. Graup, An ultradense polymorph of rutile with seven-coordinated titanium from the Ries crater, *Science* 293 (2001) 1467-1470.
- [13] A. El Goresy, M. Chen, P. Gillet, L. Dubrovinsky, G. Graup and R. Ahuja, A natural shock-induced dense polymorph of rutile with alpha-PbO₂ structure in the suevite from the Ries crater in Germany, *Earth and Planetary Science Letters* 192 (2001) 485-495.
- [14] L. Gerward and J.S. Olsen, Post-rutile high-pressure phases in TiO₂, *Journal of Applied Crystallography* 30 (1997) 259-264.
- [15] L. Gerward and J.S. Olsen, High-pressure behaviour of titanium dioxide, in: *European Powder Diffraction: Epdic Iv, Pts 1 and 2* (1996), pp. 383-386.

- [16] J. Haines and J.M. Leger X-Ray-Diffraction Study of TiO₂ up to 49 Gpa, *Physica B* 192 (1993) 233-237.
- [17] K. Lagarec and S. Desgreniers, Raman-Study of Single-Crystal Anatase TiO₂ up to 70 Gpa, *Solid State Communications* 94 (1995) 519-524.
- [18] M. Mattesini, J.S. de Almeida, L. Dubrovinsky, N. Dubrovinskaia, B. Johansson and R. Ahuja, High-pressure and high-temperature synthesis of the cubic TiO₂ polymorph, *Physical Review B* 70 (2004) 212101 1-4.
- [19] J.S. Olsen, L. Gerward and J.Z. Jiang, On the rutile/alpha-PbO₂-type phase boundary of TiO₂, *Journal of Physics and Chemistry of Solids* 60 (1999) 229-233.
- [20] J.S. Olsen, L. Gerward and J.Z. Jiang, High-pressure behavior of nano titanium dioxide, *High Pressure Research* 22 (2002) 385-389.
- [21] T. Sasaki, Stability of rutile-type TiO₂ under high pressure, *Journal of Physics-Condensed Matter* 14 (2002) 10557-10562.
- [22] H. Sato, S. Endo, M. Sugiyama, T. Kikegawa, O. Shimomura and K. Kusaba, Baddeleyite-Type High-Pressure Phase of TiO₂, *Science* 251 (1991) 786-788.
- [23] V. Swamy, N.A. Dubrovinskaia and L.S. Dubrovinsky, Compressibility of baddeleyite-type TiO₂ from static compression to 40 GPa, *Journal of Alloys and Compounds* 340 (2002) 46-48.
- [24] A.C. Withers, E.J. Essene and Y.X. Zhang, Rutile/TiO₂II phase equilibria, *Contributions to Mineralogy and Petrology* 145 (2003) 199-204.
- [25] P. Bouvier, E. Djurado, G. Lucazeau and T. Le Bihan, High-pressure structural evolution of undoped tetragonal nanocrystalline zirconia, *Physical Review B* 62 (2000) 8731-8737.
- [26] T.K. Gupta, F.F. Lange and J.H. Bechtold, Effect of Stress-Induced Phase-Transformation on Properties of Polycrystalline Zirconia Containing Metastable Tetragonal Phase, *Journal of Materials Science* 13 (1978) 1464-1470.
- [27] J. Haines, J.M. Leger and A. Atouf, Crystal-Structure and Equation of State of Cotunnite-Type Zirconia, *Journal of the American Ceramic Society* 78 (1995) 445-448.
- [28] J. Haines, J.M. Leger, S. Hull, J.P. Petitet, A.S. Pereira, C.A. Perottoni and J.A.H. da Jornada, Characterization of the cotunnite-type phases of zirconia and hafnia by neutron diffraction and Raman spectroscopy, *Journal of the American Ceramic Society* 80 (1997) 1910-1914.
- [29] G. Kulcinsk., High-Pressure Induced Phase Transition in ZrO₂, *Journal of the American Ceramic Society* 51 (1968) 582-&.
- [30] O. Ohtaka, S. Kume and E. Ito, Stability Field of Cotunnite-Type Zirconia, *Journal of the American Ceramic Society* 73 (1990) 744-745.
- [31] O. Ohtaka, S. Kume and E. Ito, Synthesis and Phase-Stability of Cotunnite-Type Zirconia, *Journal of the American Ceramic Society* 71 (1988) C448-C449.
- [32] O. Ohtaka, D. Andraut, P. Bouvier, E. Schultz and M. Mezouar, Phase relations and equation of state of ZrO₂ to 100 GPa, *Journal of Applied Crystallography* 38 (2005) 727-733.
- [33] O. Ohtaka, H. Fukui, K. Funakoshi, W. Utsumi, T. Irifune and T. Kikegawa, Phase relations and EOS of ZrO₂ and HfO₂ under high-temperature and high-pressure, *High Pressure Research* 22 (2002) 221-226.
- [34] O. Ohtaka, H. Fukui, T. Kunisada, T. Fujisawa, K. Funakoski, W. Utsumi, T. Irifune, K. Kuroda and T. Kikegawa, Phase relations and equations of state of

- ZrO₂ under high temperature and high pressure, *Physical Review B* 6317 (2001) 174108.
- [35] O. Ohtaka, T. Yamanaka, S. Kume, E. Ito and A. Navrotsky, Stability of Monoclinic and Orthorhombic Zirconia - Studies by High-Pressure Phase-Equilibria and Calorimetry, *Journal of the American Ceramic Society* 74 (1991) 505-509.
- [36] O. Ohtaka, T. Yamanaka and T. Yagi New High-Pressure and High-Temperature Phase of ZrO₂ above 1000 °C at 20 Gpa, *Physical Review B* 49 (1994) 9295-9298.
- [37] J.E. Lowther, J.K. Dewhurst, J.M. Leger and J. Haines, Relative stability of ZrO₂ and HfO₂ structural phases, *Physical Review B* 60 (1999) 14485-14488.
- [38] S. Desgreniers and K. Lagarec, High-density ZrO₂ and HfO₂: Crystalline structures and equations of state, *Physical Review B* 59 (1999) 8467-8472.
- [39] G.A. Kourouklis and E. Liarakis, Pressure and Temperature-Dependence of the Raman-Spectra of Zirconia and Hafnia, *Journal of the American Ceramic Society* 74 (1991) 520-523.
- [40] L.G. Liu, New High-Pressure Phases of ZrO₂ and HfO₂, *Journal of Physics and Chemistry of Solids* 41 (1980) 331-334.
- [41] Bendelia.Na, S.V. Popova and L. Verescha, New High Pressure Modifications of ZrO₂ and HfO₂, *Geochemistry International Ussr* 4 (1967) 557-559.
- [42] A. Jayaraman, S.Y. Wang, S.K. Sharma and L.C. Ming, Pressure-Induced Phase-Transformations in HfO₂ to 50 Gpa Studied by Raman-Spectroscopy, *Physical Review B* 48 (1993) 9205-9211.
- [43] J.E. Jaffe, R.A. Bachorz and M. Gutowski, Low-temperature polymorphs of ZrO₂ and HfO₂: A density-functional theory study, *Physical Review B* 72 (2005).
- [44] J.M. Leger, A. Atouf, P.E. Tomaszewski and A.S. Pereira, Pressure-Induced Phase-Transitions and Volume Changes in HfO₂ up to 50 Gpa, *Physical Review B* 48 (1993) 93-98.
- [45] S.N. Luo, J.L. Mosenfelder, P.D. Asimow and T.J. Ahrens, Direct shock wave loading of Stishovite to 235 GPa: Implications for perovskite stability relative to an oxide assemblage at lower mantle conditions, *Geophysical Research Letters* 29 (2002).
- [46] D. Andrault, G. Fiquet, J.P. Itie, P. Richet, P. Gillet, D. Hausermann and M. Hanfland, Thermal pressure in the laser-heated diamond-anvil cell: An X-ray diffraction study, *European Journal of Mineralogy* 10 (1998) 931-940.
- [47] V. Swamy, S.K. Saxena, B. Sundman and J. Zhang, A Thermodynamic Assessment of Silica Phase-Diagram, *Journal of Geophysical Research-Solid Earth* 99 (1994) 11787-11794.
- [48] R.T. Downs and D.C. Palmer, The Pressure Behavior of Alpha-Cristobalite, *American Mineralogist* 79 (1994) 9-14.
- [49] L.G. Liu, Bulk Moduli of SiO₂ Polymorphs - Quartz, Coesite and Stishovite, *Mechanics of Materials* 14 (1993) 283-290.
- [50] R.G. McQueen, J.C. Jamieson and S.P. Marsh, Shock-Wave Compression and X-Ray Studies of Titanium Dioxide, *Science* 155 (1967) 1401-&.
- [51] R. Marchand, L. Brohan and M. Tournoux, TiO₂(B) a New Form of Titanium-Dioxide and the Potassium Octatitanate K₂Ti₈O₁₇, *Materials Research Bulletin* 15 (1980) 1129-1133.

- [52] M. Lacroche, L. Brohan, R. Marchand and M. Tournoux, New Hollandite Oxides - $\text{TiO}_2(\text{H})$ and $\text{K}_{0.06}\text{TiO}_2$, *Journal of Solid State Chemistry* 81 (1989) 78-82.
- [53] J. Akimoto, Y. Gotoh, Y. Oosawa, N. Nonose, T. Kumagai, K. Aoki and H. Takei, Topotactic Oxidation of Ramsdellite-Type $\text{Li}_{10.5}\text{TiO}_2$, a New Polymorph of Titanium-Dioxide - $\text{TiO}_2(\text{R})$, *Journal of Solid State Chemistry* 113 (1994) 27-36.
- [54] J.F. Banfield, B.L. Bischoff and M.A. Anderson, TiO_2 Accessory Minerals - Coarsening, and Transformation Kinetics in Pure and Doped Synthetic Nanocrystalline Materials, *Chemical Geology* 110 (1993) 211-231.
- [55] J. Tang and S. Endo, P-T Boundary of Alpha- PbO_2 Type and Baddeleyite Type High-Pressure Phases of Titanium-Dioxide, *Journal of the American Ceramic Society* 76 (1993) 796-798.
- [56] M. Akaogi, K. Kusaba, J. Susaki, T. Yagi, M. Matsui, T. Kikegawa, H. Yusa and E. Ito in: Y. Syono, M.H. Manghanni (Eds). *High-Pressure Research: Application to Earth and Planetary Sciences*, Terra Scientific Publishing Company, Tokyo (1992) 447.
- [57] V. Swamy, E. Holbig, L. Dubrovinsky, V. Prakapenka and B.C. Muddle, Mechanical properties of bulk and nanoscale TiO_2 phases, *Journal of Physics and Chemistry of Solids* (submitted) (2007).
- [58] T. Ohsaka, S. Yamaoka and O. Shimomura, Effect of Hydrostatic-Pressure on the Raman-Spectrum of Anatase (TiO_2), *Solid State Communications* 30 (1979) 345-347.
- [59] G.R. Lumpkin, Physical and chemical characteristics of baddeleyite (monoclinic zirconia) in natural environments: an overview and case study, *Journal of Nuclear Materials* 274 (1999) 206-217.
- [60] D. Viehnic and V.S. Stubican, Phase Studies within System $\text{ZrO}_2\text{-MgO}$, *Nature* 206 (1965) 1251-&.
- [61] R.E. Latta, E. Duderstadt and R.E. Fryxell, Melting Point of Pure Zirconia, *Journal of Nuclear Materials* 35 (1970) 345-&.
- [62] A. Navrotsky, Calorimetry of nanoparticles, surfaces, interfaces, thin films, and multilayers, *Journal of Chemical Thermodynamics* 39 (2007) 1-9.
- [63] M.R. Ranade, A. Navrotsky, H.Z. Zhang, J.F. Banfield, S.H. Elder, A. Zaban, P.H. Borse, S.K. Kulkarni, G.S. Doran and H.J. Whitfield, Energetics of nanocrystalline TiO_2 , *Proceedings of the National Academy of Sciences of the United States of America* 99 (2002) 6476-6481.
- [64] T. Mitsuhashi and O.J. Kleppa, Transformation Enthalpies of the TiO_2 Polymorphs, *Journal of the American Ceramic Society* 62 (1979) 356-357.
- [65] Navrotsk.A and O.J. Kleppa, Enthalpy of Anatase-Rutile Transformation, *Journal of the American Ceramic Society* 50 (1967) 626-&.
- [66] Navrotsk.A, J.C. Jamieson and O.J. Kleppa, Enthalpy of Transformation of a High-Pressure Polymorph of Titanium Dioxide to Rutile Modification, *Science* 158 (1967) 388-&.
- [67] P.Y. Shen, S.L. Hwang, H.T. Chu, T.F. Yu, C.N. Pan and W.L. Huang, On the transformation pathways of alpha- PbO_2 -type TiO_2 at the twin boundary of rutile bicrystals and the origin of rutile bicrystals, *European Journal of Mineralogy* 17 (2005) 543-552.

- [68] M.W. Pitcher, S.V. Ushakov, A. Navrotsky, B.F. Woodfield, G.S. Li, J. Boerio-Goates and B.M. Tissue, Energy crossovers in nanocrystalline zirconia, *Journal of the American Ceramic Society* 88 (2005) 160-167.
- [69] A.E. McHale and R.S. Roth, Investigation of the Phase-Transition in $ZrTiO_4$ and $ZrTiO_4$ - SnO_2 Solid-Solutions, *Journal of the American Ceramic Society* 66 (1983) C18-C20.
- [70] A.E. McHale and R.S. Roth, Low-Temperature Phase-Relationships in the System ZrO_2 - TiO_2 , *Journal of the American Ceramic Society* 69 (1986) 827-832.
- [71] R. Merkle and H. Bertagnolli, Crystallization behaviour of the series of solid solutions $Zr_xTi_{1-x}O_2$ and $Pb_yZr_xTi_{1-x}O_{2+y}$ prepared by the sol-gel process, *Journal of Materials Chemistry* 8 (1998) 2433-2439.
- [72] U. Troitzsch, TiO_2 -doped zirconia: Crystal structure, monoclinic-tetragonal phase transition, and the new tetragonal compound Zr_3TiO_8 , *Journal of the American Ceramic Society* 89 (2006) 3201-3210.
- [73] U. Troitzsch, A.G. Christy and D.J. Ellis, Synthesis of ordered zirconium titanate $(Zr,Ti)_2O_4$ from the oxides using fluxes, *Journal of the American Ceramic Society* 87 (2004) 2058-2063.
- [74] U. Troitzsch, A.G. Christy and D.J. Ellis, The crystal structure of disordered $(Zr,Ti)O_2$ solid solution including srilankite: evolution towards tetragonal ZrO_2 with increasing Zr, *Physics and Chemistry of Minerals* 32 (2005) 504-514.
- [75] U. Troitzsch and D.J. Ellis, High-PT study of solid solutions in the system ZrO_2 - TiO_2 : The stability of srilankite, *European Journal of Mineralogy* 16 (2004) 577-584.
- [76] U. Troitzsch and D.J. Ellis, The ZrO_2 - TiO_2 phase diagram, *Journal of Materials Science* 40 (2005) 4571-4577.
- [77] A. Willgallis and H. Hartl, $(Zr_{0.33}Ti_{0.67})O_2$ - a Natural Zirconium-Titanium Oxide with an α - PbO_2 Structure, *Zeitschrift Fur Kristallographie* 164 (1983) 59-66.
- [78] S.I. Kostrovitsky, V.K. Garanin and D.A. Varlamov, Srilankite - the 2nd Finding in the World, *Doklady Akademii Nauk* 328 (1993) 601-604.
- [79] L.P. Wang, E.J. Essene and Y.X. Zhang, Mineral inclusions in pyrope crystals from Garnet Ridge, Arizona, USA: implications for processes in the upper mantle, *Contributions to Mineralogy and Petrology* 135 (1999) 164-178.
- [80] B. Bingen, H. Austrheim and M. Whitehouse, Ilmenite as a source for zirconium during high-grade metamorphism? Textural evidence from the Caledonides of western Norway and implications for zircon geochronology, *Journal of Petrology* 42 (2001) 355-375.
- [81] T. Morishita, J. Maeda, S. Miyashita, T. Matsumoto and H.J.B. Dick, Magmatic srilankite (Ti_2ZrO_6) in gabbroic vein cutting oceanic peridotites: An unusual product of peridotite-melt interactions beneath slow-spreading ridges, *American Mineralogist* 89 (2004) 759-766.
- [82] J.E. Taggart, E.E. Foord, A. Rosenzweig and T. Hanson, Scrutinyite, Natural Occurrences of α - PbO_2 from Bingham, New-Mexico, USA, and Mapimi, Mexico, *Canadian Mineralogist* 26 (1988) 905-910.
- [83] J.G. Li, T. Ishigaki and X.D. Sun, Anatase, brookite, and rutile nanocrystals via redox reactions under mild hydrothermal conditions: Phase-selective synthesis

- and physicochemical properties, *Journal of Physical Chemistry C* 111 (2007) 4969-4976.
- [84] U. Bach, D. Lupo, P. Comte, J.E. Moser, F. Weissortel, J. Salbeck, H. Spreitzer and M. Gratzel, Solid-state dye-sensitized mesoporous TiO₂ solar cells with high photon-to-electron conversion efficiencies, *Nature* 395 (1998) 583-585.
- [85] M.R. Hoffmann, S.T. Martin, W.Y. Choi and D.W. Bahnemann, Environmental Applications of Semiconductor Photocatalysis, *Chemical Reviews* 95 (1995) 69-96.
- [86] M.A. Fox and M.T. Dulay, Heterogeneous Photocatalysis, *Chemical Reviews* 93 (1993) 341-357.
- [87] M. Mattesini, J.S. de Almeida, L. Dubrovinsky, N. Dubrovinskaia, B. Johansson and R. Ahuja, Cubic TiO₂ as a potential light absorber in solar-energy conversion, *Physical Review B* 70 (2004).
- [88] A. Fujishim and K. Honda, Electrochemical Photolysis of Water at a Semiconductor Electrode, *Nature* 238 (1972) 37-&.
- [89] W.M. Kriven, Possible Alternative Transformation Tougheners to Zirconia - Crystallographic Aspects, *Journal of the American Ceramic Society* 71 (1988) 1021-1030.
- [90] T. Muromura and Y. Hinatsu, Fluorite Type Phase in Nuclear Waste Ceramics with High Zirconia and Alumina Contents, *Journal of Nuclear Materials* 151 (1987) 55-62.
- [91] S.X. Zhang, J.B. Li, J. Cao, H.Z. Zhai and B. Zhang, Effect of composition on sinterability, microstructure and microwave dielectric properties of Zr_xTi_{1-x}O₄ (x=0.40-0.60) ceramics, *Journal of Materials Science Letters* 20 (2001) 1409-1411.
- [92] F. Azough, R. Freer, C.L. Wang and G.W. Lorimer, The relationship between the microstructure and microwave dielectric properties of zirconium titanate ceramics, *Journal of Materials Science* 31 (1996) 2539-2549.
- [93] F. Azough, A. Wright and R. Freer, The Microstructure and Dielectric-Properties of Zr₅Ti₇O₂₄ Ceramics, *Journal of Solid State Chemistry* 108 (1994) 284-290.
- [94] G. Wolfram and H.E. Gobel, Existence Range, Structural and Dielectric-Properties of Zr_xTi_ySn_zO₄ Ceramics (X+Y+Z=2), *Materials Research Bulletin* 16 (1981) 1455-1463.
- [95] S.H. Jhi, J. Ihm, S.G. Louie and M.L. Cohen, Electronic mechanism of hardness enhancement in transition-metal carbonitrides, *Nature* 399 (1999) 132-134.
- [96] C.M. Sung and M. Sung, Carbon nitride and other speculative superhard materials, *Materials Chemistry and Physics* 43 (1996) 1-18.
- [97] D.M. Teter, Computational alchemy: The search for new superhard materials, *Mrs Bulletin* 23 (1998) 22-27.
- [98] J.E. Lowther, Superhard ceramic oxides, *Mrs Bulletin* 28 (2003) 189-193.
- [99] W. Luo, S.F. Yang, Z.C. Wang, Y. Wang, R. Ahuja, B. Johansson, J. Liu and G.T. Zou, Structural phase transitions in brookite-type TiO₂ under high pressure, *Solid State Communications* 133 (2005) 49-53.
- [100] S.K. Chan, Y. Fang, M. Grimsditch, Z. Li, M.V. Nevitt, W.M. Robertson and E.S. Zouboulis, Temperature-Dependence of the Elastic-Moduli of Monoclinic Zirconia, *Journal of the American Ceramic Society* 74 (1991) 1742-1744.

- [101] R.E. Cohen, M.J. Mehl and L.L. Boyer, Phase-Transitions and Elasticity in Zirconia, *Physica B & C* 150 (1988) 1-9.
- [102] J.K. Dewhurst and J.E. Lowther, Relative stability, structure, and elastic properties of several phases of pure zirconia, *Physical Review B* 57 (1998) 741-747.
- [103] N.J. Petch, The Cleavage Strength of Polycrystals, *Journal of the Iron and Steel Institute* 174 (1953) 25-28.
- [104] E.O. Hall, The Deformation and Ageing of Mild Steel .3. Discussion of Results, *Proceedings of the Physical Society of London Section B* 64 (1951) 747-753.
- [105] T.G. Nieh and J. Wadsworth, Hall-Petch Relation in Nanocrystalline Solids, *Scripta Metallurgica Et Materialia* 25 (1991) 955-958.
- [106] J. Schiotz, F.D. Di Tolla and K.W. Jacobsen, Softening of nanocrystalline metals at very small grain sizes, *Nature* 391 (1998) 561-563.
- [107] S. Ogata, H. Iyetomi, K. Tsuruta, F. Shimojo, R.K. Kalia, A. Nakano and P. Vashishta, Variable-charge interatomic potentials for molecular-dynamics simulations of TiO₂, *Journal of Applied Physics* 86 (1999) 3036-3041.
- [108] H. leRoux and L. Glasser, Transferable potentials for the Ti-O system, *Journal of Materials Chemistry* 7 (1997) 843-851.
- [109] F.H. Streitz and J.W. Mintmire, Charge-Transfer and Bonding in Metallic Oxides, *Journal of Adhesion Science and Technology* 8 (1994) 853-864.
- [110] C.R.A. Catlow, C.M. Freeman and R.L. Royle, Recent Studies Using Static Simulation Techniques, *Physica B & C* 131 (1985) 1-12.
- [111] M. Mostoller and J.C. Wang, Ionic Potential Models in Insulators Having the Rutile Structure, *Physical Review B* 32 (1985) 6773-6786.
- [112] M. Matsui and M. Akaogi in: *Molecular Simulation* (1991) 239-244.
- [113] V. Swamy and J.D. Gale, Transferable variable-charge interatomic potential for atomistic simulation of titanium oxides, *Physical Review B* 62 (2000) 5406-5412.
- [114] K. Rosciszewski, K. Doll, B. Paulus, P. Fulde and H. Stoll, Ground-state properties of rutile: Electron-correlation effects, *Physical Review B* 57 (1998) 14667-14672.
- [115] P. Reinhardt, B.A. Hess and M. Causa, Electronic and geometrical structure of bulk rutile studied with Hartree-Fock and density functional methods, *International Journal of Quantum Chemistry* 58 (1996) 297-306.
- [116] J.K. Dewhurst and J.E. Lowther, High-pressure structural phases of titanium dioxide, *Physical Review B* 54 (1996) R3673-R3675.
- [117] J. Muscat, V. Swamy and N.M. Harrison, First-principles calculations of the phase stability of TiO₂, *Physical Review B* 65 (2002).
- [118] F. Labat, P. Baranek, C. Domain, C. Minot and C. Adamo, Density functional theory analysis of the structural and electronic properties of TiO₂ rutile and anatase polytypes: Performances of different exchange-correlation functionals, *Journal of Chemical Physics* 126 (2007).
- [119] M. Posternak, A. Baldereschi, E.J. Walter and H. Krakauer, Wannier functions and Born charge tensors of brookite TiO₂, *Physical Review B* 74 (2006).
- [120] K.M. Glassford and J.R. Chelikowsky, Structural and Electronic-Properties of Titanium-Dioxide, *Physical Review B* 46 (1992) 1284-1298.

- [121] M. Mikami, S. Nakamura, O. Kitao and H. Arakawa, Lattice dynamics and dielectric properties of TiO₂ anatase: A first-principles study (vol B 66, art no 155213, 2002), *Physical Review B* 69 (2004).
- [122] M.Y. Kuo, C.L. Chen, C.Y. Hua, H.C. Yang and P.Y. Shen, Density functional theory calculations of dense TiO₂ polymorphs: Implication for visible-light-responsive photocatalysts, *Journal of Physical Chemistry B* 109 (2005) 8693-8700.
- [123] C.Y. Lee and X. Gonze, Dielectric-Constants and Born Effective Charges of TiO₂ Rutile, *Physical Review B* 49 (1994) 14730-14731.
- [124] S. Matsushima, K. Obata, H. Yamane, K. Yamada, H. Nakamura, M. Arai and K. Kobayashi, First-principles band calculation of TiO₂ with Brookite structure, *Electrochemistry* 72 (2004) 694-696.
- [125] S.D. Mo and W.Y. Ching, Electronic and Optical-Properties of 3 Phases of Titanium-Dioxide - Rutile, Anatase, and Brookite, *Physical Review B* 51 (1995) 13023-13032.
- [126] V. Swamy, J.D. Gale and L.S. Dubrovinsky, Atomistic simulation of the crystal structures and bulk moduli of TiO₂ polymorphs, *Journal of Physics and Chemistry of Solids* 62 (2001) 887-895.
- [127] W. Kohn and L.J. Sham, Self-Consistent Equations Including Exchange and Correlation Effects, *Physical Review* 140 (1965) 1133-&.
- [128] P. Hohenberg and W. Kohn, Inhomogeneous Electron Gas, *Physical Review B* 136 (1964) B864-&.
- [129] J.P. Perdew, J.A. Chevary, S.H. Vosko, K.A. Jackson, M.R. Pederson, D.J. Singh and C. Fiolhais, Atoms, Molecules, Solids, and Surfaces - Applications of the Generalized Gradient Approximation for Exchange and Correlation, *Physical Review B* 46 (1992) 6671-6687.
- [130] I.L. Spain, Ultrahigh pressure apparatus and technology, in: *High pressure Technology*, vol. 1 Equipment design, materials, and properties, editors Spain, I.L. and Pauwe J., Marcel Dekker, new York (1977) 395.
- [131] W.C. Luth and O.F. Tuttle, Externally heated cold-seal pressure vessels for use to 10,000 bars and 750 °C, *American Mineralogist* 48 (1963) 1401-1403.
- [132] O.F. Tuttle, Two pressure vessels for silicate-water studies, *Geological Society of America Bulletin* 60 (1949) 1927-1929.
- [133] A.L. Boettcher and D.M. Kerrick, Temperature-calibration of cold-seal pressure vessels, *Research Techniques for high pressure and high temperature*, G.C. Ulmer (ed.), New York, Springer (1971) 179-173.
- [134] J.R. Holloway and B.J. Wood, *Simulating the Earth: Experimental Geochemistry*, Boston, Unwin Hyman (1988) 26.
- [135] D. Dolejs and D.R. Baker, Fluorite solubility in hydrous haplogranitic melts at 100 MPa, *Chemical Geology* 225 (2006) 40-60.
- [136] T. Dunn, The piston-cylinder apparatus, in: Luth, R.W. (ed): *Experiments at High Pressure and Applications to the Earth's Mantle*, MAC shortcourse handbook, Vol.21. Mineralogical association of Canada, (1993) p. 39-94.
- [137] N. Kawai and S. Endo, Generation of Ultrahigh Hydrostatic Pressures by a Split Sphere Apparatus, *Review of Scientific Instruments* 41 (1970) 1178-&.
- [138] J. Graham, The multianvil press. In Sammis, C.G and Henvey, T.L. (eds.), *Geophysics Part A, Laboratory Measurements, Methods of experimental physics*. Academic Press, Orlando (1987).

- [139] E. Ohtani, T. Irifune, W. Hibberson and A.E. Ringwood, Modified split-sphere guide block for practical operation of a multi-anvil apparatus, *High Temperatures - high Pressures* 19 (1987) 523-529.
- [140] D. Walker, M.A. Carpenter and C.M. Hitch, Some Simplifications to Multianvil Devices for High-Pressure Experiments, *American Mineralogist* 75 (1990) 1020-1028.
- [141] Y.W. Fei and S.K. Saxena, Internally Consistent Thermodynamic Data and Equilibrium Phase-Relations for Compounds in the System MgO-SiO₂ at High-Pressure and High-Temperature, *Journal of Geophysical Research-Solid Earth and Planets* 95 (1990) 6915-6928.
- [142] M.J. Walter, Y. Thibault, K. Wei and R.W. Luth, Characterizing Experimental Pressure and Temperature Conditions in Multi-Anvil Apparatus, *Canadian Journal of Physics* 73 (1995) 273-286.
- [143] A. Jayaraman, Diamond Anvil Cell and High-Pressure Physical Investigations, *Reviews of Modern Physics* 55 (1983) 65-108.
- [144] G.J. Piermarini and S. Block, Ultrahigh Pressure Diamond-Anvil Cell and Several Semiconductor Phase-Transition Pressures in Relation to Fixed-Point Pressure Scale, *Review of Scientific Instruments* 46 (1975) 973-979.
- [145] H.K. Mao, P.M. Bell, K.J. Dunn, R.M. Chrenko and R.C. Devries, Absolute Pressure Measurements and Analysis of Diamonds Subjected to Maximum Static Pressures of 1.3-1.7 Mbar, *Review of Scientific Instruments* 50 (1979) 1002-1009.
- [146] L. Merrill and W.A. Bassett, Miniature Diamond Anvil Pressure Cell for Single-Crystal X-Ray-Diffraction Studies, *Review of Scientific Instruments* 45 (1974) 290-294.
- [147] G. Huber, K. Syassen and W.B. Holzapfel, Pressure-Dependence of 4f Levels in Europium Pentaphosphate up to 400-Kbar, *Physical Review B* 15 (1977) 5123-5128.
- [148] N. Dubrovinskaia and L. Dubrovinsky, Whole-cell heater for the diamond anvil cell, *Review of Scientific Instruments* 74 (2003) 3433-3437.
- [149] H.K. Mao, J. Xu and P.M. Bell, Calibration of the Ruby Pressure Gauge to 800-Kbar under Quasi-Hydrostatic Conditions, *Journal of Geophysical Research-Solid Earth and Planets* 91 (1986) 4673-4676.
- [150] T. Watanuki, O. Shimomura, T. Yagi, T. Kondo and M. Isshiki, Construction of laser-heated diamond anvil cell system for in situ x-ray diffraction study at SPring-8, *Review of Scientific Instruments* 72 (2001) 1289-1292.
- [151] D. Andrault, G. Fiquet, T. Charpin and T. le Bihan, Structure analysis and stability field of beta-iron at high P and T, *American Mineralogist* 85 (2000) 364-371.
- [152] L.S. Dubrovinsky, P. Lazor, S.K. Saxena, P. Haggkvist, H.P. Weber, T. Le Bihan and D. Hausermann, Study of laser heated iron using third generation synchrotron X-ray radiation facility with imaging plate at high pressures, *Physics and Chemistry of Minerals* 26 (1999) 539-545.
- [153] G.Y. Shen, H.K. Mao, R.J. Hemley, T.S. Duffy and M.L. Rivers, Melting and crystal structure of iron at high pressures and temperatures, *Geophysical Research Letters* 25 (1998) 373-376.

- [154] G.Y. Shen, V.B. Prakapenka, P.J. Eng, M.L. Rivers and S.R. Sutton, Facilities for high-pressure research with the diamond anvil cell at GSECARS, *Journal of Synchrotron Radiation* 12 (2005) 642-649.
- [155] D. McKie and C. McKie, *Essentials of Crystallography (Crystalline Solids Vol 1)*, Blackwell Science Ltd. (1986).
- [156] B.H. Toby, EXPGUI, a graphical user interface for GSAS, *Journal of Applied Crystallography* 34 (2001) 210-213.
- [157] A.C. Larson and R.B. Von Dreele, Los Alamos National Laboratory Report LAUR (2000) 86-748.
- [158] A. Hammersley, Computer program Fit2D, ESRF, Grenoble (1998).
- [159] A. Coelho, TOPAS-Academic Users Manual, <http://pws.prserv.Net/Alan.Coelho/> (2005).
- [160] A. Kern, A. Coelho and R.W. Cheary, in: E.J. Mettemeijer, P. Scard (eds): *Diffraction Analysis of the Microstructure of Materials*, p. 17, Springer, Berlin (2004).
- [161] D. Balzar and H. Ledbetter, Voigt-Function Modeling in Fourier-Analysis of Size-Broadened and Strain-Broadened X-Ray-Diffraction Peaks, *Journal of Applied Crystallography* 26 (1993) 97-103.
- [162] D. Balzar, Profile Fitting of X-Ray-Diffraction Lines and Fourier-Analysis of Broadening, *Journal of Applied Crystallography* 25 (1992) 559-570.
- [163] N.C. Popa and D. Balzar, An analytical approximation for a size-broadened profile given by the lognormal and gamma distributions, *Journal of Applied Crystallography* 35 (2002) 338-346.
- [164] V.L. Aksenov, A.Y. Kuzmin, J. Purans and S.I. Tyutyunnikov, EXAFS spectroscopy at synchrotron-radiation beams, *Physics of Particles and Nuclei* 32 (2001) 675-707.
- [165] J.P. Itie, B. Couzinet, A. Polian, A.M. Flank and P. Lagarde, Pressure-induced disappearance of the local rhombohedral distortion in BaTiO₃, *Europhysics Letters* 74 (2006) 706-711.
- [166] R.V. Vedrinskii, V.L. Kraizman, A.A. Novakovich, P.V. Demekhin and S.V. Urazhdin, Pre-edge fine structure of the 3d atom K x-ray absorption spectra and quantitative atomic structure determinations for ferroelectric perovskite structure crystals, *Journal of Physics-Condensed Matter* 10 (1998) 9561-9580.
- [167] F. Farges, G.E. Brown and J.J. Rehr, Ti K-edge XANES studies of Ti coordination and disorder in oxide compounds: Comparison between theory and experiment, *Physical Review B* 56 (1997) 1809-1819.
- [168] A. Rogalev, J. Goulon, C. Goulon-Ginet and C. Malgrange, in *Magnetism and Synchrotron Radiation*, E. Beaurepaire, F. Scheurer, G. Krill and J.-P. Kappler (eds.) *Lectures Notes in Physics*, Springer, New York 565 (2001).
- [169] C. Dhaussy, N. Jaouen, J.P. P. Itié, A. Rogalev, S. Marinel and A. Veres, *Synchrotron Radiation Instrumentation*, AIP Conf.Proc. No. 879, AIP, New York (2007) 1825.
- [170] A. Dadashev, M.P. Pasternak, G.K. Rozenberg and R.D. Taylor, Applications of perforated diamond anvils for very high-pressure research, *Review of Scientific Instruments* 72 (2001) 2633-2637.
- [171] J.P. Itie, F. Baudalet, A. Congeduti, B. Couzinet, F. Farges and A. Polian, High pressure x-ray absorption spectroscopy at lower energy in the dispersive mode:

- application to Ce and FePO₄, *Journal of Physics-Condensed Matter* 17 (2005) S883-S888.
- [172] L. Nasdala, D.C. Smith, R. Kaindl and M.A. Ziemann, Raman spectroscopy: Analytical perspectives in mineralogical research. In Beran, A. and Libowitzky (eds.), *EMU Notes in Mineralogy, Vol. 6: Spectroscopic Methods in Mineralogy*. Eötvös University Press, Budapest. (2004) 281-243.
- [173] A.J. Jayaraman, Diamond anvil cell and high-pressure physical investigations, *Review of Modern Physics* 55 (1983) 65-85.
- [174] J.R. Ferraro, *Vibrational spectroscopy at high external pressures- The diamond anvil cell*. New York, Academic Press (1984) 264.
- [175] J.C. Chervin, B. Canny, M. Gauthier and P. Pruzan, Micro-Raman at Variable Low-Temperature and Very High-Pressure, *Review of Scientific Instruments* 64 (1993) 203-206.
- [176] A. Putnis, *Introduction to Mineral Sciences*. Cambridge University press, Cambridge. (1992).
- [177] S.J.B. Reed, *Electron microprobe analysis and scanning electron microscopy in geology*. Cambridge University press, Cambridge. (1996).
- [178] J.T. Armstrong, Citzaf - a Package of Correction Programs for the Quantitative Electron Microbeam X-Ray-Analysis of Thick Polished Materials, Thin-Films, and Particles, *Microbeam Analysis* 4 (1995) 177-200.
- [179] R.F. Egerton, *Electron energy-loss spectroscopy in the electron microscope*. Plenum press, New York. (1996).
- [180] D.B. Williams and C.B. Carter, *Transmission electron microscopy - IV Spectroscopy*. Plenum press., New York (1996) 637-729.
- [181] R. Wirth, Focused ion beam (FIB): Applications in micro- and nanoanalysis in geosciences and applied mineralogy, *Praktische Metallographie-Practical Metallography* 42 (2005) 188-205.
- [182] J. Hafner, Atomic-scale computational materials science, *Acta Materialia* 48 (2000) 71-92.
- [183] G. Kresse and J. Hafner, Ab-Initio Molecular-Dynamics for Open-Shell Transition-Metals, *Physical Review B* 48 (1993) 13115-13118.
- [184] S.H. Wei, H. Krakauer and M. Weinert, Linearized Augmented-Plane-Wave Calculation of the Electronic-Structure and Total Energy of Tungsten, *Physical Review B* 32 (1985) 7792-7797.
- [185] P. Blaha, K. Schwarz, P. Dufek and J. Luitz, *Wien97*, Vienna University of Technology (1990).
- [186] P. Blaha, K. Schwarz, P. Sorantin and S.B. Trickey, Full-Potential, Linearized Augmented Plane-Wave Programs for Crystalline Systems, *Computer Physics Communications* 59 (1990) 399-415.
- [187] J.P. Perdew, K. Burke and M. Ernzerhof, Generalized gradient approximation made simple, *Physical Review Letters* 77 (1996) 3865-3868.
- [188] Z.G. Wu and R.E. Cohen, More accurate generalized gradient approximation for solids, *Physical Review B* 73 (2006).
- [189] H.J. Monkhorst and J.D. Pack, Special Points for Brillouin-Zone Integrations, *Physical Review B* 13 (1976) 5188-5192.
- [190] F. Birch, Finite Elastic Strain of Cubic Crystals, *Physical Review*, 1947, pp. 809-824.

- [191] S. Ananta, R. Tipakontitikul and T. Tunkasiri, Synthesis, formation and characterization of zirconium titanate (ZT) powders, *Materials Letters* 57 (2003) 2637-2642.
- [192] M. Daturi, A. Cremona, F. Milella, G. Busca and E. Vogna, Characterisation of zirconia-titania powders prepared by coprecipitation, *Journal of the European Ceramic Society* 18 (1998) 1079-1087.
- [193] I.C. Cosentino, E.N.S. Muccillo, R. Muccillo and F.M. Vichi, Low-temperature sol-gel synthesis of single-phase $ZrTiO_4$ nanoparticles, *Journal of Sol-Gel Science and Technology* 37 (2006) 31-37.
- [194] A. Bianco, M. Paci and R. Freer, Zirconium titanate: from polymeric precursors to bulk ceramics, *Journal of the European Ceramic Society* 18 (1998) 1235-1243.
- [195] E.L. Sham, M.A.G. Aranda, E.M. Farfan-Torres, J.C. Gottifredi, M. Martinez-Lara and S. Bruque, Zirconium titanate from sol-gel synthesis: Thermal decomposition and quantitative phase analysis, *Journal of Solid State Chemistry* 139 (1998) 225-232.
- [196] P. Lobmann, Soluble powders as precursors for TiO_2 thin films, *Journal of Sol-Gel Science and Technology* 33 (2005) 275-282.
- [197] M. Bockmeyer and P. Lobmann, Densification and microstructural evolution of TiO_2 films prepared by sol-gel processing, *Chemistry of Materials* 18 (2006) 4478-4485.
- [198] S.A. Borkar and S.R. Dharwadkar, Temperatures and kinetics of anatase to rutile transformation in doped TiO_2 heated in microwave field, *Journal of Thermal Analysis and Calorimetry* 78 (2004) 761-767.
- [199] M. Yashima, T. Hirose, S. Katano, Y. Suzuki, M. Kakihana and M. Yoshimura, Structural-Changes of ZrO_2 - CeO_2 Solid-Solutions around the Monoclinic-Tetragonal Phase-Boundary, *Physical Review B* 51 (1995) 8018-8025.
- [200] R.E. Newnham, Crystal Structure of $ZrTiO_4$, *Journal of the American Ceramic Society* 50 (1967) 216-&.
- [201] W. Gonschorek, X-Ray Charge-Density Study of Rutile (TiO_2), *Zeitschrift Fur Kristallographie* 160 (1982) 187-203.
- [202] C.J. Howard, E.H. Kisi and O. Ohtaka, Crystal-Structures of 2 Orthorhombic Zirconias, *Journal of the American Ceramic Society* 74 (1991) 2321-2323.
- [203] E. Holbig, L. Dubrovinsky, G. Steinle-Neumann, V. Prakapenka and V. Swamy, Compression behavior of Zr-doped nanoanatase, *Zeitschrift Fur Naturforschung Section B-a Journal of Chemical Sciences* 61 (2006) 1577-1585.
- [204] Y. Li, T.J. White and S.H. Lim, Low-temperature synthesis and microstructural control of titania nano-particles, *Journal of Solid State Chemistry* 177 (2004) 1372-1381.
- [205] V. Swamy, D. Menzies, B.C. Muddle, A. Kuznetsov, L.S. Dubrovinsky, Q. Dai and V. Dmitriev, Nonlinear size dependence of anatase TiO_2 lattice parameters, *Applied Physics Letters* 88 (2006).
- [206] T. Yagi, Experimental-Determination of Thermal-Expansion of Several Alkali-Halides at High-Pressures, *Transactions-American Geophysical Union* 58 (1977) 492-492.
- [207] V. Swamy, A. Kuznetsov, L.S. Dubrovinsky, P.F. McMillan, V.B. Prakapenka, G. Shen and B.C. Muddle, Size-dependent pressure-induced amorphization in nanoscale TiO_2 , *Physical Review Letters* 96 (2006) 135702.

- [208] G.S. Li, L.P. Li, J. Boerio-Goates and B.F. Woodfield, Grain-growth kinetics of rutile TiO₂ nanocrystals under hydrothermal conditions, *Journal of Materials Research* 18 (2003) 2664-2669.
- [209] R.M. Hazen and L.W. Finger, Bulk Moduli and High-Pressure Crystal-Structures of Rutile-Type Compounds, *Journal of Physics and Chemistry of Solids* 42 (1981) 143-151.
- [210] L.C. Ming and M.H. Manghnani, Isothermal Compression of TiO₂ (Rutile) under Hydrostatic-Pressure to 106-Kbar, *Journal of Geophysical Research* 84 (1979) 4777-4779.
- [211] X.L. Wu, D.W. Meng and Y.J. Han, alpha-PbO₂-type nanophase of TiO₂ from coesite-bearing eclogite in the Dabie Mountains, China, *American Mineralogist* 90 (2005) 1458-1461.
- [212] Z.W. Wang and S.K. Saxena, Raman spectroscopic study on pressure-induced amorphization in nanocrystalline anatase (TiO₂), *Solid State Communications* 118 (2001) 75-78.
- [213] Z.W. Wang, S.K. Saxena, V. Pischedda, H.P. Liermann and C.S. Zha, X-ray diffraction study on pressure-induced phase transformations in nanocrystalline anatase/rutile (TiO₂), *Journal of Physics-Condensed Matter* 13 (2001) 8317-8323.
- [214] G.R. Hearne, J. Zhao, A.M. Dawe, V. Pischedda, M. Maaza, M.K. Nieuwoudt, P. Kibasomba, O. Nemraoui, J.D. Comins and M.J. Witcomb, Effect of grain size on structural transitions in anatase TiO₂: A Raman spectroscopy study at high pressure, *Physical Review B* 70 (2004).

Erklärung

Hiermit erkläre ich, daß ich die vorliegende Arbeit selbständig verfaßt und keine anderen als die von mir angegeben Quellen und Hilfsmittel benutzt habe.

Ferner erkläre ich, daß ich nicht anderweitig mit oder ohne Erfolg versucht habe, eine Dissertation einzureichen. Ich habe keine gleichartige Doktorprüfung an einer anderen Hochschule endgültig nicht bestanden.

Bayreuth, den 19. 12. 2007

Eva Holbig